The Pennsylvania State University

The Graduate School

DOMAIN WALL MOTION IN POLYCRYSTALLINE FERROELECTRIC FILMS

A Thesis in

Materials Science and Engineering

by

Gavin T. Hennessey

Submitted in Partial Fulfillment
of the Requirements
for the Degree of

Master of Science

December 2022

The thesis of Gavin T. Hennessey was reviewed and approved by the following:

Susan Trolier-McKinstry
Thesis Advisor
Evan Pugh University Professor and Stewart Flaschen Professor of Ceramic Science & Engineering

John Mauro
MatSE Department Head for Graduate Education
Professor of Materials Science & Engineering

Jon-Paul Maria
Professor of Materials Science & Engineering

Darren Pagan
Assistant Professor of Materials Science & Engineering

ABSTRACT

Though the functional properties of ferroelectrics depend heavily on the mobility of polar boundaries, the microstructural factors that impact domain structure and domain wall movement are not fully understood. This work describes preparatory work to enable exploration of how a broad range of grain boundary orientations impact domain wall motion and pinning depth. For this purpose, lead zirconate titanate 52/48 (PZT) and strontium ruthenate (SRO) films were deposited onto platinum-coated silicon or polycrystalline strontium titanate ($SrTiO_3$) substrates. The polycrystalline large-grained $SrTiO_3$ substrates allow a large variety of structure features and grain boundary orientations to be isolated for study. By analyzing the electrical properties as a function of position, it is possible to extract the influence of grain boundaries and triple points on the mobility of the domain structure.

Samples were deposited using either pulsed laser deposition or chemical solution deposition. PZT films with average compositions at the morphotropic phase boundary showed high relative permittivity (>1000), high remanent polarization (>20 $\mu C/cm^2$), and a low loss tangent (< 2%) could be obtained through both techniques, and were analyzed for thickness and grain structure. The optimized growth conditions of PLD utilized a substrate temperature of 630 °C, laser energy of 1.4 J/cm^2, repetition rate of 10 Hz, and deposition pressure of 350 mTorr for a PZT 52/48 (10% excess PbO) target. In the case of strontium ruthenate, the optimized film growth utilized a laser energy of 1.4 J/cm^2, repetition rate of 10 Hz, deposition pressure of 160 mTorr, and substrate temperature of 680 °C.

PZT lateral grain sizes measured using scanning electron microscopy (SEM) averaged around 200 nanometers while the large grains of $SrTiO_3$ ranged from one to ten microns across a single sample. Electron Backscatter Diffraction (EBSD) and cross-section SEM was then utilized to visualize the grain orientations, microstructure, and film thicknesses. When paired with Piezoresponse Force Microscopy (PFM), the collected sample information allowed microstructure features to be marked, revisited, and cataloged for their property impact. The orientation of a single grain defined by EBSD mapping was found to have an end to end disorientation of less than 2° for each grain investigated using the AztecCrystal software.

The piezoelectric nonlinearity of numerous grain boundaries and triple points was mapped using PFM. It was found that triple points typically serve as deep pinning sites, for which domain wall motion can be degraded with a radial width of influence of up to 527 ± 38 nm for a total of 1054 ± 76 nm. Moreover, at the triple points, the nonlinear piezoelectric response is often non-Rayleigh-like in character, suggesting that the domain walls locally see a non-Gaussian set of restoring forces. It was found that different grain boundaries influenced the mobility of domain walls on length scales from 124 ± 23 nm to 575 ± 73 nm normal to their respective grain boundary. The largest width of influence recorded up to 905 ± 153nm. The minimum values of the irreversible/reversible Rayleigh constants, $\alpha/d_{33,init}$, were found to be larger for Coincident Site Lattice (CSL) boundaries compared to random grain boundaries which suggests decreased pinning when two grains share a unique rotation axis.

TABLE OF CONTENTS

LIST OF FIGURES

LIST OF TABLES

Acknowledgements

Funding for this work was generously provided by The National Science Foundation through NSF DMR-2025439; though the findings and conclusions do not necessarily reflect the view of the funding agency. I would also like to acknowledge the support of the Trolier-McKinstry Group, the Material Research Institute Staff, and the Oak Ridge National Lab Staff whose assistance cannot be understated. With particular thanks to Dr. McKinstry for her advising prowess and vast knowledge, to Pannawit Tipsawat for his assistance in MLA patterning and accompanying me for many long nights in the lab, to Travis Peters and Liam Collins for their hard work making Piezoresponse Force Microscopy measurements at Oak Ridge National Lab in Tennessee, and to Yeongwoo Son for his help in continuously troubleshooting and reengineering the Pulsed Laser Deposition system with me. My experience was greatly enriched by having these researchers beside me and I would be remiss to not mention their continual effort. Lastly, thank you to my family and friends for their support throughout my entire schooling process.

Chapter 1

Introduction & Statement of the Problem

While the properties of ferroelectrics have been reported to depend on domain wall mobility, the influence of microstructure on both domain structure and domain wall movement is not fully known. This work aims to explore the relationship between microstructure and domain wall motion with respect to a range of microstructural features. A domain is a region of approximately uniform polarization that can grow and shrink in response to local stresses and electric fields; as the domain with polarization oriented close to the direction of applied field tend to grow, the boundary that separates the two domains will shift in what is called domain wall motion.[1,2] To analyze the length scale over which various pinning sites influence the mobility of domain walls, lead zirconate titanate $PbZr_{1-x}Ti_xO_3$ (PZT) ferroelectric films and strontium ruthenate $SrRuO_3$ (SRO) bottom electrodes were deposited onto polycrystalline strontium titanate $SrTiO_3$ substrates. Local epitaxial growth of PZT ferroelectric films on polycrystalline substrate allows the effect of structural features to be studied for a wider range of available orientations compared to bicrystal or single crystal samples. [3-5] Ultimately, this will allow features such as grain boundary orientation, defects, and triple points to be assessed for their influence on domain wall motion. In particular, by analyzing electrical properties as a function of position, one can extract the width of influence of domain pinning sites on an evolving domain structure. The configuration of these domains and domain wall movement about pinning sites have significant implications on device performance.[6] For example, the distinctive ferroelectric

feature of a polarization – electric field (P-E) hysteresis loop arises from the nucleation and growth of domains in response to a large AC voltage excitation.[7]

Figure 1-1 shows three phases in the PZT phase diagram, in which one can see that in the tetragonal and rhombohedral perovskite phases, the central cation displaces from its position in the cubic phase to form a spontaneous polarization in the direction of the cation displacement. The available directions for the spontaneous polarization depend on the symmetry lost with respect to the prototype paraelectric phase. The material phase also impacts the resultant domain structure and domain dynamics. [1,8]

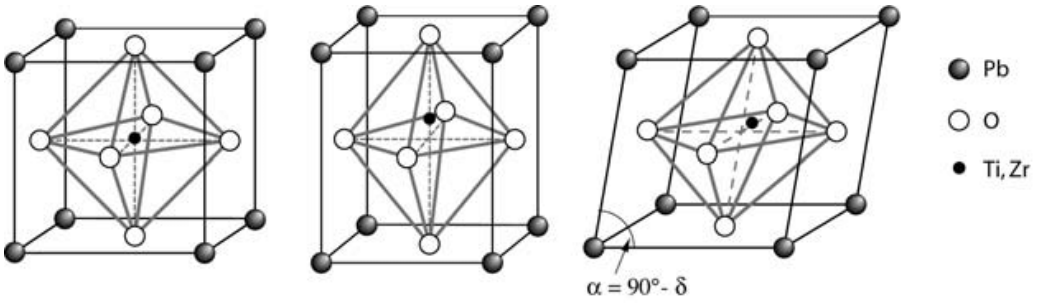

Figure 1-1: Perovskite crystal in its paraelectric cubic (left), ferroelectric tetragonal (middle), and ferroelectric rhombohedral (right) states adopted from [9] demonstrating the direction of displacement for the central cation

In this work, thin film samples were deposited using two techniques: pulsed laser deposition (PLD) and sol-gel chemical solution deposition (CSD). A combination of structural and electromechanical characterization was used to determine the impact of local microstructure with respect to the surrounding conditions. Orientation Imaging Microscopy (OIM) was used to map the grain orientation and confirm local epitaxy, while Piezoresponse Force Microscopy (PFM) was used to assess the piezoelectric nonlinearity at each position. Probing the microstructure of polycrystalline thin films, then electrically

exciting the sample about a pinning site allows the analysis of the local domain wall mobility.

Mission Statement for Thesis Work

This thesis is directed towards increasing the understanding of the way ferroelectric domain walls interact with microstructural features. The approach adopted is to analyze the nonlinear properties of PZT films with respect to local microstructure, such that the width of influence can be isolated for each domain wall pinning site. Of interest is to determine whether certain classes of grain boundaries, triple points, or specific defect types provide a greater pinning potential. Furthermore, this work will explore the influence of domain wall continuity across grain boundaries. An improved understanding of this fundamental ferroelectric material physics may open pathways to improved material models and new ferroelectric materials with engineered microstructures that better consider the impact of pinning sites based on grain size, grain orientation, and proximity to defects.

Chapter 2

Literature Review

2.1 Introduction

The objectives of this thesis were to fabricate polycrystalline ferroelectric thin film samples, characterize their local microstructure, and catalog the property impact of various microstructure features on the domain wall movement and piezoelectric properties. To this end, this chapter provides a review of ferroelectric properties, domain wall movement, Rayleigh behavior, as well as measurement and synthesis techniques according to the cited literature.

2.2 Ferroelectric Materials

A ferroelectric material has a spontaneous polarization which can develop along at least two equivalent crystal directions, and the polarization can be reoriented between the allowed states by an applied electric field.[1,8] The material class has been utilized in memory applications, as its nonvolatility and fast response speeds offer the potential to reduce power requirements in computing.[10] In practice, the two reorientable polarization states can correspond to binary values of "0" or "1" in memory circuits.[10] All ferroelectric material structures exhibit one of the 10 pyroelectric point groups that can demonstrate odd-rank tensor properties such as pyroelectricity and piezoelectricity.[2,8] The perovskite crystal structure in Figure 1-1 is a common host structure for ferroelectricity and is essential to this study.

As a perovskite ferroelectric is cooled from its high temperature phase, the atomic positions shift from the original cubic unit cell positions such that the centers of negative and positive charge are no longer collocated and can produce a dipole moment.[8,10] The directions available for displacement and the magnitude of the displacement vector varies by material phase.[1] For example, on cooling a perovskite ferroelectric through the cubic to tetragonal phase transition temperature, the unit cell distorts to lattice parameters of $c > b = a$. The highly charged cation then shifts away from the body center along the elongated *c*-direction, and the polarization aligns in the [001] direction. In the rhombohedral perovskite phase, the B-site cation displaces along the elongated cell diagonal, producing a spontaneous polarization in the [111] direction of the original cubic cell. The high temperature cubic phase, in contrast, is paraelectric as it does not have a reorientable polarization.[1]

For the ferroelectric phases, two critical properties often encourage their use: a polarization direction that can be altered with a sufficiently large electric field, and a remanent polarization state that persists after removing the driving external field.[2,11] These properties are critical to memory applications, such that the polarization state can be given binary memory values that remains intact in the absence of field. Under an applied field of sufficient magnitude, domains nucleate and grow or shrink in size and cause domain wall motion.[6] The gradual process of domain switching with field is responsible for the prototypical polarization – electric field (P-E) hysteresis loop in ferroelectrics. [1,7] The switching of domains has been reported well below the coercive field of materials as discussed in section 2.5 and 2.6; domain wall motion and switching behavior were measured at electric fields of up to ~45 kV/cm for this study.

The work is in part motivated by the effort to improve models describing how local microstructure factors influence domain wall motion and switching behavior. As one domain grows, the domain wall boundary demarcating the separation from the neighboring domain shifts. This serves both to increase the magnitude of the dielectric or piezoelectric response and to increase hysteresis, and consequently energy loss.

For the purpose of this study, lead zirconate titanate, PZT, was selected for investigation as it is a robust, electrically insulating ferroelectric for which epitaxial growth has been reported on other perovskite structures in spite of large lattice mismatch and external stress. [12-14] Epitaxial growth is pertinent to understanding how the propagated grain structure of an underlying substrate impacts the PZT thin film properties. For polycrystalline samples, the crystallographic orientation of grains is random, which leads to a greater likelihood of a large range of grain boundary orientations for study.[4,5]

In this thesis work, epitaxial $SrRuO_3$ was deposited by PLD as a bottom electrode on polycrystalline $SrTiO_3$ substrates. This layer was then used to template the microstructure of the thin film PZT ferroelectric layer. The polycrystalline $SrTiO_3$ microstructure, therefore, provides triple points with a larger variety of orientations compared to single crystal or bicrystal samples that can be studied for their pinning potential and width of influence.

2.3 Lead Zirconate Titanate

Lead Zirconate Titanate, $Pb(Zr_x, Ti_{1-x})O_3$, or PZT is an industrially important perovskite ferroelectric and the primary material investigated in this work. First developed

at the Tokyo Institute of Technology in 1952, PZT ceramics are in widespread use due to their low cost, high piezoelectric charge constant (d_{33}) and high Curie temperature.[10] Thin film PZT is used industrially for non-volatile memory and microelectromechanical system (MEMS) applications.[10] High-quality PZT films have been grown using multiple thin film deposition techniques.[4,14,15,16,17]

In many cases, the compositions of interest in perovskites are designed around the morphotropic phase boundary (MPB) as they yield strong piezoelectric and ferroelectric properties. [18-22] In PZT, the MPB denotes a phase transition between the tetragonal and rhombohedral ferroelectric phases that is nearly temperature-independent on a temperature-composition phase diagram. For the tetragonal phase, domain walls of 90° and 180° are expected, while for the rhombohedral phase 71°, 109°, and 180° domain walls are expected based on the cation displacement directions and available neighboring domain states. [22] As shown in the phase diagram in Figure 2-1, the paraelectric to ferroelectric

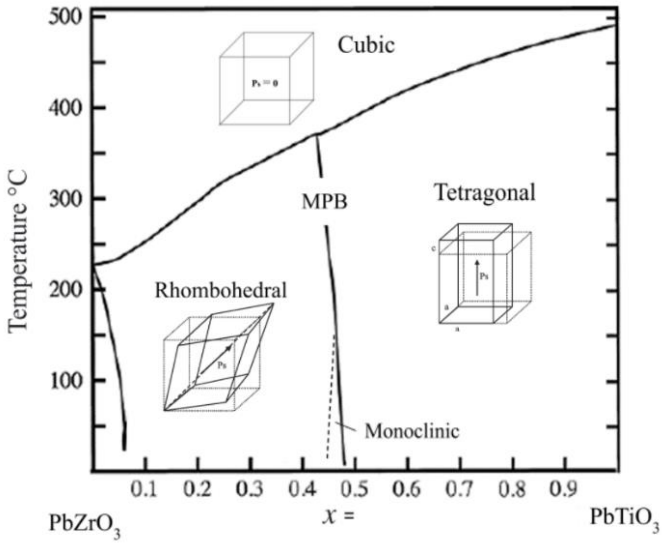

Figure 2-1: PZT phase diagram with unit cell structure schematics embedded adopted from [10]

phase transition temperature associated with cooling from the cubic phase varies from roughly 225°C to 500°C with increasing titanium content. [23] However, the compositional phase boundary that separates the two prominent ferroelectric phases is relatively constant with respect to temperature up until the Curie point.

The piezoelectric activity associated with PZT is maximized near the morphotropic phase boundary composition of $Pb(Zr_{0.52}Ti_{0.48})O_3$.[10,19,22] The large dielectric and piezoelectric constants have been attributed to the abrupt change in crystal structure and flattening of the free energy curve between the two available polarization states around the MPB which facilitates greater polarizability. Jaffe et al. reported maxima in the piezoelectric d coefficients, the electromechanical coupling factor k, and the dielectric properties in the vicinity of the MPB as shown in Figure 2-2 with decreasing coefficient values to either side of the composition boundary. [10]

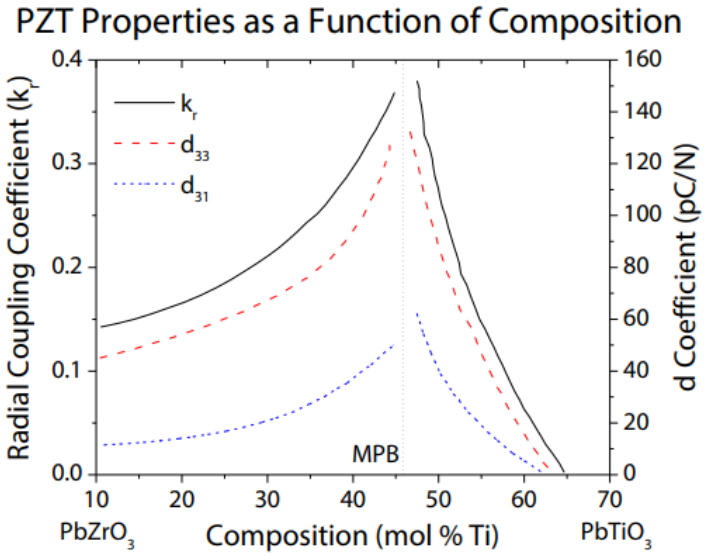

Figure 2-2: PZT properties as a function of composition adopted from [10]

The MPB was extensively characterized in the work of Noheda et al., where an unexpected monoclinic phase was found between the tetragonal and rhombohedral PZT phases.[20] The collected x-ray diffraction data of Figure 2-3 found a phase not compatible with either a rhombohedral phase or with a mixture of tetragonal and rhombohedral phases below 300K.[20] The new phase instead best corresponded to an intermediate monoclinic

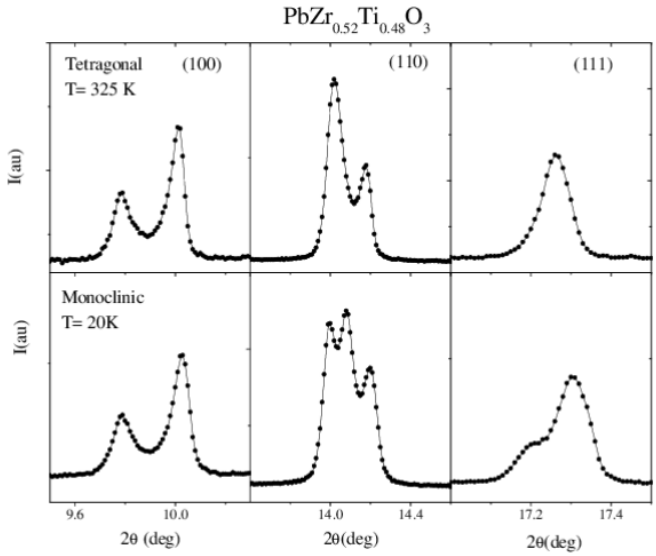

Figure 2-3: X-ray powder diffraction data of PZT sample with x=0.48 demonstrating additional peaks in the low temperature regions suggesting a monoclinic phase. Figure adopted from [20]

phase. Poled PZT samples showed that the monoclinic phase was stable in a narrow composition range and served as a bridge between the tetragonal and rhombohedral structures.[20] The strong electromechanical response may therefore include contributions of increased strain from the intermediate monoclinic structure around this range of compositions.

The grain orientations and propensity for polarization rotation vary with material phase and thus impact the polarizability. Du et al. demonstrated the orientation dependence of the piezoelectric coefficient near the MPB for both rhombohedral and tetragonal phases with the [001] direction exhibiting the highest piezoelectric d_{33}^{eff} coefficient as seen in Figure 2-4.[22]

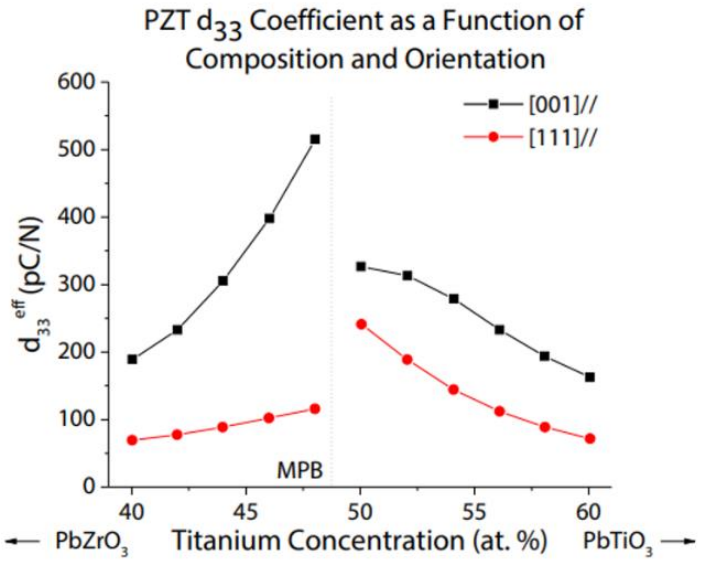

Figure 2-4: PZT d_{33} coefficient as a function of composition and orientation adopted from [22]

2.4 Domain Structure

Domain structures develop in the ferroelectric state and have significant implications for device performance.[1] It is therefore interesting and worthwhile to consider the factors that influence the evolving domain structure. In an ideal ferroelectric, alignment of the spontaneous polarization normal to the surface would cause charge to develop at the surfaces and form a depolarization field; domain structures form to separate

regions of uniform polarization direction and decrease the overall free energy of the system. [22,24] Given that PZT is also ferroelastic, strain also influences the energy balance, and hence the domain structures. The forming domain structure thus arranges in response to several energy contributions including strain, applied fields, and depolarization fields. [26,27,28]

Fousek studied the permissible orientations of ferroelectric domain walls in great detail, noting that uniform strain states should in theory only yield domain walls along planes of mechanical compatibility in the absence of external stress.[26] The cases where no additional elastic strain is created is deemed a permissible wall.[26,27] While they found no ferroelectric crystal samples for which there were no permissible walls, irregular walls did arise when separated by an irregular boundary of large stress, or when separated by another intermediate domain.[26] The majority of the observed incompatible domain pairs were found for spontaneous polarization vectors without a definite orientation with respect to their paraelectric lattice. The two non-permissable domains then meet along a stressed boundary for which the domain switching is expected to be restricted.[26]

90° domain walls and other non-180º domain walls are both ferroelectrically and ferroelastically active.[27] Non-180º domain wall excitation thus changes both the polarization and strain. A head-to-tail 90° domain wall can be seen on the left in Figure 2-5, while the less stable head-to-head walls shown on the right typically arise in high conductivity samples in which mobile carriers move to compensate the energetically costly polarization gradient. Head-to-head domain walls are compensated by fixed charge, which

can induce small-scale imprint phenomenon, where one polarization state is preferred as more energetically favorable locally.[27]

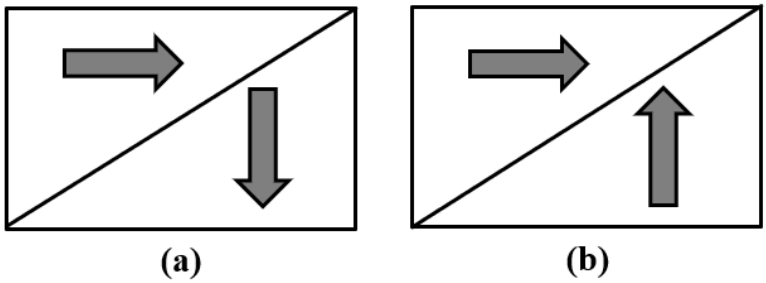

Figure 2-5: Visualization of (a) Head-to-tail domain wall configuration and (b) Head-to-head 90° domain wall configuration

Fousek and Janovec described the elastic energy for differently oriented spontaneous strains in neighboring domains, and the electrostatic energy related to differently oriented spontaneous polarization vectors to describe the energy balance that determines the final domain structure.[26,28] It was found that local strains and local electric fields control the domain state. The domain structure evolves to minimize free energy by adjusting both the domain size and local polarization directions. It was later shown that domain structures often show some relation across grain boundaries, such that the domain structure in one grain can influence that in another several grains distant in PZT ceramics.[19,29,30,31,32]

Depending on the crystal structure, different angles between the polarization directions of adjacent ferroelectric domains can be identified. As the angle between polarities describe a domain wall, the allowed domain wall angles are limited by the available polar directions of a material phase.[19,26,33] 180° domain walls occur when the polarization is anti-parallel in two neighboring domains. These domain pairs can share any plane parallel to the *c*-axis of a tetragonal perovskite material due to the fact that both unit

cells are elongated in the *c*-direction.[27] In contrast, 90° domain walls share the (101) plane due to the requirement for matching strain at the domain wall.[27] 180° domain walls were originally thought to show little to no extrinsic piezoelectric response associated with the domain wall mobility in bulk ceramics as they are purely ferroelectrically active, meaning that they can be excited only by electric fields.[24] However, Bassiri Gharb et al. proved that 180° walls do in fact contribute to piezoelectric response in cases of dynamic poling of thin films.[25] Bassiri Gharb found 180° domain wall motion to be a major source of dielectric nonlinearity and further demonstrated that piezoelectric nonlinearity could appear in thin films cases where only 180° domain wall motion was active. [25]

As one domain grows, the domain wall boundary will shift to accommodate the growth in what is called domain wall motion. Local microstructure features can create pinning centers, though, that act as energy barriers of variable strength to restrict this motion of domain walls.[4,30,34] Figure 2-6 visualizes an applied electric field acting on two domains with oppositely oriented polarization direction (denoted by the arrows). In Figure 2-6, the domain with a polarization direction most nearly aligned with the applied electric

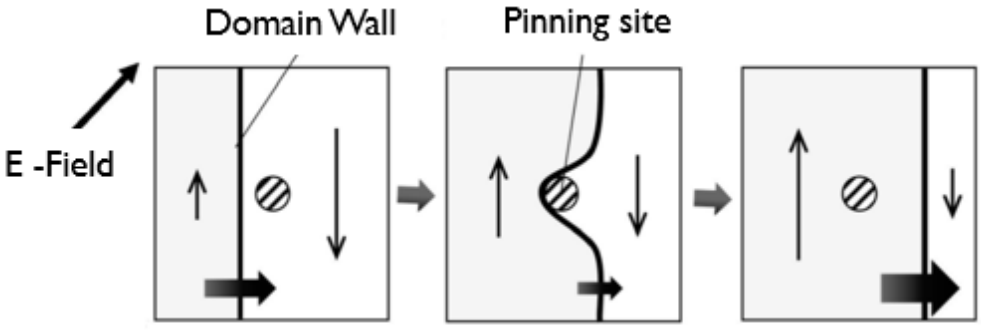

Figure 2-6: Schematic of domain wall movement with respect to a local pinning site. Figure reproduced from [35]

field grows at the expense of the oppositely-oriented domain, and the domain wall separating the two regions shifts to accommodate this growth. In the case of low electric fields, the displacement of domain walls is small and reversible as the field does not supply enough driving force to overcome the energy cost of breaking a domain wall free from one or more pinning centers.[19,31] At higher electric fields the movement can become irreversible; at fields above the coercive field (E_c) the polarization response is strongly hysteretic.[19,30,31]

The extent to which domain wall motion contributes to the net dielectric and piezoelectric responses depends on the ferroelectric distortion. For example, Demartin and Damjanovic quantified the irreversible contribution of domain wall movement to the piezoelectric properties in bulk PZT ceramics. They suggest that the comparatively smaller spontaneous strain of the rhombohedral phase of PZT relative to the tetragonal phase gives rise to higher domain wall mobilities. In some cases, this results in larger dielectric and piezoelectric nonlinearities for rhombohedral samples.[24]

In principle, the degree to which domains grow, move, or remain pinned also depends strongly on the surrounding conditions. Schultheiß et al. studied the domain wall-grain boundary interaction using local coercive voltage mapping on a polycrystalline rhombohedral $Pb(Zr_{0.7}Ti_{0.3})O_3$ ceramic.[31] Figure 2-7 shows a PFM image and local coercive voltage contour plot from this work, in which the red line denotes the grain boundary and black dots represent measurement points.

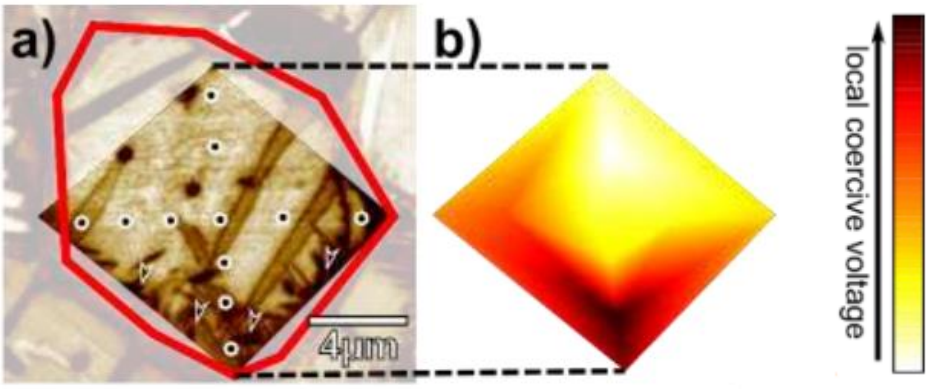

Figure 2-7: a) PFM image of the domain structure. The grain boundary is displayed as a red line, while the measurement points are marked by black dots. The arrows indicate the position of areas with a high density of domain walls. b) Local coercive voltage contour plot corresponding to the measurement points marked in a). The sample had 1.09 domain walls/µm² with an average grain size of 10.4 µm. This figure was reproduced from [31]

The higher reported coercive voltages at the grain boundary area compared to those found at the center of the grain were attributed to the stronger pinning within the influence of the grain boundary regions. [31] The enhanced local coercive voltage is thought to be associated with the strained volumes and higher domain wall density that accompany pinning sites.[36] Additionally, the orientation of a given grain relative to the applied field direction and the grain sizes were found to influence the variability in the domain response.[31]

Marincel's thesis work assessed this grain boundary orientation in greater detail, reporting that at sub-switching fields, grain boundaries had a strong influence on domain wall motion dependent on the misorientation angle between the two grains.[4] It was demonstrated that irreversible domain wall motion in a $Pb(Zr_{0.52}Ti_{0.48})O_3$ bicrystal thin film was reduced up to 450 ± 30 nm away from a 24° tilt grain boundary shown as dotted lines in Figure 2-8.[4] Comparable measurements were made on a subset of tilt/twist grain

boundaries with different degrees of misorientation. It was found that in most cases, the nonlinear response was reduced at a grain boundary. However, the grain boundaries differed in terms of the degree of pinning and the width of influence. [4] In analyzing the ratio of irreversible α and reversible d_{33} components via PFM, Marincel visualized areas of increased domain pinning and nonlinearity near the grain boundary sites. Similarly, Griggio et al. reported decreased domain wall mobility with reduced grain size; an average grain size increase of 110 nm to 270 nm for PZT thin films, was accompanied by an increase in the Rayleigh coefficient α by 100% from 5.3 ± 0.02 cm/kV to 10.6 ± 0.09 cm/kV.[37] Given that α is associated with the irreversible motion of domain walls, the

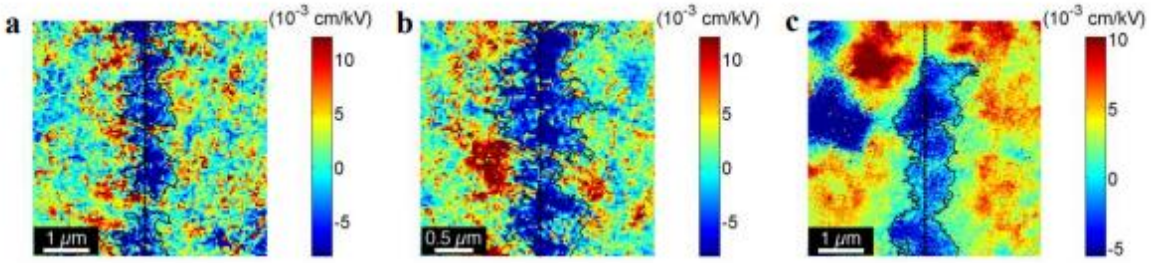

Figure 2-8: Nonlinear response maps measured across the 24° grain boundary denoted by the center dotted line where a) 425 nm thick sample and b) and c) 611 nm thick sample. Adopted from [4]

increase in domain wall mobility with grain size can be thought of as having larger measured areas that are unaffected by nearby grain boundaries. Grain boundary proximity, increased density of domain walls, and increased residual stresses can all decrease the mobility of domain walls.[4,36,37] The local microstructure is thus critical to analyzing domains and their evolution.

2.5 Domain Continuity & Collective Motion

Domain walls often do not move independently of each other, but rather interact to move in clusters that produce a large non-linear response. Bintachitt et al. demonstrated this collective movement, which they described as "domain avalanches".[32] They found that the large-scale clustered movement produces piezoelectric nonlinearity that affects neighboring domains and is heterogeneous at a micron length scale.[32] Figure 2-9 demonstrates the cooperative displacement of domains in which the black dots represent pinning sites and the lines represent the domain walls as the avalanche proceeds from A) to B) to C). It was further noted by Bintachitt et al. that the affected walls do not need to be direct neighbors.

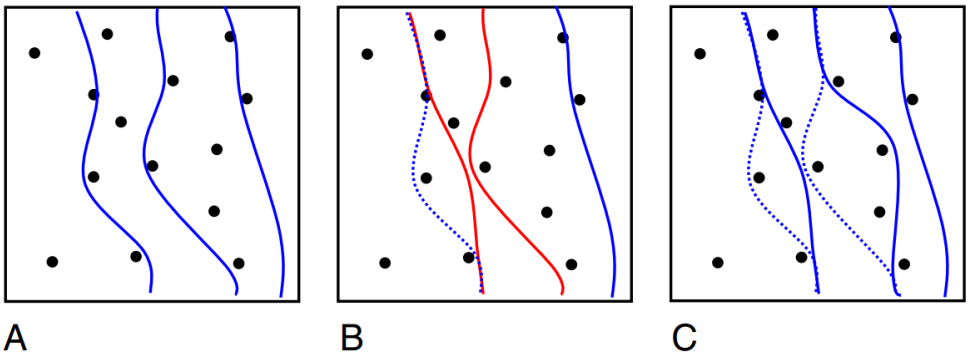

Figure 2-9: Schematic of domain avalanche in which black dots represent pinning sites and the lines represent the domain walls in its progression of domain cluster movement from A to C. Reproduced from [32]

Often the extrinsic contributions to dielectric properties are measured for large sample volumes by analyzing the collective response of the domain walls. The impact and width of influence of individual structure features are, however, difficult to isolate using

these indirect methods, and drive the use of PFM to assess domain motion locally across grain boundaries.

In Figure 2-10, a PFM amplitude image of unpoled PZT with average grain size of 10.4 μm demonstrate cases of domain continuity and lack thereof across the grain boundaries marked in red. Schultheiß et al. also reported that the local variations in the coercive field extend to an average of 10–20 grains in polycrystalline PZT ceramics due to the collective response of the domain clusters.[31] Changes in the domain behavior of polycrystalline samples were attributed to the local strain, domain density, and field heterogeneity across a region.[31]

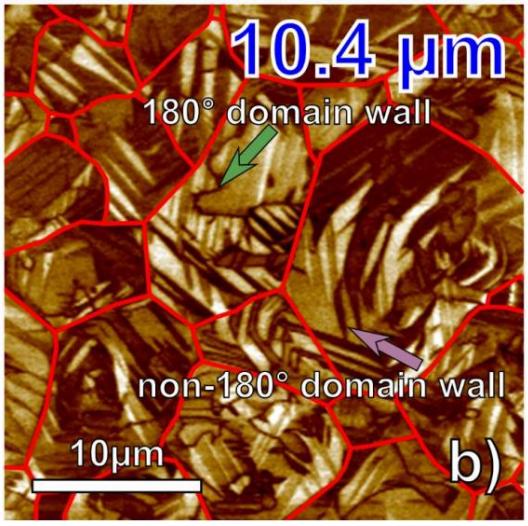

Figure 2-10: PFM amplitude image of unpoled PZT 70/30 with mean grain size of 10.4 μm. Grain boundaries are marked in red while the wedge-shaped features are likely non-180° domain walls, irregular shape are 180° walls [31]

One factor that may influence both the degree of pinning and the width of influence of the grain boundary on domain wall motion is the amount of continuity in the domain structure observed across the grain boundary. Mantri et al. in their review of ferroelectric domain continuity across grain boundaries reported the conditions for continuity in 36

domain wall combinations for tetragonal ferroelectrics.[30] They report that for random grain-grain misorientations, domain continuity is dependent on the ability of the material to compensate ferroelastic strain mismatch and minimize the polarization charge at the grain boundary.[30] For any two domains across a grain boundary, larger uncompensated charge (calculated from the angle mismatch and magnitude of the two spontaneous polarizations) makes continuity less energetically favorable.[30]

In order to assess potential domain clustering in a study of crystal defects on domain motion, Marincel sorted the PFM nonlinear response behavior into high and low response.[4] Based on the average and standard deviation of $\alpha/d_{33,init}$ behavior far from the grain boundary pinning site, it was found that regions of low response (25% of the standard deviation below the mean nonlinear response) appeared most often near the pinning site. This was then used as one means of defining the width of influence of a particular defect on the irreversible motion of domain walls.

2.6 Rayleigh Behavior

It is important to note that domain walls can move at electric fields well below the coercive field in many ferroelectrics. These mobile interfaces contribute to the net dielectric and piezoelectric coefficients. As a result, the observed properties are often the sum of the intrinsic response, as well as the contributions from reversible and irreversible motion of domain walls or phase boundaries.[38] Intrinsic contributions are those that would be present in a single domain single crystal, while extrinsic contributions are associated primarily with domain wall motion and phase boundary motion.[1,2,19,38]

The Rayleigh law is often used to quantify nonlinear dielectric and piezoelectric properties under sub-switching field conditions where domain wall motion is hindered by pinning sites.[38,39,40] Lord Rayleigh's 1887 work describing ferromagnetic minor loops proposed a mathematical description for nonlinearity that is often described as "Rayleigh behavior".[29] This is shown in Equation 1.1, where $M(H)$ is the field-dependent magnetization, χ_{init} is the initial susceptibility, and α is the irreversible Rayleigh coefficient.

$$M(H) = (\chi_{init} + \alpha H_{max})H \pm \frac{\alpha}{2}(H_{max}^2 - H^2) \qquad \textit{Equation 1.1}$$

This description accounts for both the real and imaginary magnetic response, in which the irreversible Rayleigh constant α makes the connection between hysteresis and nonlinearity. This expression is often translated to the dielectric analog, wherein the P(E) loops take the place of field dependent magnetization M(H). This approach was applied to nonlinearity in permittivity and piezoelectric constants by Damjanovic and Demartin.[38]

The Rayleigh Law describes a relationship between field and dielectric constant under sub-switching conditions. The linear relationship between dielectric displacement D and applied alternating electric field E is given as $D = \varepsilon_0 \varepsilon_r E$.[38] This linear relationship fails with increasing field; the Rayleigh law then treats the field dependence of the relative permittivity ε_r of a ferroelectric material with mobile domain walls as a function of the applied field strength.[38] The dielectric Rayleigh response is shown in Equations 1.2 through 1.3. E_0 is the amplitude of the applied field, ε'_{init} the reversible Rayleigh coefficient, α' the irreversible Rayleigh coefficient, and ε'' the imaginary permittivity. ε'_{init}

is associated with the intrinsic lattice contribution and reversible motion of domain walls, while α' represents the irreversible domain wall motion.

Real Dielectric Constant	$\varepsilon' = \varepsilon'_{init} + \alpha' E_0$	Equation 1.2
Imaginary Dielectric Constant	$\varepsilon'' = \alpha'' E_0 = \frac{4}{3}\pi\alpha' E_0$	Equation 1.3
Measured Polarization Change	$\mathrm{P(E)} = (\varepsilon_{init} + \alpha_\varepsilon \mathrm{E}_0) \pm \frac{\alpha_\varepsilon}{2}(\mathrm{E}_0^2 - E^2)$	Equation 1.4

Equation 1.4 shows that the measured polarization change depends on the irreversible extrinsic contributions. It is important to note that an analogous linear relation describes the field dependence of the piezoelectric response $d_{33} = d_{33,init} + \alpha_d E_0$ where α_d represents the irreversible coefficient that drives nonlinearity.[38] The measured changes in these dielectric properties and the local piezoelectric nonlinearity as a function of position provides insight into the domain wall motion and pinning under subcoercive electric fields.

Bassiri Gharb and Lacey describe the 'freezing out' of domain wall motion to remove the thermally activated extrinsic contributions and isolate the intrinsic.[25,41] Without extrinsic contributions, the dielectric properties of PZT are significantly decreased. Bassiri Gharb found that piezoelectric nonlinearity could appear in thin film cases where only 180° domain wall motion was operative; she also showed that as temperature decreased, the domain walls were increasingly pinned.[25,41]

Rayleigh behavior entails domain walls that move across a random energy landscape such as that shown in Figure 2-11 created by dispersed pinning centers with activation barriers to movement that follow a uniform statistical distribution. [29,38,40,42].

It is generally thought that at low fields, domain walls oscillate around a potential energy minima reversibly, as shown in Fig. 2-12. [44,64] Once the applied electric field is sufficient to overcome the pinning energy, the domain wall may irreversibly move from

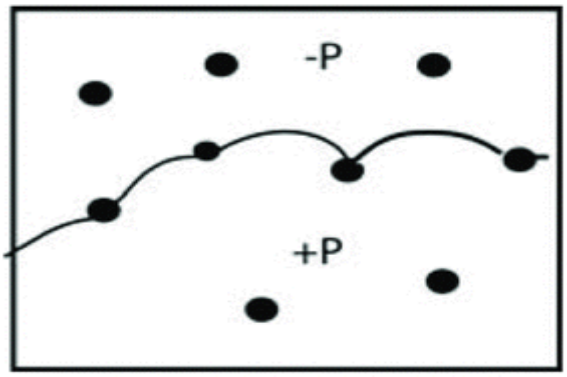

Figure 2-11: Schematic of subswitching conditions. The black points correspond to pinning points; the black line is a domain wall. Adopted from [38]

one minimum to another. The physical description of Rayleigh behavior is therefore mobile domain walls that are hindered by local potential energy barriers.

The dielectric or piezoelectric coefficients are not always linearly dependent on the amplitude of the applied field, however, and so the Rayleigh model does not always apply. Due to this, Damjanovic et al. utilized Preisach type models to describe piezoelectric

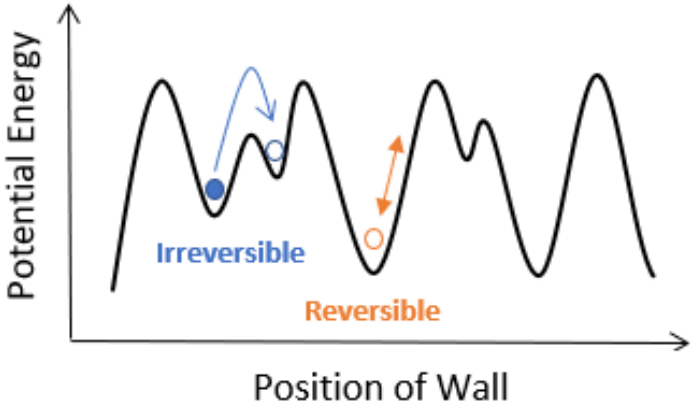

Figure 2-12: Potential energy of reversible and irreversible displacement of domain walls reproduced from [34]

nonlinearity and hysteresis in ferroelectric materials where collected minor loops demonstrate congruency and are rate-independent. [38,42] In other words, it was found that the Preisach description is applicable for hysteretic systems for which any history of operations is wiped out by subsequent loops.

Many lead-based ferroelectric films adhere to Rayleigh behavior up until an applied electric field of roughly a third or half of their coercive field. [32,38,43] Above this field range, the density of domain walls is changed during the measurement, and the Rayleigh law no longer applies. Marincel and Zhang et al., found that the mobile interfaces contributing to nonlinearity in PZT ferroelectrics can be attributed to domain walls and/or phase boundaries.[44]

2.7 Polarization – Electric Field Hysteresis

A characteristic feature of ferroelectric materials is the Polarization – Electric Field hysteresis loop, or P–E loop. The reorientation of the spontaneous polarization with field produces the prototypical P-E loop shape. In linear dielectrics, there is a linear relationship between polarization and electric field.[45-47] A perfect linear dielectric without loss is represented as a straight line in polarization vs. field, whereas a bloated ellipsoidal loop shape can be attributed to dielectric loss.[47] Unlike linear dielectrics which lose their induced polarization after the removal of the field, ferroelectrics retain at least some of the reoriented polarization. For ferroelectrics, domains act in response to a large AC voltage excitation by nucleating new domains and growing the ones for which applied field is well-aligned with one of the allowed polarization directions.[1]

Figure 2-13 shows the P–E loop of a ferroelectric material. +/-P_r refers to the remanent polarization, i.e., the polarization that remains in the material after the electric

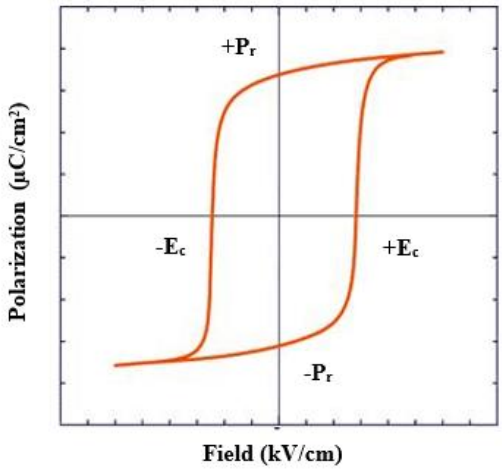

Figure 2-13: Typical hysteresis loop of a ferroelectric material [46]

field is removed. The coercive field +/-E_c represents the electric field required to return the polarization to zero.[8,46] The shape of the hysteresis loop illuminates factors such as necessary poling conditions, leakage currents, and the quality of the electrode-film interfaces.[46] The area inside the P-E hysteresis loop corresponds to energy loss; this is largely attributed to the movement of domain walls through the crystal as an alternating field is applied.[24,25] The sharp tips at the maximum positive or negative polarization values shown in Figure 2-13 suggest samples which are good electrical insulators at high field, while lossy samples often show a bloated, rounded hysteresis.[46]

P–E loops can vary locally around microstructure features when probed with small-area characterization measurements. For example, local hysteresis loops measured in the vicinity of a grain boundary exhibited a strong imprint (e.g. a preferred polarization state, such that the two coercive fields do not average to zero.[45,46] A ferroelectric with imprint behaves as though there is an internal electric field; this can result from aligned defects,

composition gradients, or may develop from the repeated writing of the same polarization state.[47] In polycrystalline samples, there is often significant back-switching as the electric field is reduced due to local elastic or electric fields.[19,32]

2.8 Thin Film Deposition Techniques

Pulsed Laser Deposition or PLD, is a film deposition technique that uses high power laser pulses at high vacuum to ablate material into the gas phase from the surface of a rotating material target; this approach is widely used to deposit epitaxial perovskite films. When the high intensity pulse is incident upon the material target, the material is ejected in the form of a laser-induced plasma plume which is recrystallized onto a hot substrate surface to form a film of approximately the target's composition. [48] Growth is influenced by the laser energy density, the optical absorption coefficient of the target, the pressure of the vacuum system, the substrate temperature, target-to-substrate distance, and pulse duration.[48,49] While this deposition technique is powerful, thin layers grown by laser ablation are prone to physical defects that can result in shorting across the film. Small particles or target fragments known as boulders can appear in the deposited film.[48]

Another technique used to synthesize samples in this thesis is chemical solution deposition (CSD). CSD is a wet-chemical deposition process offering advantages of stoichiometry control and the flexibility of crystallization parameters without the need for high vacuum. In short, CSD via spin coating follows three steps. First the liquid precursor solution is applied on top of the substrate and spun at high velocity. The deposited film goes through a pyrolysis step to dry the coating and remove unwanted organic functional

groups. Finally, the sample is rapidly annealed to crystallize the film. This cycle is repeated several times to achieve a required thickness. Shoghi et al., in their sol-gel synthesis of PZT on glass, found that raising the crystallization temperature to 600 °C leads to a substantial increase in the crystallinity of the perovskite phase where the amount of pyrochlore phase is negligible.[50] Higher temperatures caused a growth in the intensity of pyrochlore peaks.[50] The work of Budd, Dey, and Payne report large remanent polarization in samples grown through CSD processing.[51]

2.9 Epitaxy & Orientation Mapping

Creating reproducible local epitaxy and measuring grain boundaries and triple points is critical to understanding the effect of film microstructure on domain wall motion. While reports of depositions on single crystal and bi-crystal substrates have been addressed in this literature review, these substrates limit the study to a small range of available orientations. To access a wider range of orientations for study, one approach is to optimize the growth on polycrystalline substrates utilizing local epitaxy. Epitaxial growth occurs when the crystalline structure of the underlying substrate material is translated to the growing film and each volume of film reproduces the crystallographic orientation of the underlying grains in matching the atomic spacings and crystal structures.[3,8,48,49] Film and substrates of the same crystal structure are often used to reduce lattice mismatch and strain in the film.

One approach to assessing the orientation of the grown film is to use orientation imaging microscopy (OIM) or Electron Back Scatter Diffraction (EBSD). In OIM, an

electron beam incident on a crystalline material produces a “back-scatter pattern” or EBSPs.[52] Back-scatter band patterns reveal the crystal’s atomic spacing via band intensity, the angle between crystal lattice planes, and sample phase information in the form of Kikuchi patterns.[52] Kikuchi patterns can then be associated to an available orientation of the sample stack and mapped for orientation results.

Figure 2-14 shows an EBSD orientation map of a PZT film deposited on a polycrystalline $SrTiO_3$ substrate. The orientation of each grain, and consequently the degree of misorientation between its neighbors, is readily determined using this method.

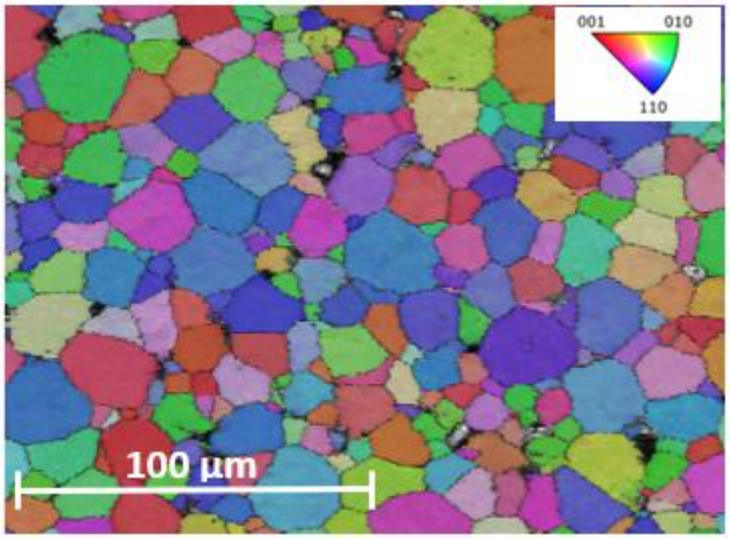

Figure 2-14: EBSD Orientation Map of CSD Deposited 500nm PZT on 30nm $SrRuO_3$

When paired with electron beam lithography to define the electrode patterns at specific areas, sample regions can be studied in relation to their local microstructure and crystallographic orientation.

2.10 Piezoresponse Force Microscopy

Piezoresponse Force Microscopy, or PFM, enables imaging and excitation of ferroelectric domains through use of a conductive probe. PFM utilizes an alternating voltage to deform the material. The deflection of the probe cantilever is then read, similar to atomic force microscopy.[52] Nanoscale phenomena governing the extrinsic contributions through domain wall or phase boundary motion was analyzed using PFM measurements by Bintachitt et al. [32] As seen in Fig. 2-15, Bintachitt demonstrated that the application of band excitation PFM (BE-PFM) could successfully probe the nonlinear converse piezoelectric response at a local scale without artifacts associated with cantilever/film contact and demonstrated that the local response differed with film thickness. [32]

Another related measurement technique is Switching Spectroscopy Piezoresponse Force Microscopy (SSPFM). SSPFM allows the acquisition of multiple hysteresis loops and probes domain nucleation, coercive field, and switching responses mapped in real space.[5, 52, 53] Therefore, ferroelectric behavior on a submicron scale and switching over a large area can be studied. PFM techniques therefore offer the ability to spatially map the polarization dynamics in a material and domain wall-structure interactions.

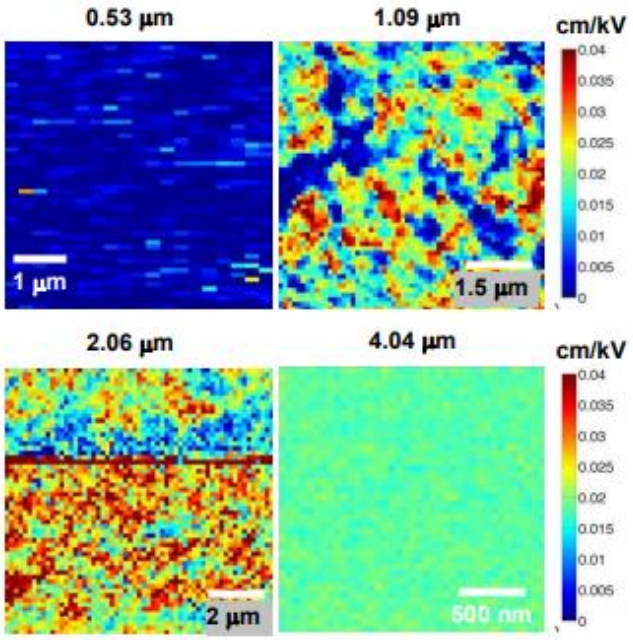

Figure 2-15: PFM Map of PZT nonlinear response as a function of film thickness. Figure from [32]

Using this technique for polycrystalline PZT thin films, Seal et al. demonstrated that local hysteresis loops collected over ~100 nm regions differ significantly from the macroscopic response of the sample, and likened this behavior to a transition from a Rayleigh to a Preisach regime with a spatial inhomogeneity of switching behavior over ~ 1–2 µm.[53] Therefore, switching and domain wall motion cannot be treated as though it were confined to a single grain in PZT samples. The SSPFM maps indicate correlated switching behavior across ~1–2 μm (e.g. the clusters consist of ten to hundreds of grains). [53] This is in good agreement with previous observations of domain structures acting across grain boundaries and supports cascading domain wall behavior. Bassiri Gharb noted the similarity between global dielectric and local piezoelectric nonlinearity measurements, suggesting that the same population of domain walls contribute to both signals.[25]

Chapter 3

Experimental Procedure

3.1 Introduction

This chapter discusses the deposition optimization, patterning and property analysis of $Pb(Zr_{0.52}\ Ti_{0.48})O_3$ (PZT) and $SrRuO_3$ (SRO) thin films. Pulsed Laser Deposition (PLD) deposited PZT film samples were grown either onto Nova platinum-coated silicon substrates for baseline electrical measurements and grain structure studies, or onto a film stack of $SrRuO_3$ bottom electrode deposited on polished polycrystalline $SrTiO_3$ substrates for optimization of local epitaxy. Similar PZT sample thicknesses were prepared using chemical solution deposition, though the $SrRuO_3$ bottom electrode was deposited via PLD in both cases. The goal was to assess whether PZT could be deposited with regions of uniform orientation that mimic the underlying polycrystalline $SrTiO_3$ grains. Local epitaxy from a polycrystalline structure allows for a larger variety of grain orientations to be analyzed compared to growth on single crystal or bicrystal substrates.

The optimized processing procedure for each technique was developed in a stepwise individual variable study. Global electrical measurements such as dielectric permittivity, loss tangent, piezoelectric coefficients, and polarization – electric field hysteresis (P-E) loops were characterized for each sample. In order to assess the film orientation locally, Electron backscatter diffraction (EBSD) mapping was conducted to evaluate local grain orientation. Local nonlinearity measurements were made via Piezoresponse Force Microscopy (PFM) at triple point locations located using the EBSD

map to assess the effects of local microstructure. Given the comparatively large grains of $SrTiO_3$, the investigated grain boundaries can be treated as independent in their effect on local PZT domain structure and domain wall mobility. Thus, it is possible to categorize domain wall pinning with respect to structural features such as grain boundary misorientation angle and grain size.

3.2 Substrate Preparation

When depositing films, it is important to consider the orientation, roughness, and underlying microstructure onto which the material will nucleate and grow. Polycrystalline $SrTiO_3$ substrates provided by Dr. Sridhar Venigalla (Knowles Precision Devices), as received, have a rough surface as shown in Figure 3-1 that may preclude EBSD mapping and PFM measurements.

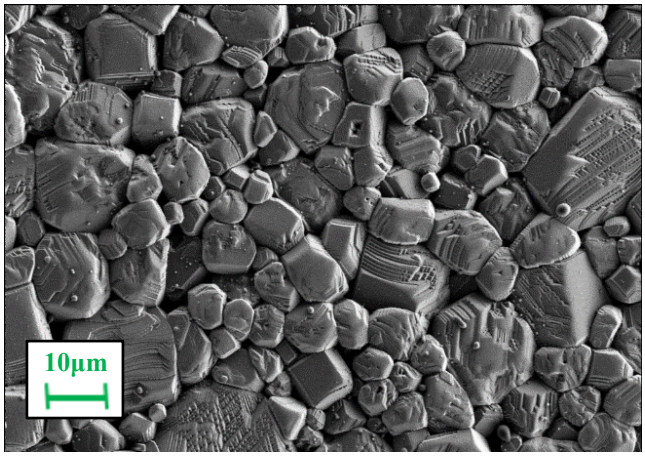

Figure 3-1: Top-down scanning electron micrograph of an unpolished $SrTiO_3$ substrate at 5 kV accelerating voltage and 1000x magnification

To ameliorate this situation, the polycrystalline $SrTiO_3$ substrates were cleaned and mechanically polished using a Multiprep polishing system (Allied High-Tech Products

Inc.) to reduce roughness. The first two polishing steps were conducted successively for one minute each using 600 (P-1200) and 800 grit (P-2400) silicon carbide with a platen speed of 300 RPM, a sample speed of 60 RPM, a down force of 4Lbf, and a constant stream of water as lubricant. These initial polish steps serve to flatten the sample and remove visible roughness. From there a secondary set of two polishing steps, each lasting three minutes, were run using the same rotation speed and down force settings as the initial polish. The two secondary polishing steps utilized a 6 μm grit and a 1 μm grit

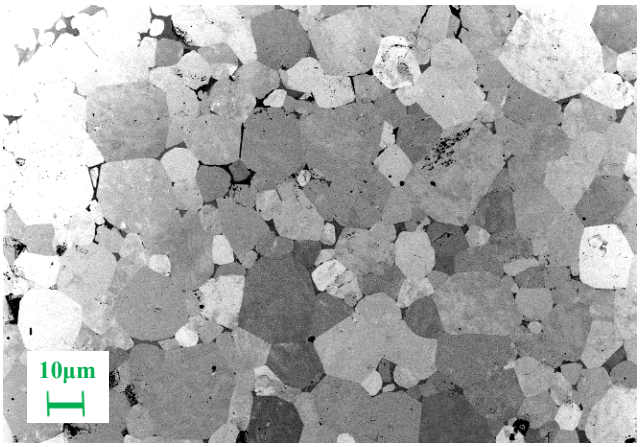

Figure 3-2: Top-down scanning electron micrograph of polycrystalline $SrTiO_3$ substrate polished to 0.05 μm at 2 kV accelerating voltage and 700x magnification

polycrystalline diamond abrasive respectively both utilizing a glycol suspension and Greenlube polishing coolant. The final 1 minute polishing step with 0.05μm colloidal silica grit, 150 RPM sample rotator speed, 150 RPM platen speed, 27 N of down force, and water as a lubricant was then used. After polishing, acetone, isopropanol, and deionized water were then used to clean the surface in successive baths each for a span of 30 seconds in a 5510 Bransonic ultrasonic cleaner. The sample was then dried with a nitrogen gun. The polished $SrTiO_3$ substrate was then rapid thermally annealed at 750°C for 1 minute to remove organics and aid in recrystallization of the surface. A fully polished $SrTiO_3$ sample

surface can be seen in Figure 3-2 via a top-down SEM scan in which the roughness uniformly low compared to that of Figure 3-1. The final surface roughness was quantified using AFM in which an average surface roughness of 18.3 nm was found for PZT deposition via PLD on the fully polished $SrTiO_3$. It was also found that this range of roughness yielded well-defined Kikuchi patterns using EBSD on PZT deposited via chemical solution deposition up to 1000 nm in thickness, compared to roughly 250 nm for PLD deposited PZT. Figure 3-3 demonstrates an AFM scan of PLD deposited PZT on polished $SrTiO_3$.

The Nova $Pt/Ti/SiO_2/Si$ substrates were cleaned prior to deposition using the same acetone, isopropanol, and deionized water successive baths (30 seconds each) in a 5510 Bransonic Cleaning Bath before being dried with a nitrogen gun. A polishing step was not necessary for the Nova substrates given their initial smooth surface finish. The Nova

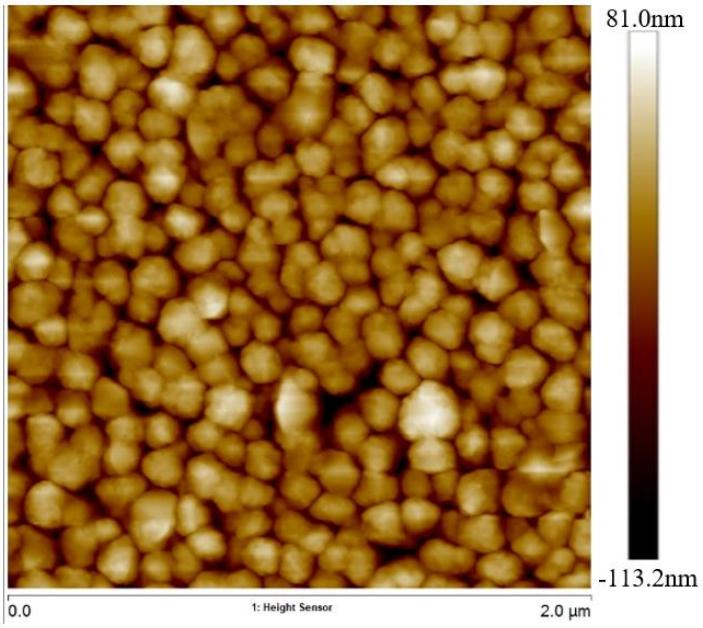

Figure 3-3: AFM scan of 300nm PLD deposited PZT on a polished $SrTiO_3$ ceramic

substrates were instead used to optimize PLD growth trials based on their consistent surface starting point and pre-sputtered platinum bottom electrode.

3.3 Pulsed Laser Deposition

Pulsed Laser Deposition or PLD, uses high power laser pulses under high vacuum to ablate material from the surface of a rotating material target and form a film of the target's composition. PZT thin films and $SrRuO_3$ bottom electrodes were deposited via PLD onto polished $SrTiO_3$ substrates using a KrF Excimer 248 nm laser (Lambda Physik Compex Pro) according to the final process conditions listed in Table 3-1. The optimization used to achieve these conditions is discussed in section 3-4.

A majority of films grown for optimization were deposited on Pt-coated silicon wafers (Nova Electronic Materials, Inc., Richardson, TX). The wafers had a 1 μm thermal oxide, 200 Å titanium buffer layer, and 1,500 Å platinum layer. All Nova wafers were broken to roughly an area of 2 cm x 2 cm using a diamond scribe, cleaned in successive baths of acetone, isopropanol, and deionized water for 30 seconds each in a 5510 Bransonic Cleaning Bath, and dried with N_2 gas to remove any unwanted surface particles before mounting onto the heater. Prior to growth, the back of the wafer was coated with silver paint adhesive (Alfa Aesar, Ward Hill, MA), mounted onto the heater surface, heated to 300°C for ten minutes, and left to cool before aligning the heater perpendicular to the horizontal plasma plume.

Samples deposited on polished polycrystalline $SrTiO_3$ substrates were first mounted onto Nova Pt-coated silicon wafer using the same silver paint adhesive prior to

mounting to the heater. The silver paint was baked on a hot plate at 300°C for five minutes, and air cooled to room temperature to ensure proper binding. Mounting the fragile $SrTiO_3$ pieces onto Pt-coated silicon facilitated removal from the heater without the substrate breaking into pieces. In either substrate case, the substrates were mounted onto the heater using silver paint adhesive heated to 300°C for ten minutes and cooled to 100°C. Shown in Figure 3-4 is a simplified schematic of the Pulsed Laser Deposition tool in which one can see the sample mounted normal to the rotating target.

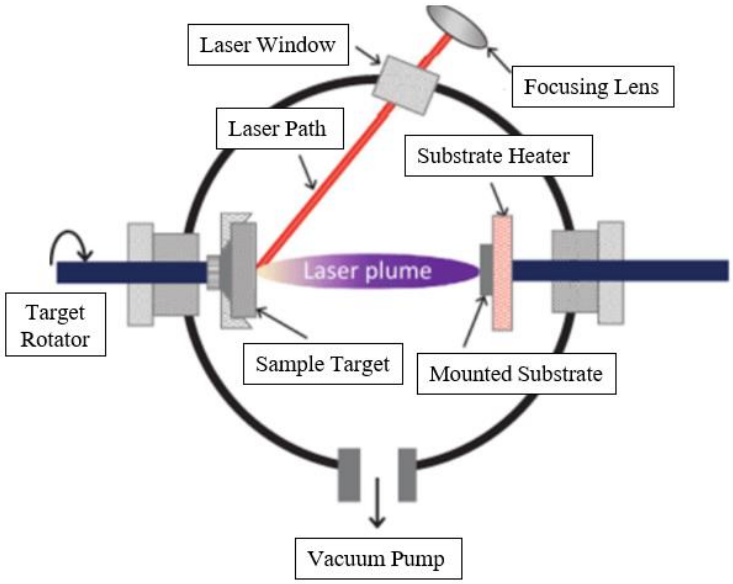

Figure 3-4: Schematic of Pulsed laser deposition system. Adopted from [57] and labelled for clarity

$PbZr_{0.52}Ti_{0.48}O_3$ and $SrRuO_3$ targets 1.5" in diameter from AEM deposition Co. were mounted on stainless steel holders using silver paint, burned out on a hot plate at 300°C for 10 minutes, and cooled to room temperature to ensure it was well bonded. If the paint was incompletely dried, then on subsequent heating, the substrate slid off its mount. The heater is powered by a Hewlett Packard type 6268B dc supply and monitored using a K-type thermocouple embedded under the heater surface.

Prior to each deposition, the target was resurfaced using 800 grit sandpaper until the ablation ring of previous trials was removed. A single laser pulse of the desired energy was then used on the mounted target to calculate an energy density based on the area of the resultant mark. The target surface was then preablated at the desired laser energy and 20 Hz repetition rate for one minute. Polishing and preablating the target surface provided a consistent starting point for growth. Remaining variations in the growth rate occurred due to inconsistencies with plume-substrate alignment from run to run. Once the heater and mounted substrate were aligned normal to the preablation ring at the desired substrate-target distance, the door to the chamber was closed. The closed system was then pumped down to the 10^{-7} Torr pressure range utilizing an Edwards XDS 10 roughing pump to achieve 10^{-3} Torr, and from there a Shimadzu TMP 1002LM Turbomolecular Pump was used to reach 10^{-7} Torr.

Once a chamber pressure of 10^{-7} Torr was reached, the turbo pump was slowed to 20% speed such that a PCI G-1 Ozone generator set to a flow rate of 26.2 mg/min introduced a mixture of 90%O_2/10%O_3 into the chamber until the deposition pressure of 160mTorr for $SrTiO_3$ or 300mTorr for PZT was achieved. The chamber pressure was controlled manually by partially closing or opening the gate valve to the diffusion pump. Once at deposition pressure, the heater was set to the desired temperature and the KrF excimer laser was fired with its cover closed at 10 Hz to warm up the system. The target rotator was also turned on. A specified number of laser pulses incident on the target was then fired with the laser cover opened to achieve a film of the desired thickness. After deposition, heater power and the laser were turned off simultaneously. Then, the vent valve was opened slightly until the chamber pressure reached 100 mTorr. Once the substrate

temperature cooled to 100°C, the system was vented to atmosphere, and the deposited film was removed from the chamber.

When depositing on polycrystalline $SrTiO_3$, the substrate was mounted to a piece of silicon wafer due to its brittle nature. While this added rigidity and served to aid sample removal, an extra thermal resistor must be considered when adjusting the surface temperature to offset the added layer; this is discussed in section 3.5.

3.4 Optimized Pulsed Laser Deposition Parameters

Parameters such as deposition pressure, substrate distance, temperature, laser intensity, and pulse rate were individually modified in pulsed laser deposition trials. In PLD, many of the deposition parameters are correlated such that a change in chamber pressure or target-to-substrate distance alters both the growth rate and the amount of bombardment experienced by the growing film. Thus, a number of individual variable studies of the parameters were made, recognizing some overlap in the parameter's effects. It should be noted that the baseline PZT deposition conditions were tuned from the conditions described in Marincel's thesis, just as the SRO conditions utilized the work of Maria et al. as a starting point.[4,49] From that baseline all variables were held constant except for one independent variable per trial which was varied in a stepwise fashion. The results of these individual variable studies are discussed in Chapter 4 with a focus on optimizing for epitaxy and improved electrical performance. A final PLD process for consistent bottom electrode $SrRuO_3$ on $SrTiO_3$ was developed which enabled local epitaxy with respect to the underlying substrate at consistent growth rates. The $SrRuO_3$ on $SrTiO_3$

deposition via PLD was used for both PLD and CSD deposited PZT films. Strontium ruthenate depositions utilized a laser energy of 1.4 J/cm^2 at 10 Hz, a substrate distance of 8 cm, a deposition pressure of 160 mTorr, and a top surface temperature of 710°C with a heating rate of 10°C/min. Under these conditions, a growth rate of ~10 nm/min was recorded. $PbZr_{0.52}Ti_{0.48}O_3$ film depositions utilized a laser energy of 1.2 J/cm^2 at 12 Hz, a substrate distance of 6cm, a deposition pressure of 300mTorr, and a heating rate of 10°C/min to a growth temperature of 660°C. The deposited films in both cases were cooled to room temperature at 100 mTorr prior to fully venting the system. Under these conditions, PZT films were produced at a growth rate of about 42 nm/min or 0.06 nm/pulse. The $SrRuO_3$ and PZT depositions ran for 11 minutes and 14 minutes, respectively, to achieve 500 nm of PZT and 100nm of SRO. Table 3-1 shows the optimized conditions used to grow 500 nm of PZT on 100 nm $SrRuO_3$ on a polished strontium titanate substrate. Given the use of a single target PLD system, the system was vented and the next target was installed between each layer of the sample stack.

Table 3-1: Optimized pulsed laser deposition conditions for $SrRuO_3$ and PZT films on polycrystalline $SrTiO_3$ substrate stacks (500 nm of PZT and 100 nm $SrRuO_3$)

Composition	Chamber Pressure **[mTorr]**	Substrate Temperature **[°C]**	Target-Substrate Distance **[cm]**	Laser Energy Density **[J cm^{-2}]**	Repetition Rate **[Hz]**	Pulses **[#]**
$SrRuO_3$	160	710	8	1.4	10	6,600
$PbZr_{0.52}Ti_{0.48}O_3$	300	660	6	1.2	12	8,400

For the deposition conditions in Table 3-1, the $SrRuO_3$ films had an average roughness of 19.4 nm on $SrTiO_3$, as shown in Fig. 3-5. For the same deposition conditions

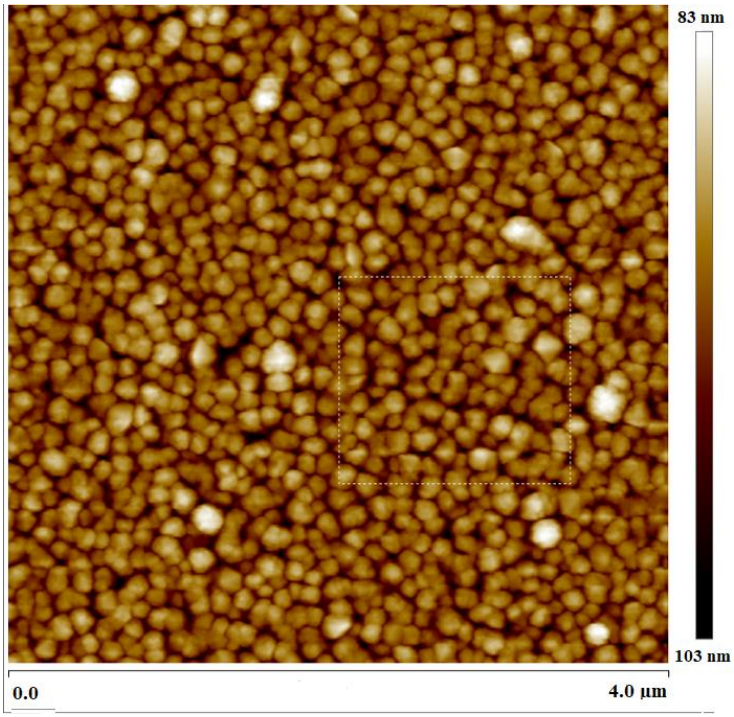

Figure 3-5: AFM scan of 100 nm of $SrRuO_3$ on a polished $SrTiO_3$ ceramic

on 100nm on Nova Pt-coated silicon, the average $SrRrO_3$ roughness was 11.7 nm. The AFM scan of 100nm $SrRuO_3$ on polished $SrTiO_3$ shows a consistent grain structure that resulted in an acceptable average roughness for EBSD mapping (e.g. strong Kikuchi lines were achieved) and PFM measurements.

3.5 Overcoming Additional Thermal Interfaces

It was found that thin pieces of polycrystalline $SrTiO_3$ substrates are fragile and nearly impossible to remove from the heater stage for PLD without breaking. To avoid this difficulty, the strontium titanate ceramics were adhered with silver paint (Alfa Aesar, Ward

Hill, MA) onto a piece of Nova Pt coated Si substrates for increased mechanical robustness (Nova Electronic Materials, Inc., Richardson, TX). This step produced a larger recoverable sample area without breaking, but introduced an additional thermal interface between the heater stage and substrate surface. Thus, it was difficult to predict the substrate surface temperature for depositions on $SrTiO_3$. A simplified schematic of the additional thermal resistor layer is shown in Figure 3-6.

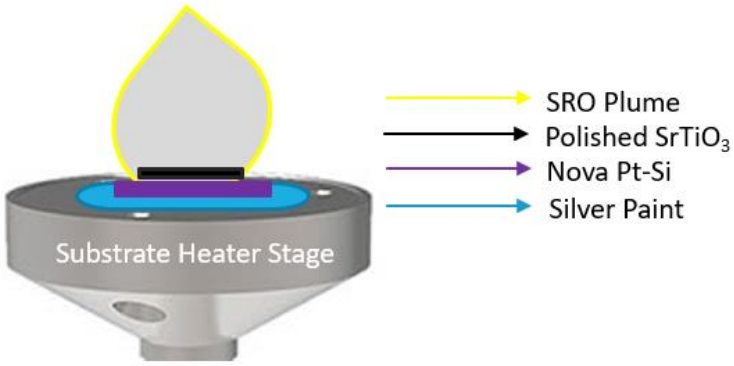

Figure 3-6: Schematic of pulsed laser deposition substrate stack with added thermal resistor associated with mounting the polished $SrTiO_3$ ceramic on a Pt-coated silicon layer

Following the report of Morandi,[56] a series of temperature trials at 50°C intervals was used to measure the offset between the heater set temperature and the $SrTiO_3$ surface temperature. As shown in Fig. 3-7, the offset between the heater set temperature and the top surface temperature for each $SrTiO_3$ substrate deposition was 30°C below ~400°C, and then began to diverge. This temperature offset was presumed to hold under deposition conditions. For all subsequent growths on polycrystalline $SrTiO_3$, the heater set temperature was increased by 30°C relative to growths directly on Pt-coated Si, recognizing that in some case this will result in a growth temperature that is too low. The offset was presumed to be consistent for both $SrRuO_3$ and $PbZr_{0.52}Ti_{0.48}O_3$ film depositions.

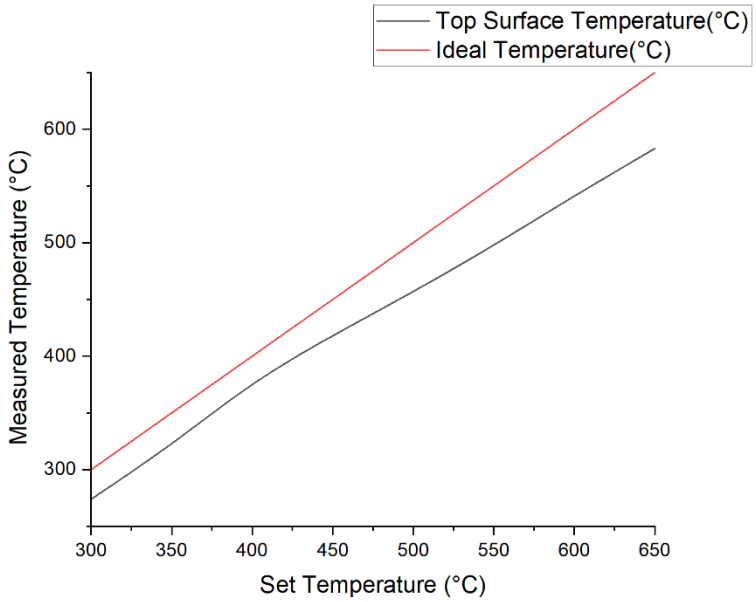

Figure 3-7: Measured surface temperature as a function of set temperature for polycrystalline $SrTiO_3$ on Si on the heater

As will be described in Chapter 4, PLD growth of PZT films using this temperature offset produced rough surfaces and poor reproduction of the underlying $SrTiO_3$ grain structure. As an alternative approach, chemical solution deposition was explored as a processing technique for PZT growth which offers easier temperature monitoring without the need of high vacuum.

3.6 Chemical Solution Deposition

The Chemical Solution Deposition (CSD) of PZT via spin coating allows for accurate composition control, structural homogeneity, and comparatively low roughness relative to that of PLD deposited PZT.[16] In this work, a modification of the processes reported by Trent Borman and Wanlin Zhu were used to prepare the sol-gel PZT films.[55,56]

The substrates were cleaned prior to spin coating as described in section 3.2. The cleaning steps were followed by a dry nitrogen gun and a dehydration step on a 110°C hot plate to evaporate any remaining solvent. The samples were then preannealed at 750°C for 1 min in a rapid thermal processor/annealer (RTP/RTA) (Allwin21 Corp AW 810 RTP) where the temperature was monitored via a thermocouple on the bottom of the wafer.

Mitsubishi Materials Corporation 115/52/48/2 PZT film solution of $PbZr_{0.52}Ti_{0.48}O_3$ with 15 wt% Pb and 2%Nb was then dispensed on to the prepped substrate sample through a syringe with a 0.1μm filter until the entire surface was covered. The samples were spun at 1500 rpm for 30s using a PWM32 photoresist spinner (Headway Research, Inc., Garland, TX) to apply a uniform solution layer onto the substrate surface. The deposited layer was dehydrated and pyrolyzed at 100°C and 300°C on hot plates for 1 and 2 minutes, respectively for each cycle to remove organics. The temperature of each hot plate was monitored using a K-type thermocouple thermometer prior to use.

After pyrolysis of each layer, the sample underwent rapid thermal annealing (RTA) at 750°C for 1 minute with a heating rate of 4°C/s and 2.0 SLPM O_2 gas ambient in the system. This process was repeated until the desired thickness was achieved, with each spin step sequence producing a ~200 nm layer of film for a solution molarity of 0.75 M. The pyrolysis and crystallization steps utilized offered reproducible epitaxial growth and a comparatively smooth sample surface at PZT thicknesses up to 1000 nm.

3.7 Structural Characterization

Prior to patterning top electrodes for electrical measurements, the structure of each deposited film was analyzed. The characterized samples included PZT deposited via Pulsed Laser Deposition (PLD) and Chemical Solution Deposition (CSD) at thicknesses of 250 nm, 500 nm, and 1000 nm grown either onto platinum coated silicon substrates, or onto $SrRuO_3$ on polished polycrystalline $SrTiO_3$ substrates. X-ray Diffraction (XRD) was employed for phase analysis, cross-section Scanning Electron Microscopy (SEM) for film thickness measurements, top-down SEM for grain size measurements, and Electron Backscatter Diffraction (EBSD) to map the grain orientation and collect proof of local epitaxy. In utilizing these characterization techniques, the optimization of film deposition could be carefully tuned, and the sample structure could be mapped for analysis of local pinning sites. Details for each characterization technique are provided in the following sections.

3.8 X-ray Diffraction

The crystallographic orientation and quality of film crystallinity were determined in part by using an Empyrean III diffractometer (Malvern PANalytical, Malvern, United Kingdom) in the Bragg-Brentano geometry. Cu - K_α radiation and a programmable-Z manual phi stage were used to collect measurements in the range of 10° to 75° (2θ) at a rate of 2° 2θ/min. Copper-K_α radiation generated at 45 kV and 40 mA was utilized with

divergence slit set to 1/4° and anti-scatter slits set to 1/2°. The recorded data yielded information on the relative intensity of the crystallographic peaks and the "sharpness" of the peaks. Table 3-2 shows the standard diffraction profiles used in JADE analysis software from the International Center for Diffraction Data PDF 2022 database. Data from the PDF files serves to normalize the textured film data against a randomly textured sample for peak fitting.

Table 3-2: Powder diffraction file numbers from International Center for Diffraction Data PDF 2022 database.

Material	PDF #
$Pb(Zr_{0.52}Ti_{0.48})O_3$	01-070-4060
$PbTiO_3$	00-040-0099
$SrTiO_3$	04-001-7415
$SrRuO_3$	04-005-7020

3.9 Scanning Electron Microscopy

Dielectric response and piezoelectric coefficients require accurate knowledge of the film thickness. Scanning electron microscopy was employed both to assess the sample microstructure features and to characterize the film thicknesses. Grain boundaries and surface defects were analyzed using a Zeiss Merlin Field Emission Scanning Electron Microscope (Zeiss Co., Oberkochen, Germany) in a top-down orientation. An example of grain structure analysis is shown in Figure 3-8 in which the comparatively large grains of $SrTiO_3$ are shown with respect to the grain structure of the CSD PZT on top exhibiting scale bars orders of magnitude smaller.

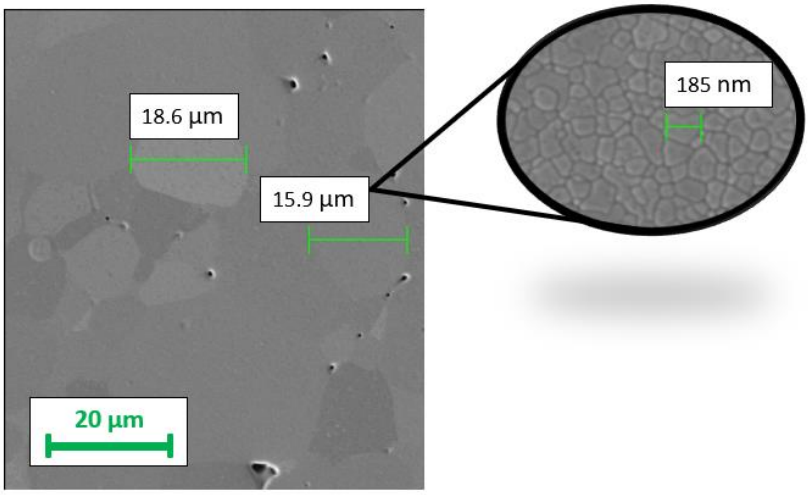

Figure 3-8: Top-down SEM image of $SrTiO_3$ and $PbZr_{0.52}Ti_{0.48}O_3$ grain structure for size comparison

Samples were mounted to the SEM sample holder using clean room kapton tape. A nitrogen blow-off gun was then used to remove particulates prior to pumping down the chamber. For cross-section analysis, the sample was cleaved near the center of the sample area, to avoid errors associated with thickness nonuniformity from the sample center to the sample edge. Figure 3-9 shows an example of a cross-sectional scan. This film thickness

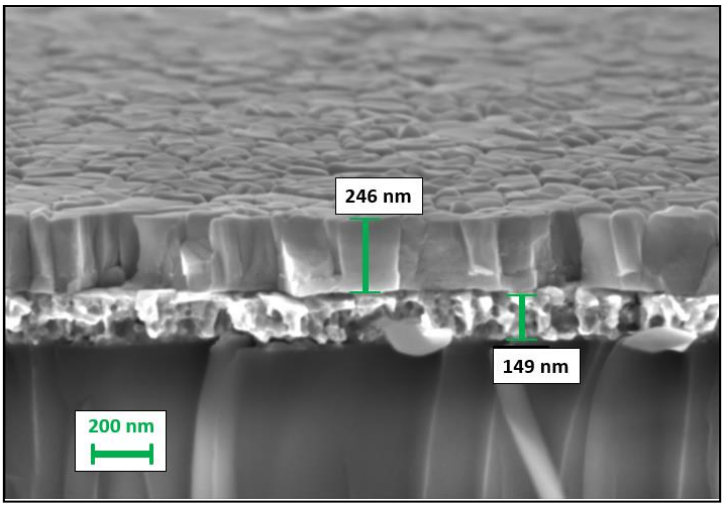

Figure 3-9: Cross-sectional scanning electron micrograph of PLD deposited PZT on $SrRuO_3$ on $SrTiO_3$

measurement technique was essential to determining the electrical properties of deposited films.

3.10 Patterning Top Electrodes

To enable electrical measurements, top electrode patterns of known areas must be deposited onto the sample stack. Prior to patterning, each sample was cleaned in successive baths of acetone, isopropanol, and deionized water each for 30 seconds and then dried with a nitrogen gun. The electrode areas were then patterned via a photolithographic lift-off process in which LOR5A photoresist (Microchem) was dispensed onto the sample dynamically (during spin) using a micropipette on a sample spinning at 900 rpm. The PWM32 photoresist spinner (Headway Research, Inc., Garland, TX) then distributed the resist evenly across the sample surface by increasing the spin speed to 4,000 rpm for 45 seconds. The remaining resist was then baked for two minutes on a 180°C hot plate and left to cool. A secondary layer of SPR3012 (Dow Electronic Materials) was spun with the same conditions as LOR5A but was baked at 95°C for 2 minutes on top of the LOR-5A layer. The coated sample was then exposed to UV light through a chromium on glass lithography mask using a MABA6 Gen 4 Exposure Tool (Suss Microtec, Garching, Germany) with a wavelength of 405 nm and a light intensity of 180 mJ/cm^2. The exposed areas of resist patterned were 1000, 60, 400, or 200 μm in diameter.

MF CD-26 developer (1-5% Tetramethylammonium hydroxide (TMAH) in water – Dow Electronic Materials) was then utilized for 70 seconds to develop the exposed photoresist areas and reveal the underlying PZT. The develop step was followed by a

deionized water rinse to stop the reaction. An oxygen plasma ash step using an M4L RF Gas Plasma System (PVA TePla Corona, California) with gas flow rates of 50 sccm He and 150 sccm O_2, at a pressure of 550 mTorr, and an RF power of 200 W for 1 min then served to remove any remaining resist in the patterned areas. The patterning process described produced discrete sample areas onto which platinum can be sputtered as a top electrode. In some cases, EBSD mapping was first used to map the exposed electrode regions prior to sputtering the top electrode.

Using a secondary photolithography step, a set of crosshairs was created around the electrode to act as cardinal directions for PFM scan alignment. The MLA 150 advanced maskless aligner from Heidelberg instruments (Heidelberg, Germany) was utilized for this secondary photolithography step after platinum deposition. Samples were first spin coated with LOR5A photoresist (Microchem) dispensed dynamically with a micropipette on a sample spinning at 900 rpm using the PWM32 photoresist spinner (Headway Research, Inc., Garland, TX); the spinner was then accelerated to the final spin speed to 4,000 rpm for 45 seconds. The remaining resist was baked for two minutes on a 180°C hot plate and left to cool. A layer of SPR3012 (Dow Electronic Materials) was spun on top of the LOR-5A layer with the same conditions as LOR5A but was baked at 95°C for 2 minutes. Once the resist layers were dried, the sample was aligned in the MLA lithography tool. From there an exposure map developed by Pannawit Tipsawat was loaded into the MLA software and a region of appropriate size for the map was selected. The exposure map included a grid of bonding pads for wire bonding that overlapped the platinum areas, labels for each column and row of electrodes, and a set of cross-hair markers surrounding each 200 μm electrode. Once aligned, the resist was exposed to a dose of 180 mJ/cm^2 for 90 seconds,

followed by a develop step using MF CD-26 developer (1-5% tetramethylammonium hydroxide (TMAH) in water – Dow Electronic Materials) for 60 seconds to reveal the patterned area. The resist was then exposed to an oxygen plasma ash step using an M4L RF Gas Plasma System (PVA TePla Corona, California) with gas flow rates of 50 sccm He and 150 sccm O_2, at a pressure of 550 mTorr, and an RF power of 200 W for 1 min then served to remove any remaining resist in the patterned areas. Approximately 500 nm of gold was sputtered into the exposed areas areas of each sample (Kurt Lesker CMS-18, Pittsburgh PA) using a power supply setpoint of 200 W forward power, 450 V, ~ 0.425 A and chamber conditions of 4.7 mTorr and 22°C for 400 seconds. The wirebonding onto the newly deposited gold pad is described in section 3.15

The fiducial markers produced in this photolithography steps facilitated orientation of the EBSD maps to characterize the grain structure features and ascertain their impact on electrical properties. In particular, this step allowed PFM measurements with known electric field excitations to be performed on previously characterized triple points and grain boundaries.

3.11 Electron Backscatter Diffraction

Orientation imaging microscopy (OIM) or Electron Backscatter Diffraction (EBSD) was used to prove local epitaxial growth to the underlying substrate, and to analyze the films for crystallographic orientations and grain boundary location prior to depositing the top electrode. EBSD uses a scanning electron beam to strike a crystalline material at an angle and record the Kikuchi diffraction patterns.[52] These provide local information on

the crystal orientation and can be overlayed on the original SEM image to map the grain orientation as shown in the large area EBSD scan of Figure 3-10. In the top right of Figure 3-10 is an Inverse Pole Figure (IPF) key which is used to color code the grain orientations; a cubic perovskite cell was used. The 30 nm thick $SrRuO_3$ film was grown using PLD deposition conditions described in Table 3-1, the 500 nm PZT was grown using the conditions described in section 3.6. The angle between any two grains was calculated using the Aztec crystal software.

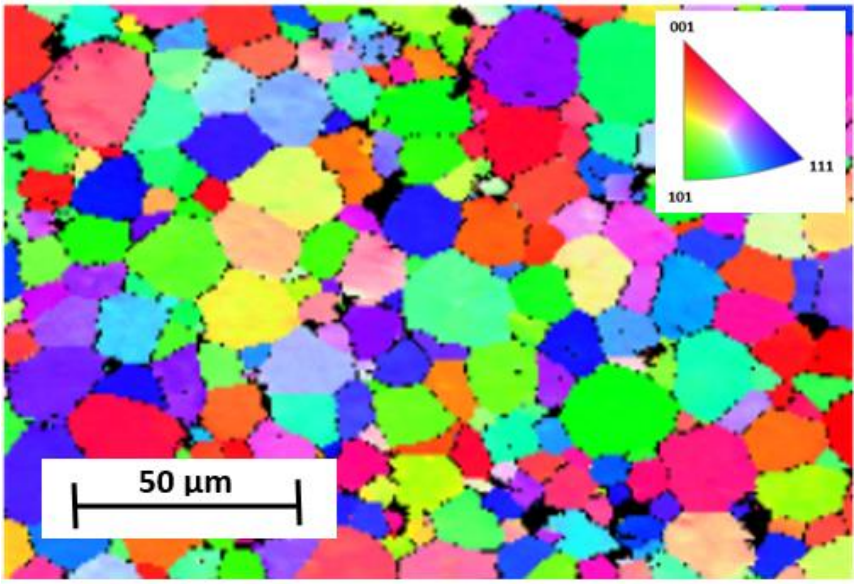

Figure 3-10: Large area EBSD scan of 500 nm of PZT deposited via CSD on 30 nm $SrRuO_3$ deposited via PLD on polished $SrTiO_3$ substrate

For each sample deposition, EBSD was utilized in a small sample area scan to ensure that consistent Kikuchi patterns could be collected that mimic the orientation of the underlying substrate. Then, prior to depositing the top electrode, the specific electrode areas defined through lithography were mapped.

To define the electrode areas via lithography, the MLA 150 advanced maskless aligner from Heidelberg instruments (Heidelberg, Germany) was utilized. Samples were first spin coated with LOR5A photoresist (Microchem) dispensed dynamically with a micropipette on a sample spinning at 900 rpm using the PWM32 photoresist spinner (Headway Research, Inc., Garland, TX); the spinner was then accelerated to the final spin speed to 4,000 rpm for 45 seconds. The remaining resist was then baked for two minutes on a 180°C hot plate and left to cool. A layer of SPR3012 (Dow Electronic Materials) was spun with the same conditions as LOR5A but was baked at 95°C for 2 minutes on top of the LOR-5A layer. Once the resist layers were dried, the sample was loaded into the MLA lithography tool vacuum chuck and aligned. From there an exposure map developed by Pannawit Tipsawat was loaded into the MLA software and a region of appropriate size for the map was selected. Figure 3-11 shows the utilized MLA exposure map in which a grid of 200 μm electrodes were uniformly spaced with each column and row of electrode areas labelled for clarity. Alongside these electrode areas was a set of cross-hair markers surrounding each 200 μm electrode; the tilt offset of the collected EBSD map could be calibrated to the future PFM scan based on orienting the crosshair with respect to the EBSD scan crosshair tilt.

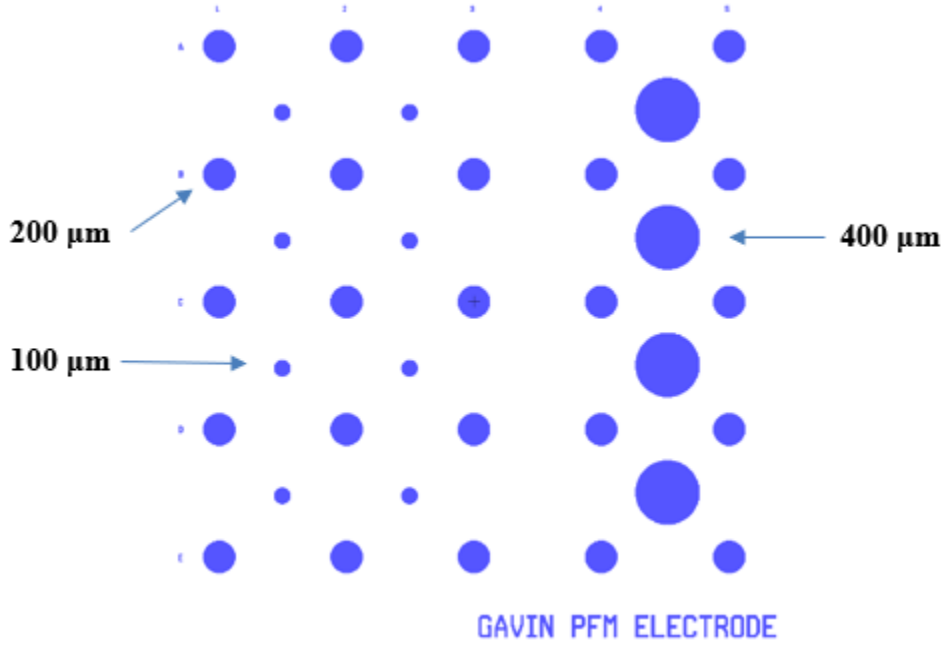

Figure 3-11: MLA electrode exposure map of uniformly spaced 200 µm electrode areas in a labelled grid formation

The prepared exposure map was aligned roughly to the sample center, and an exposure dose of 180 mJ/cm^2 was rastered along the mapped area. The exposed areas were then developed away using MF CD-26 developer (1-5% tetramethylammonium hydroxide (TMAH) in water – Dow Electronic Materials) for 60 seconds. The resultant exposed PZT area was checked visually using blue-light filtered optical microscope to ensure the exposed electrode circle areas and adjacent fiducial markers were well defined with the resist fully developed away. The developed electrode area of the PZT top layer is then ready for EBSD analysis, Figure 3-12 is an example of the electrode area scanned using

EBSD on a region of PZT where the resist has been developed away, but platinum has not yet been deposited as a top electrode.

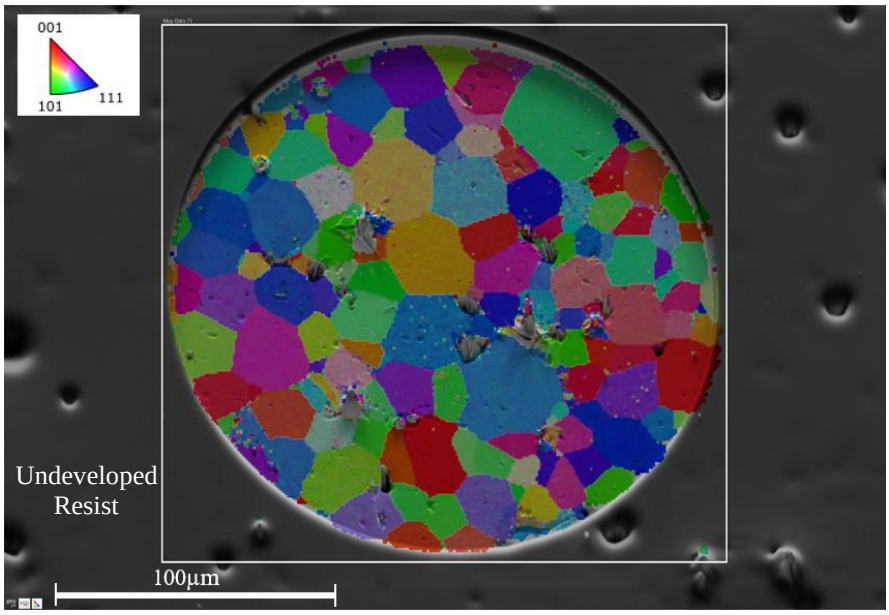

Figure 3-12: EBSD scan of exposed electrode area of 1000 nm PZT/200 nm $SrRuO_3$ on polished $SrTiO_3$ prior to platinum sputtering

Given that understanding the orientation relation to local electrical properties motivates this study, pairing local electrical measurements to these EBSD maps is crucial as it enables PFM analysis of known grain boundary orientations. The consistent ability to map via EBSD is therefore a primary consideration for deposition optimization, as the initial EBSD scan prior to depositing resist demonstrates whether a sample can be utilized in PFM.

3.12 Sputtering of Top Electrodes

500 Å of platinum was deposited as a top electrode on each of the patterned areas using a bottom-up sputter system (Kurt Lesker CMS-18, Pittsburgh PA). The patterned

sample was first mounted using cleanroom Kapton tape. The chamber was then pumped down, and sample was raised to its processing position. The sputtering of platinum was done at a chamber pressure of $2x10^{-3}$ Torr Ar and a substrate heater temperature of 18.5°C. The plasma was struck through the application of 100 W of forward power and 200 V of DC bias at ~ 0.018 A. The system was then vented to reveal a fully coated platinum surface. When the platinum thickness was critical, as is the case with PFM, the deposition rate was characterized immediately prior with a "witness" sample sputter and a cross-section SEM measurement.

Liftoff was then performed to leave behind well-defined circular top electrodes for electrical measurements. An initial acetone rinse removed the majority of unpatterned Pt. The liftoff was then completed by ultrasonication for 60 seconds in acetone. The sample was then placed into a beaker of PRS 3000 developer in an 80°C water bath for 15 minutes to remove remaining resist, followed by a short DI water bath to stop the reaction. Finally, to improve adhesion of the top electrode to the PZT surface each sample underwent a rapid thermal anneal (RTA) step at 550°C for 1 min with a heating rate of 4°C/s and ambient chamber conditions (no gas flow).

3.13 Bottom Electrode Etch

In order to expose the bottom electrode, the sample film stack was etched. Microposit 1812 photoresist (Dow Electronic Materials) was first applied to the entire sample surface using a dynamic 4000 rpm spin recipe for 45 seconds on the PWM32 photoresist spinner (Headway Research, Inc., Garland, TX). A cleanroom swab coated in

acetone was used to remove the spun-on photoresist on one of the sample's corners. The remaining photoresist was baked at 100˚C for ~ 90 seconds or until visibly dry. The exposed corner of PZT was then etched to expose the $SrRuO_3$ bottom electrode with alternating buffered oxide etch 10:1 (40% w/w NH_4F] : [49% w/w HF]) and hydrochloric acid (36% w/w HCl) droplets applied via micropipettes in accordance with the experimental procedure of Trent Borman.[56] The resultant reaction was stopped after 5 to 10 seconds using a deionized water bath, and inspected visually for color change until the dark grey appearance of $SrRuO_3$ could be seen. After each cycle, the exposed area was inspected using an optical microscope. A final post clean of acetone, isopropanol, deionized water and a dry nitrogen gun removed the remaining 1812 photoresist and completed the sample processing.

3.14 Electrical Measurements

The capacitance, dielectric constant, and loss tangent were measured using a Hewlett Packard Model 4284 Precision LCR Meter (Hewlett Packard, Palo Alto, California). Point probes were used to make contact to the top platinum electrode and the exposed bottom electrode. All measurements were collected on 200 μm diameter top electrode areas and driven from the exposed $SrRuO_3$ bottom electrode, unless otherwise specified. The LCR meter was set to C_p-D and run in the frequency range of 100 Hz to 1 kHz at 30mV oscillating voltage. The capacitances were then used to calculate the dielectric permittivity, using the equation shown in Equation 3-1, where C= Capacitance, ε_0= permittivity of vacuum (8.854×10^{-12} F/m), A= electrode area, and d= thickness of the

film stack. The thicknesses used to calculate the dielectric constant from the capacitance were obtained from cross-section SEM images and ellipsometry data collected prior to electrical analysis.

$$C = \frac{\varepsilon_o \varepsilon_r A}{D}$$ Equation 3-1

For PFM measurements the probe was rastered along a square area about a triple point of interest and measured displacement at 50 nm increments. The sample was pre-poled at three times the coercive field prior to each measurement, and care was taken to ensure that the piezoelectric phase was uniform across the scan area. The amplitude of the field applied for measurement was typically ~45 kV/cm to assess domain wall motion and measured nonlinear switching behavior; near the resonance frequency of the cantilever, this field was low enough that the samples stayed in the Rayleigh regime. Polarization-Electric field measurements of the hysteresis loops (P-E loops) were characterized using an RT66A Standardized Ferroelectric Test System (Radiant Technologies Inc. Albuquerque NM). Point probe contacts were used to connect the top and bottom electrodes. To determine the breakdown strength, the bottom electrode contact was driven at a starting applied field of 100 kV/cm for initial hysteresis and the field was then increased in 100 kV/cm increments until electrode failure. All polarization-electric field measurements were made at a period of 10 milliseconds. The Radiant Technologies Vision Software was then used to output the raw data collected. The data were plotted to confirm ferroelectricity and used to determine the remanent polarization (P_r) and coercive field (E_c).

3.15 Wirebonding

After global electrical measurements were collected using an LCR probe station, gold contact pads were deposited to partially overlap the previously sputtered platinum electrode areas. The patterning of the platinum electrode areas and fiducial crosshair markers used for alignment is described in section 3.11. The secondary lithography step for gold pads enabled easier wire bonding to the package which facilitates low mechanical noise electrical contact in the PFM measurements. Wire bonding was conducted using a Kulicke and Soffa 4123 system (Horsham, PA).

To pattern wire bonding pads, LOR5A photoresist (Microchem) was dispensed dynamically onto a sample spinning at 900 rpm and accelerated to a final spin speed to 4,000 rpm for 45 seconds using the PWM32 photoresist spinner (Headway Research, Inc., Garland, TX). The resist was then baked for two minutes on a 180°C hot plate and left to cool. A secondary layer of SPR3012 (Dow Electronic Materials) was dynamically dispensed at 900 rpm, accelerated to 3000 rpm, then baked at 95˚C for 2 minutes on top of the LOR-5A layer before being left to cool.

A Heidelberg MLA 150 advanced maskless aligner was programmed to expose a series of square areas based on the spacing of the 200 µm electrodes of Figure 3-11. The MLA map of square pads were then aligned with the previously exposed alignment crosshairs such that they were uniformly positioned to overlap the bottom of each of the 200 µm circles on the electrode grid. The sample was then exposed and developed as described above. 500 nm of gold was then sputtered (Kurt Lesker CMS-18, Pittsburgh PA) onto the exposed areas using a power supply setpoint of 200 W forward power, 450 V, ~

0.425 A and chamber conditions of 4.7 mTorr and 22°C for 400 seconds. Shown in Figure 3-13 is an example electrode area, the tilt correction crosshairs and the gold pad ready to mount to the bonding package.

To mount the prepared samples, they were first raised in height by adhering the sample backside to a glass slide with super glue to raise the surface flush with the bonding

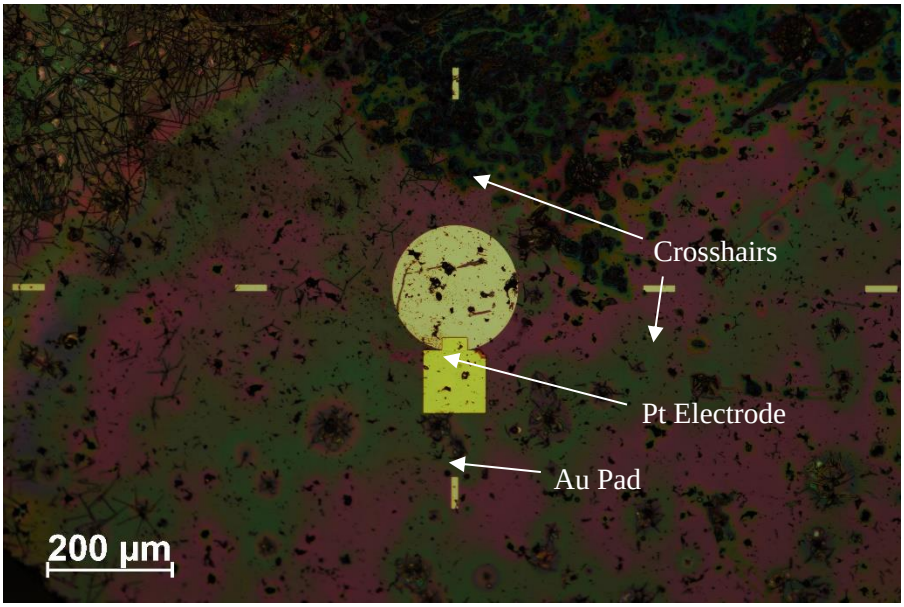

Figure 3-13: Electrode area with patterned gold pad for electrical contact via wirebonding

pads. Raising the sample in the package was necessary otherwise the PFM probe could not reach each electrode area. Once mounted, the 25 µm bonding Cu wire was routed through the bonder feeder and clamped on the end with roughly 1 cm extended past the bonding tip. Shown in Figure 3-14 is a schematic of the steps utilized for bonding. In preparation of the bonding step, the stage and package are first heated to 70°C, the wire is extended beyond the clamp, and the system set to 30 V. In step two, a downforce of 4 Lbf for 5 seconds was applied to the wire on the electrode contact pad and held for roughly two seconds to ensure strong contact.

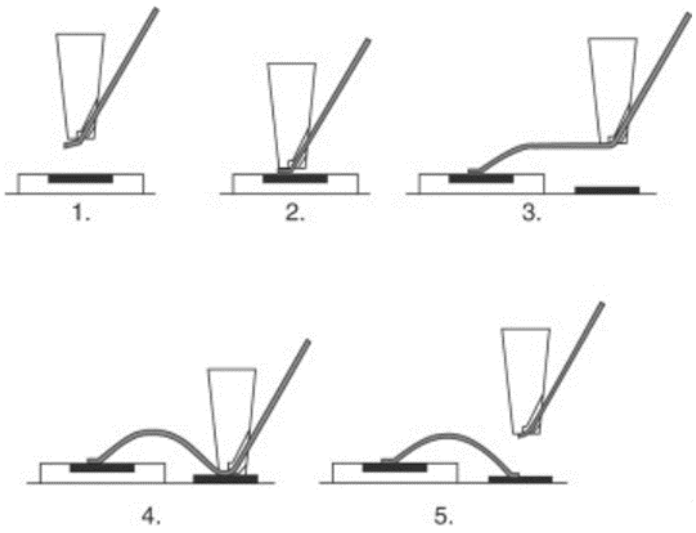

Figure 3-14: Schematic of wirebonding steps to achieve electrical contact [58]

The attached wire is then unclamped from the spool head, pulled to the bottom electrode pad, and bonded under the same force and time conditions as step two for the bond to the package. This process was repeated for each electrode of interest.

Chapter 4

Results and Discussion

4.1 Introduction

This chapter presents results on the synthesis and characterization of $PbZr_{0.52}Ti_{0.48}O_3$ films grown with local epitaxy on polished polycrystalline $SrTiO_3$ substrates with a $SrRuO_3$ bottom electrode. The PZT films were deposited using either chemical solution deposition (CSD) or pulsed laser deposition (PLD); the $SrRuO_3$ bottom electrode was deposited via PLD. It should be noted that PZT films were also deposited onto Nova platinum-coated silicon substrates for baseline electrical measurement comparison and used for grain structure analysis to aid process optimization. Both PLD and CSD produced PZT samples of high relative permittivity (>1000), high remanent polarization (>20 $\mu C/cm^2$), and a low loss tangent (< 5%) after optimization. PZT film thickness of most samples were approximately 1 μm unless otherwise stated.

As described in Chapter 3, areas of the samples that represent top electrodes were mapped using EBSD prior to platinum sputtering, such that grain boundaries of known orientation and triple point locations could be revisited for local measurements using PFM. PFM measurements offer the ability to assess piezoelectric nonlinearity about specific regions, and consequently quantify changes in the motion of domain walls at increasing distances from a grain boundary or triple point. Through process optimization and film analysis, this work details how the piezoelectric properties of polycrystalline thin film samples vary locally and catalogs the pinning potential of various grain boundary orientations in PZT films.

4.2 PLD Deposition Optimization - Single Phase Samples & Electrical Characterization

A systematic variable PLD optimization was conducted for PZT 52/48 to eliminate unwanted secondary phases and improve dielectric properties. Nova Pt-coated Silicon substrates were utilized during the initial optimization steps. The baseline parameters for film optimization were based on the thesis work of Dan Marincel.[4] The initial deposition conditions from this work are provided in Table 4.1

Table 4-1: Initial pulsed laser deposition conditions for PZT films on platinum-coated silicon substrates

Composition	Chamber Pressure **[mTorr]**	Substrate Temperature **[°C]**	Target-Substrate Distance **[cm]**	Laser Energy Density **[J cm^{-2}]**	Repetition Rate **[Hz]**
$Pb(Zr_{0.52}, Ti_{0.48})O_3$	100	630	6	1.2	10

The first variable investigated in the optimization process was chamber pressure. The pressure of the system affects thickness uniformity, growth rate, and lead loss which can drive formation of secondary pyrochlore phases. It was found that as the pressure increased, the plasma plume narrowed, which increased the instantaneous growth rate per pulse. The chamber pressure further changed the mean free path in the vapor phase, and thereby affect the number of collisions prior to reaching the substrate surface.[48] Increased pressure thus decreases bombardment energy of the growing film and consequently decreases lead loss.[48] A series of PZT films were grown at varying chamber pressures between 100 and 400 mTorr.

Phase purity of the films from the pressure series was assessed by XRD scans, as shown in Fig. 4-1. The XRD data were analyzed for secondary pyrochlore phases that can arise from a lead excess or lead deficiency. Figure 4-1 represents an overlay of each pressure trial XRD scan on a logarithmic intensity scale in which the intensity values are offset for visual clarity. Secondary phases are marked in the XRD scans by a black (*). It was found that PZT grown at 300 mTorr chamber pressure resulted in single phase PZT films. As such 300 mTorr was selected as the baseline pressure condition for subsequent variable trials.

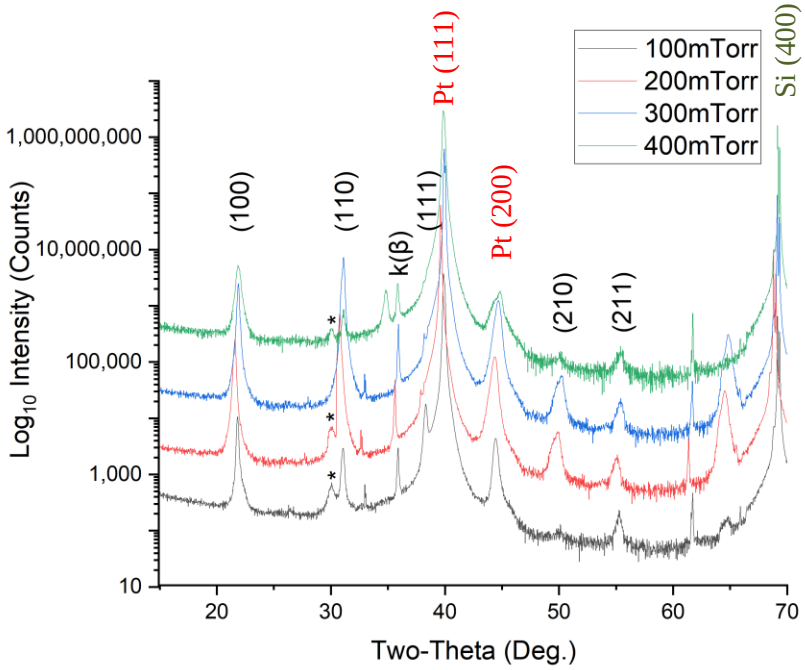

Figure 4-1: PZT films grown at different pressures, with peaks offset for visual clarity. Pyrochlore phases represented are by (*). These films were 500 nm thick.

Another crucial variable tested that affects both the growth rate and grain structure in PLD was laser pulse rate. $Pb(Zr_{0.52},Ti_{0.48})O_3$ was deposited on Pt-coated silicon with a varying pulse rate, holding constant the laser energy density, chamber pressure, surface

temperature, target distance, cooling rate, and number of pulses fired. A consistent laser energy density of 1.2 J/cm^2 was utilized for the various pulse rate trials.

Laser repetition rate can greatly impact a sample's surface structure and crystallinity. Low pulse repetition rates allow more time for atoms to rearrange at the surface, which can improve crystallinity. When pulse frequency is too high, crystallinity can be degraded given that the growing film doesn't have time for atoms to rearrange into optimal positions before being trapped under the next layer of deposited film. Growth rate is crucial to determining the final roughness and surface structure. Moreover, for Pb-based perovskites, low laser frequencies also allow more time for PbO_x to volatilize from the growing films, and as a result the long times can induce lead deficiency which can drive the formation of secondary phases.

Figure 4-2 shows SEM images of samples grown at laser frequencies from 4 to 16 Hz. All images were taken with an InLens detector at an accelerating voltage of 5 kV and a magnification of 25,000 times. A consistent grain structure with minimal boulder density is apparent at a laser frequency of 12 Hz. All of these films were ~ 500 nm thick. With the more consistent grain structure, less zero solutions are expected in the EBSD mapping.

Given the laser pulse rate can impact lead volatility, it is also important to assess the phase purity via XRD. The XRD analysis shown in Figure 4-3 confirms that PZT films grown at 12 Hz possess comparatively small amounts of pyrochlore. 12 Hz was therefore selected as the optimized pulse rate and used in subsequent trials based on these two factors.

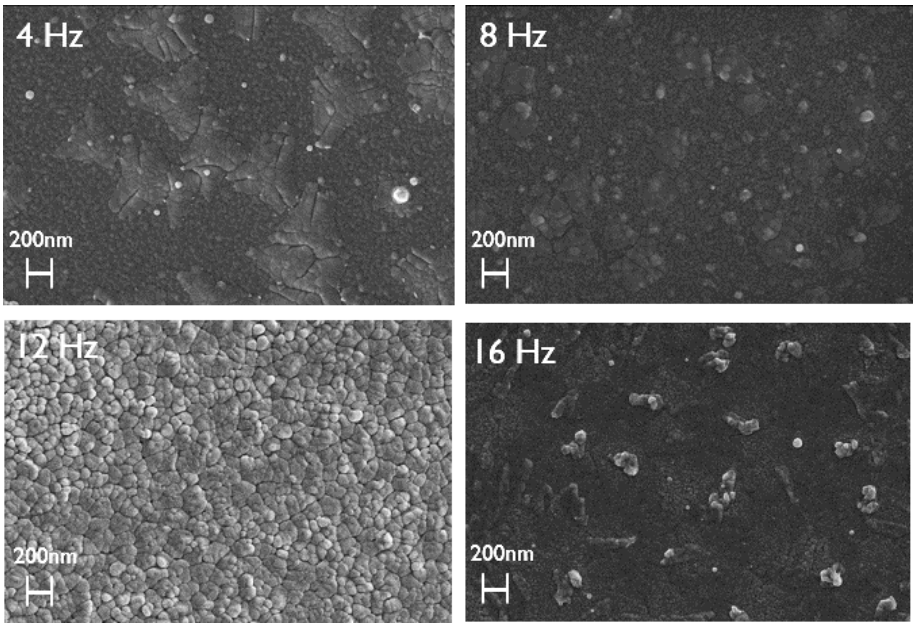

Figure 4-2: Scanning electron microscope images of PZT thin film grain structure for variable study on laser repetition rate using an InLens detector at 5 kV and a magnification of 25,000 times

The target to substrate distance impacts the plume-surface interaction and thus influences thickness uniformity across a sample surface. The sample thickness must be known to quantify the electric field for dielectric permittivity measurements. It was found that a target to substrate distance of 6 cm produced high quality films, consistent plume alignment in practice, and relatively low thickness nonuniformity. The selected substrate distance also corresponds to the PLD conditions utilized by Dan Marincel.[4] The final optimized PZT deposition conditions included a chamber pressure of 300 mTorr, a set substrate temperature of 660°C, a target-substrate distance of 6 cm, and a laser energy density of 1.2 J/cm^2 at a repetition rate of 12 Hz. Utilizing these PLD conditions on platinum-coated silicon substrates produced PZT films with a well-developed polarization

– electric field (P-E) hysteresis, relative permittivity (>1000), remanent polarization (>20 μC/cm^2), and a low loss tangent (< 5%).

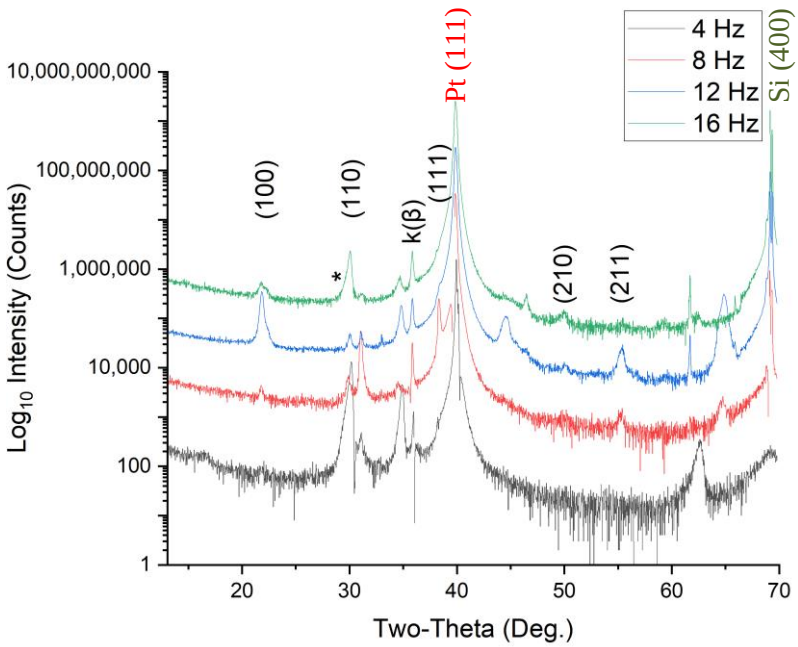

Figure 4-3: Growth of PZT films at different laser pulse repetition rates, with peaks offset for visual clarity. Pyrochlore phases are represented by (*). Standardized to 500 nm thick film growths (the number of pulses was constant)

Figure 4-4 shows a P-E loop for a 450 nm thick PZT 52/48 film on Pt-coated silicon deposited using PLD and measured with a 600 μm diameter electrode and 400 kV/cm drive field. The hysteresis shape demonstrates strong ferroelectric switching and low electrical leakage under the optimized deposition conditions.

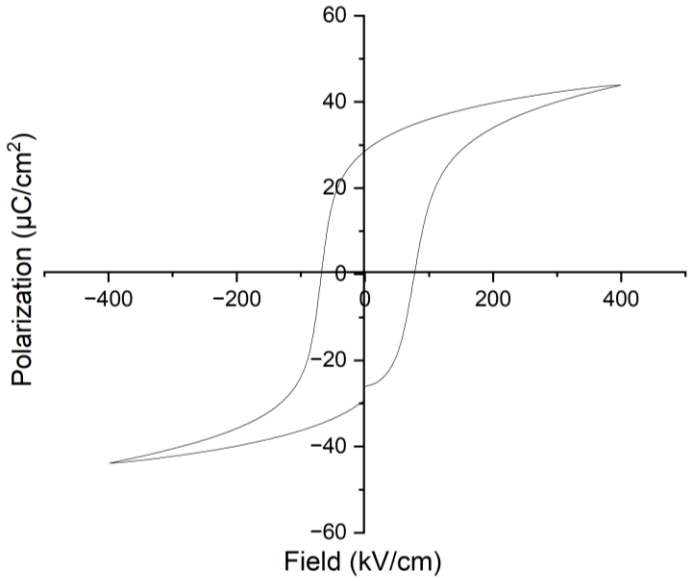

Figure 4-4: Polarization – electric field hysteresis loop for a 450 nm thick PZT 52/48 film sample deposited on Pt-coated silicon using the deposition conditions in Table 4-1, and 600 μm diameter electrode and 400kV/cm drive field

The average surface roughness for the collected area was 31.4 nm with a maximum roughness of 283 nm. An AFM scan of a ~500 nm thick PLD PZT film grown on polished $SrTiO_3$ using the optimized PLD process parameters can be found in Fig. 4-5. It was found that this level of roughness complicated the detection of Kikuchi patterns by EBSD (see section 4.3). The issue of roughness and misoriented Kikuchi patterns was further exacerbated on increasing thickness of PLD PZT. Without the ability to detect and map the Kikuchi patterns to grains, collecting proof of local epitaxy based on regions of uniform orientation was not possible.

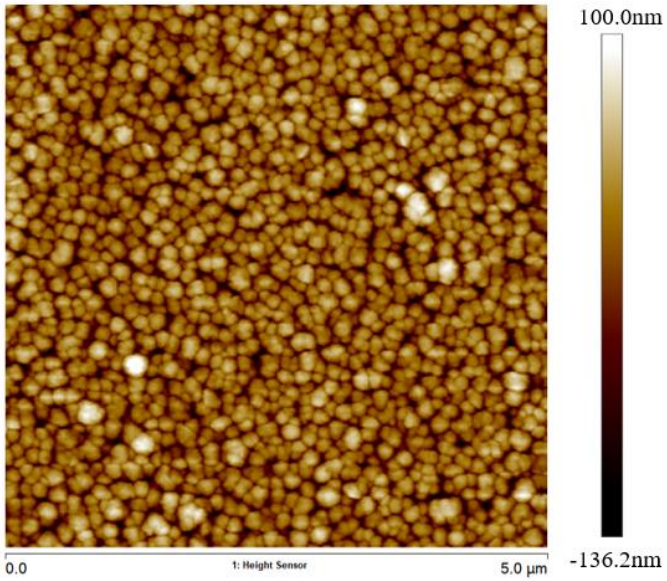

Figure 4-5: AFM scan of ~500 nm PZT deposited on polished $SrTiO_3$ utilizing the optimized PLD processing window

4.3 Deposition with Local Epitaxy to Polycrystalline Substrate

The next optimization step was directed towards transferring the PZT deposition process to polycrystalline $SrTiO_3$ substrates. Achieving local epitaxy to the underlying polished polycrystalline $SrTiO_3$ was critical for local PFM analysis to be mapped to specific locations and to uncover the pinning strength of various grain boundaries and structure features. Primary emphasis for this PLD optimization was demonstrating local epitaxy for the $SrRuO_3$ bottom electrode layer to the polycrystalline $SrTiO_3$. The $SrRuO_3$ deposition conditions utilized the work of Maria et al. as a starting point.[49]

Two factors complicated PZT optimization on polycrystalline $SrTiO_3$: surface roughness and surface temperature uncertainty. EBSD assesses crystallographic

orientation by striking a crystalline material with an SEM beam and then mapping the back scatter pattern; however, a rough surface precludes observation of distinct Kikuchi bands.

The second factor that is problematic with PLD is uncertainty in the growth surface temperature associated with mounting thin $SrTiO_3$ substrates. Unlike silicon wafers which could be removed from the heater stage with a razor blade, the fragile $SrTiO_3$ ceramics were nearly impossible to remove from the substrate heater without breaking into pieces. In response to this problem, the $SrTiO_3$ was sub-mounted to a platinum coated silicon for ease of removal. However, this comes at the cost of an additional thermal resistor between the heater stage and the substrate. As was shown in section 3.5, there is a 30-45°C difference between the heater set temperature and the surface temperature of the $SrTiO_3$ ceramic on Si mounted on the heater. While the temperature difference was compensated for by increasing the set temperature, the true impact on film growth and nucleation at deposition conditions is difficult to assess in a closed system without a thermal imaging system.

The initial PLD deposition conditions of strontium ruthenate described by Maria et al. utilized a laser energy density of 2 J/cm^2 at 10 Hz, a substrate distance of 8 cm, a deposition pressure of 20-160 mTorr, and a top surface temperature of 680°C.[49] To compensate for the 30°C temperature offset, the heater was set to 710°C; the chamber pressure of 160 mTorr was held constant. A lower laser energy density of 1.4 J/cm^2 was also utilized as it produced a shallower ablation racetrack, and so reduced the material that had to be polished away after each run. Under these conditions a growth rate of roughly 10 nm/min was recorded for $SrRuO_3$; the resultant films were smooth enough to be mapped by EBSD.

The $SrRuO_3$ bottom electrode layer (prior to PZT deposition) demonstrates clear orientation mapping at layers beyond the thickness limitations present in PZT. This is demonstrated in the orientation imaging map in Figure 4-6 for 100 nm $SrRuO_3$ on polished $SrTiO_3$. It is apparent that the map shows large areas of similar orientation, with a grain structure that mimics that of the underlying $SrTiO_3$. This establishes that PLD deposition

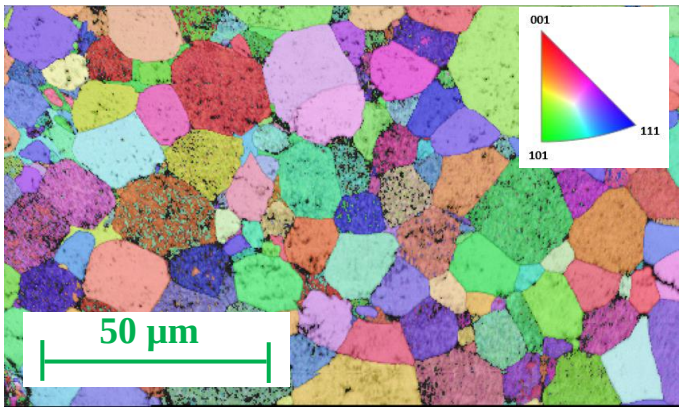

Figure 4-6: EBSD scan of 100 nm thick $SrRuO_3$ grown on polished $SrTiO_3$

of the $SrRuO_3$ bottom electrode, unlike PLD deposited PZT, can be grown with local epitaxy to the underlying substrate at necessary film thicknesses. As such PLD was used to deposit $SrRuO_3$ for both CSD and PLD PZT depositions. CSD deposited PZT demonstrated more consistent local epitaxy to the $SrRuO_3$ layer than the PLD deposited PZT, as will be discussed in section 4.4.

Local epitaxy was retained up to 500 nm of $SrRuO_3$ thickness, as shown in Figure 4-8. While the amount of zero solution increased with the increased thickness, as compared to that of Figure 4-7, Kikuchi patterns are still achievable. The typical bottom electrode thickness was thus chosen as ~100 nm $SrRuO_3$.

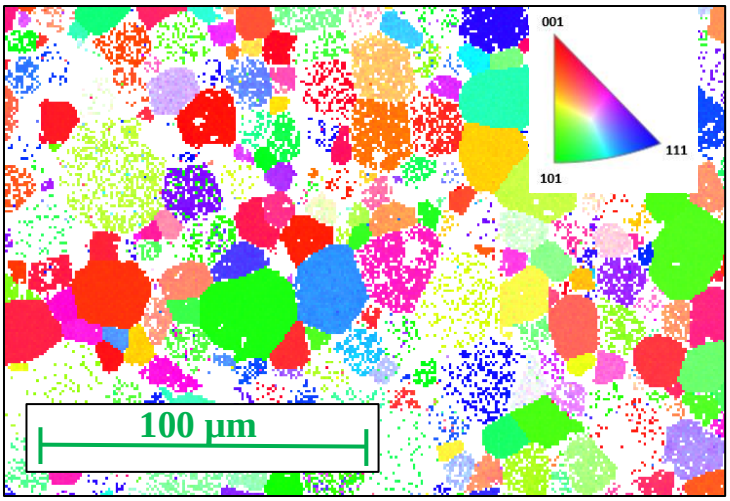

Figure 4-7: EBSD scan of 500 nm thick $SrRuO_3$ grown on polished $SrTiO_3$

Finally shown in Figure 4-8 shows an EBSD map of ~1000 nm of CSD deposited PZT on ~100 nm of PLD deposited $SrRuO_3$ on polished $SrTiO_3$. This film stack matches the thicknesses used for the final PFM analysis, and demonstrates that clear grain orientations and grain boundary that represent the polycrystalline nature of the $SrTiO_3$ locations could be characterized via EBSD.

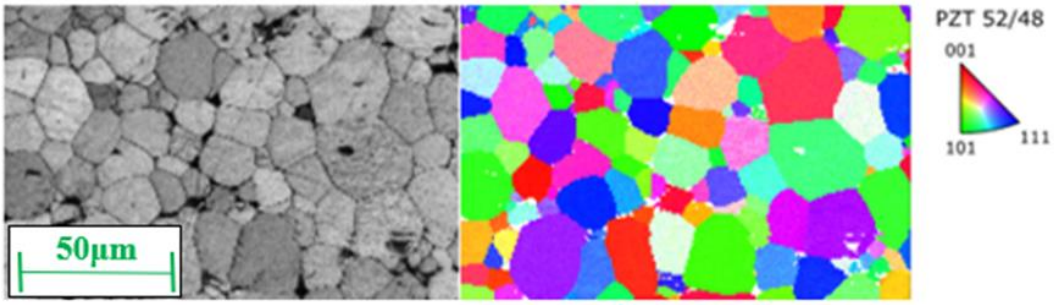

Figure 4-8: EBSD map on $SrTiO_3$, $SrRuO_3$, PZT film stack demonstrating local epitaxy of the PZT and mapping the grain orientations such that specific orientation angles can be assessed

4.4 Deposition Technique Comparison

The other technique employed to deposit $Pb(Zr_{0.52},Ti_{0.48})O_3$ was chemical solution deposition (CSD). The CSD processing procedure was a modification of the processes reported by Trent Borman and Wanlin Zhu as described in section 3.6.[55,56] In this section, PZT films using both deposition techniques will be compared.

Figure 4-9 demonstrates the polarization-electric field hysteresis loops (P-E Loop) for both a 1000 nm CSD deposited PZT and 1000 nm PLD deposited PZT samples on Nova Pt-coated silicon substrates, both measurements utilized a 200 µm platinum top electrode and a drive field of 400 kV/cm. In both cases, the films exhibited a relative permittivity >1000, remanent polarizations >20 $\mu C/cm^2$, and loss tangents < 5%. The cross sections of sample

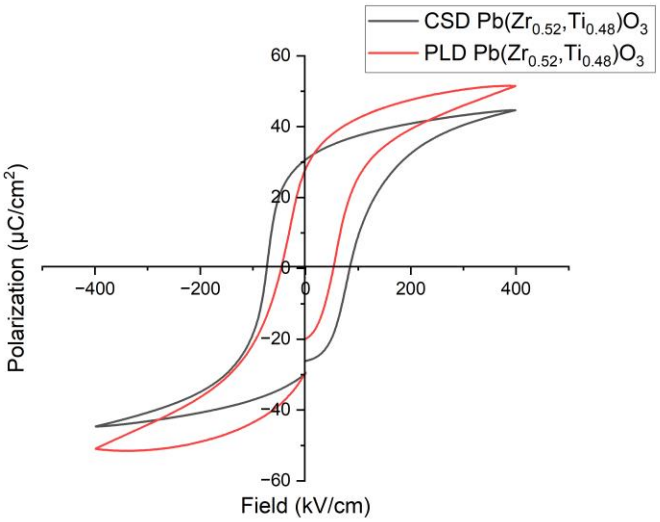

Figure 4-9: Polarization – Electric Field Hysteresis loop for a 1000 nm thick PZT 52/48 film sample deposited on 100nm $SrRuO_3$ on polished $SrTiO_3$ with 600 µm diameter platinum electrode and 400 kV/cm drive field

stacks from both deposition techniques are displayed in Figure 4-10 which demonstrate the comparatively smooth sample surface of the CSD film (A) yielded improved EBSD

measurements relative to PLD films (B). Surface SEM images are also shown for the same sample stacks in Figure 4-11. It is clear that the CSD film has decreased roughness and

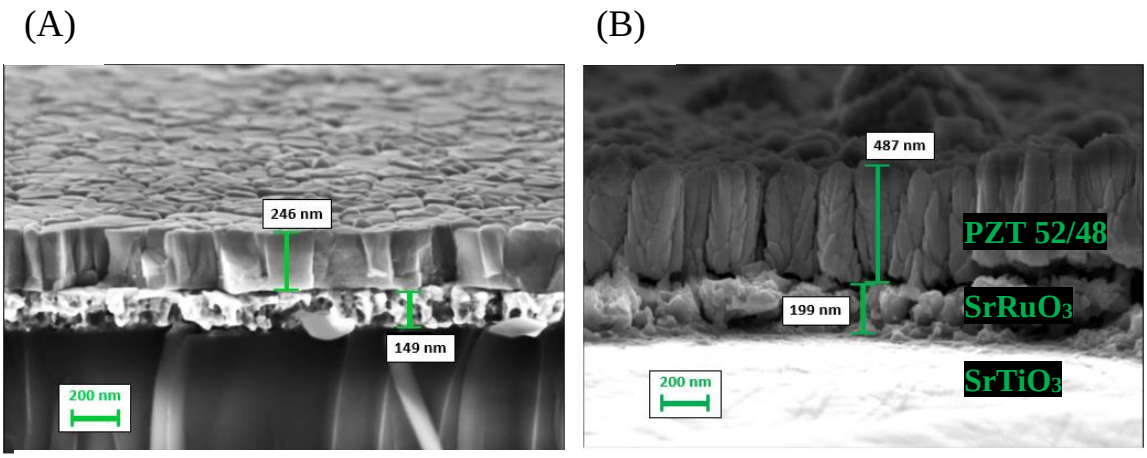

Figure 4-10: Cross-section SEM comparison of $SrTiO_3$, $SrRuO_3$, PZT thin film stack with PZT deposited via CSD (A) and PLD (B) demonstrating the surface roughness

less surface particles compared to PLD deposited PZT. Moreover, there is little surface pyrochlore.

Films of increasing thicknesses from each deposition technique were characterized for microstructure and orientation mapping. It was found that the rough PLD deposited

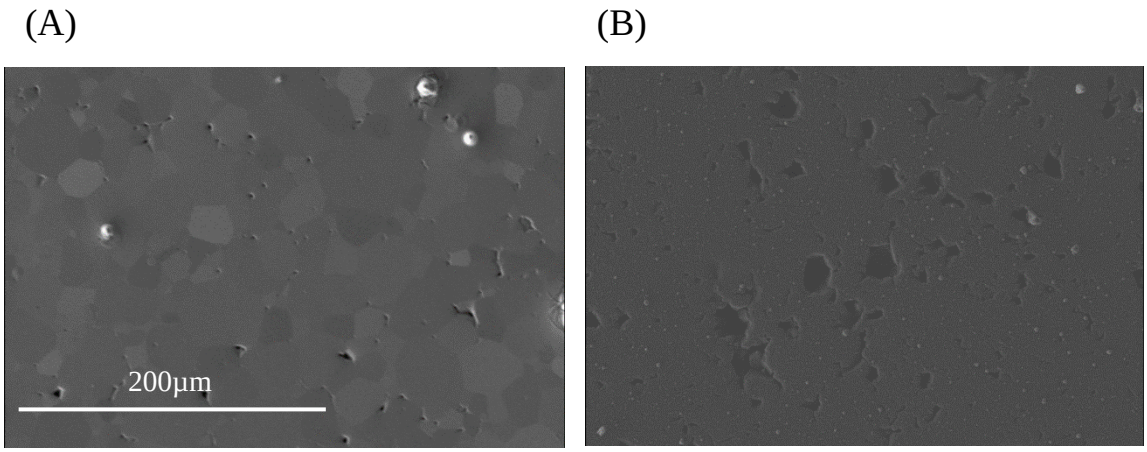

Figure 4-11: Surface SEM comparison of $SrTiO_3$, $SrRuO_3$, PZT thin film stack demonstrating sample surface roughness at 500x magnification for CSD deposited PZT (A) and PLD deposited PZT (B)

films either failed to show regions of uniform crystallographic orientation or produced uninterpretable Kikuchi patterns for EBSD. Notably the PLD PZT films exhibited degraded orientation imaging results as the thickness of the film increased beyond 250 nm.

Figure 4-12 shows that PZT deposited through PLD can demonstrate Kikuchi patterns at a film thickness of 250 nm. There are many regions shown in black on the scan that demonstrate "zero-solution" or no discernable Kikuchi patterns within that area. However, even in regions where Kikuchi patterns could be collected, there is poor correlation between the orientation map and the large underlying $SrTiO_3$ grains. Compared to the EBSD map of Figure 4-8 in section 4.3 for a 1000 nm thick PZT film, it is clear that

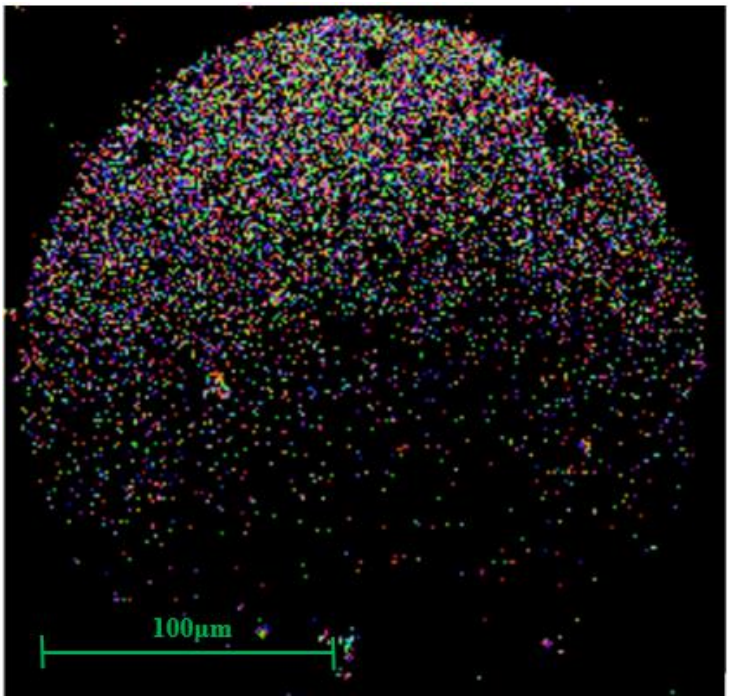

Figure 4-12: EBSD scan of a 250 nm of PZT deposited via PLD on $SrRuO_3/SrTiO_3$ exhibiting large amounts of zero solution. Furthermore, the regions of uniform orientation are far smaller than the $SrTiO_3$ grain size, suggesting that these growth conditions do not favor a local epitaxial relationship in which the PZT orientation is controlled by the underlying $SrTiO_3$.

the uniformity in orientation within the scale of a $SrTiO_3$ grain size was inferior in PLD samples to that of CSD deposited samples.

Finally, two sample stacks of ~1000 nm $Pb(Zr_{0.52},Ti_{0.48})O_3$ were grown using the finalized parameters of each deposition technique, on 100 nm of PLD deposited $SrRuO_3$, on polished $SrTiO_3$. As seen in Figure 4-13, both techniques yielded comparable XRD scans, with slightly higher intensities in the case of the CSD deposited film. In both cases, the lack of secondary phases attests to the optimized deposition parameters, and demonstrates that the need for chemical solution deposition is primarily on the basis of distinct Kikuchi patterns and improved EBSD mapping.

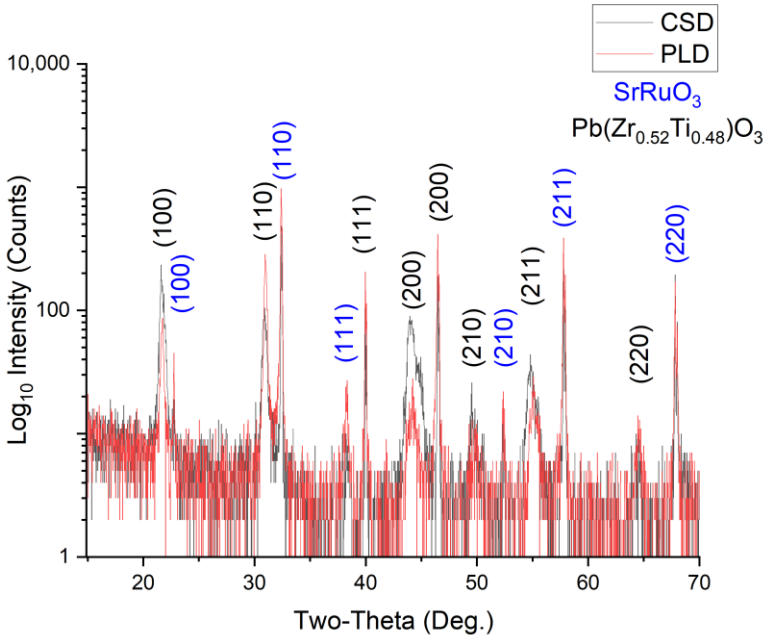

Figure 4-13: XRD patterns for unpatterned 1000 nm PZT/100 nm $SrRuO_3$/polished $SrTiO_3$ film stacks prepared by CSD and PLD

4.5 Registry of EBSD and Piezoresponse Force Microscopy Data

Once consistent Kikuchi patterns could be collected on the deposited PZT films, an added difficulty of returning to the same location as the orientation imaging map had to be addressed. Shown in Figure 4-14 is an EBSD-overlayed SEM image of a PZT/

$SrRuO_3/SrTiO_3$ sample stack prior to depositing the platinum top electrodes. Using these overlays, the location of grain boundaries can be approximated based on visible grains in

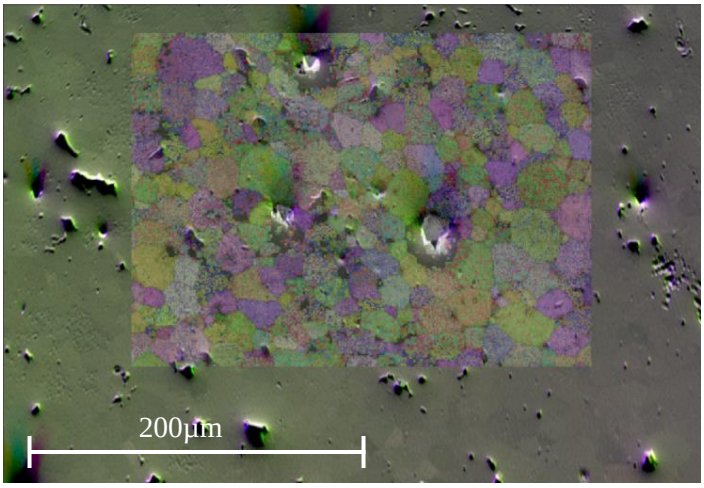

Figure 4-14: Collected EBSD map overlayed onto SEM image of an unpatterned PZT/ $SrRuO_3/SrTiO_3$ film stack

the SEM image and the EBSD zero solution regions that accompany surface defects. However, alignment to the EBSD maps based solely on structural landmarks does not offer sufficient accuracy to make reports on individual grain boundaries once the top electrode is deposited. Furthermore, samples cannot be reassessed via EBSD once the top electrode is deposited. For example, Figure 4-15 shows an orientation map where the platinum electrode areas obscure the underlying grain orientation, and thus offers no information on grain boundary or triple point locations. To combat this, the circular electrode areas were mapped prior to depositing the platinum top electrode as described in section 3.12. To aid in map alignment, crosshairs markers were patterned at 90° intervals around the electrodes so that the collected scans could be tilt-corrected for alignment of the PFM data so that areas of interest could be scanned under the photolithography steps described in section 3.10.

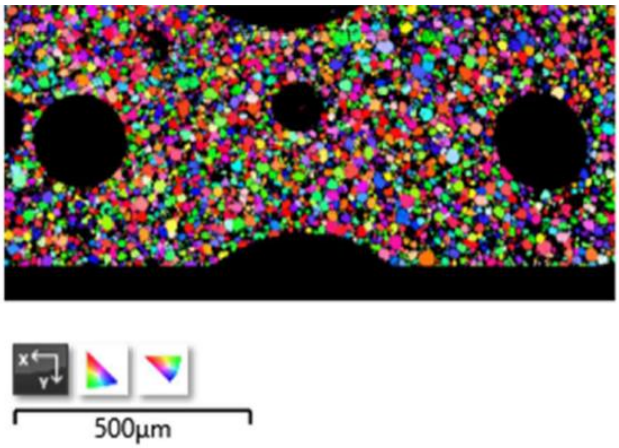

Figure 4-15: Collected EBSD map demonstrating the zero solutions associated with platinum top electrodes (dark circles).

Shown in Figure 4-16 (A) is an SEM image of a 200µm diameter electrode and its tilt correction crosshairs, alongside the EBSD orientation map of the same electrode region (B). Once aligned to the orientation map, the PFM probe was rastered along a square area centered about a triple point of interest for assessment of the poling uniformity. The sample was pre-poled at three times the coercive field prior to each measurement, and care was

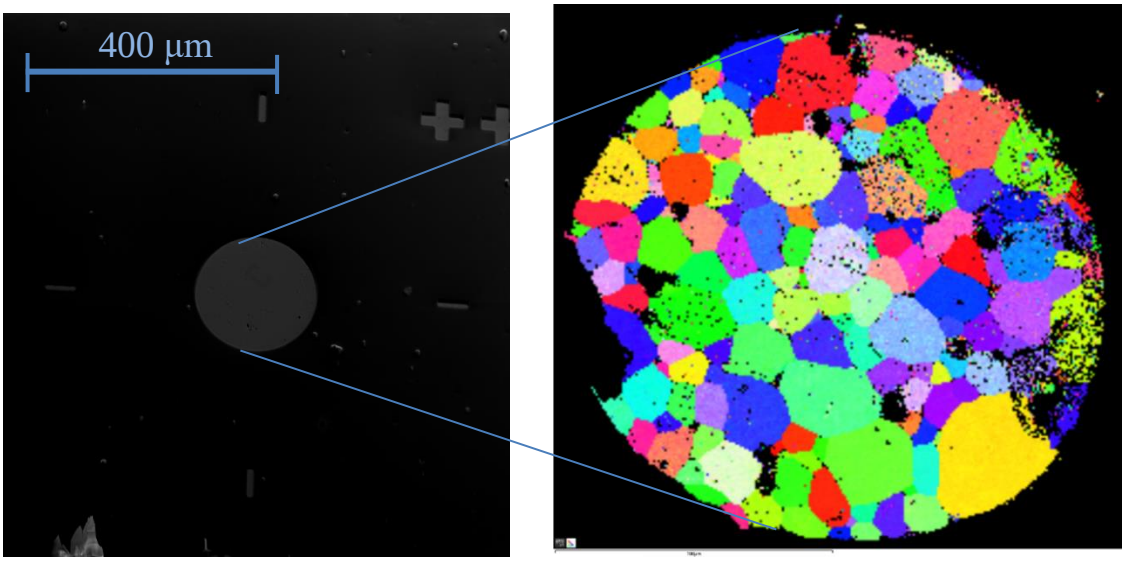

Figure 4-16: (left) SEM image of patterned electrode area and alignment crosshairs with exposed PZT layer (right) EBSD map of the same electrode area rotated with respect to PFM crosshair orientation.

taken to ensure that the piezoelectric phase was uniform across the scan area. Using the EBSD map the precise grain boundary location could then be located. It was found that the piezoresponse amplitudes differ for each grain, as expected, due to their different orientations. Moreover, the piezoelectric response of a single grain was found to vary in steady state value with respect to different grain boundaries. Presumably the differing behavior is in response to changes in the electrical and mechanical boundary conditions associated with proximity to grains of different orientations.

Figure 4-17 demonstrates the use of an EBSD map with two different sized PFM scan areas (shown as white boxes) to first locate the sample area with respect to the electrode map, and then narrow the scan area to a triple point region of interest. As regions of interest were identified on the piezoresponse scans, maps of the local nonlinear response were acquired by Travis Peters at the Center for Nanoscale Materials Science at Oak Ridge National Laboratory on a Cypher AFM (Asylum Research). To do so, deflection amplitude

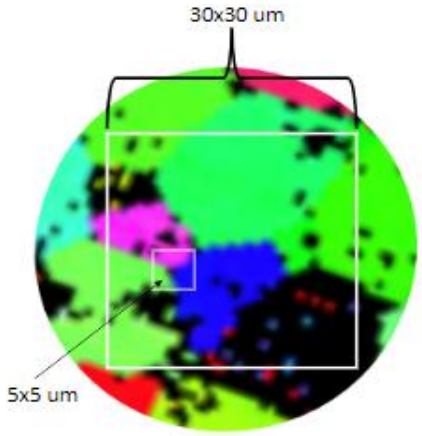

Figure 4-17: A large scan region was used for initial PFM analysis (large white box) was overlaid on the collected EBSD orientation map to locate a triple point region for study (small white box)

data were collected as a function of the driving voltage. As described by Griggio et al., the band excitation signal with which the sample was driven was optimized to reduce the effect

of nonlinearities in the tip-sample contact on the measured data.[37] The displacement data was then fit point-by-point to a simple harmonic oscillator. The excitation signal was converted from voltage to field and the displacement data were fit to: Displacement = A2E + A3E^2.

Shown in Figure 4-18 is the result of a grain boundary trace of the same triple point as Figure 4-17 rescaled to the 5 µm x 5 µm scan area and then used to format the raw data with respect to grain boundary position. The $\alpha/d_{33,init}$ ratios were typically found to be smaller near the grain boundary and triple point locations. The nonlinearity results surrounding the triple point are discussed in detail in section 4.6.

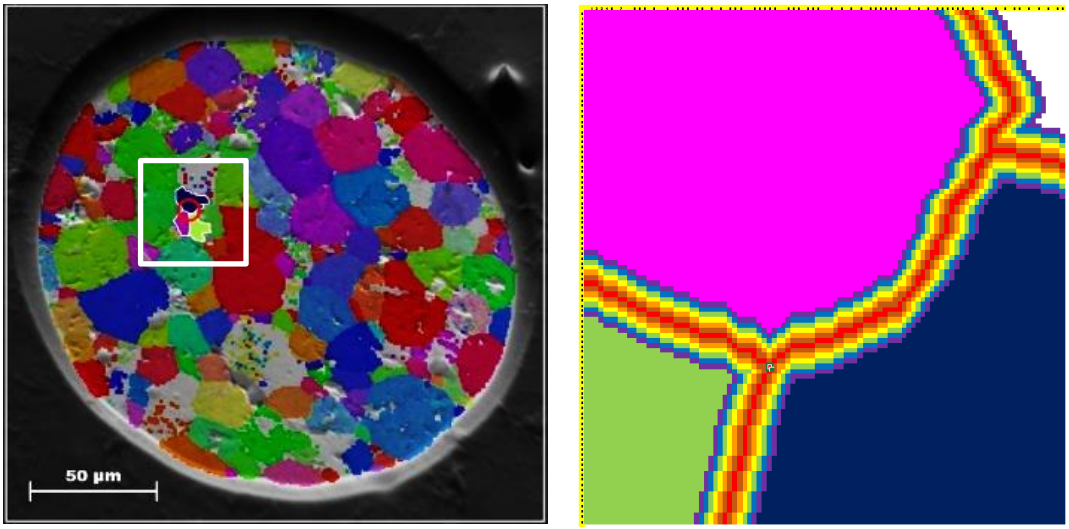

Figure 4-18: (Left) EBSD map of an electrode used to identify the grain boundary locations. The triple of interest is highlighted by the white box (Right) Marked .CSV file with a grain boundary trace to associate raw data with microstructure locations. The red line denotes the grain boundaries in the 5 µm x µm scan

4.6 Piezoresponse Force Microscopy Measurements of Microstructure and Local Nonlinearity

The approach outlined above was used to measure the piezoresponse behavior about multiple grain boundaries and triple points and address how the nearby domain wall motion is affected. Using Piezoresponse Force Microscopy (PFM), local behavior was measured in a 50 nm x 50 nm pixel grid over a scan area of typically 5 μm x 5 μm. EBSD orientation maps that identify and mark the relative position of structure features were then overlaid onto these PFM scan regions such that the positions of triple points and grain boundaries could be correlated to their $\alpha/d_{33,init}$ responses reported by the PFM .CSV files. The cell sizes within the file were scaled to the square pixels of the PFM scan to avoid distorting the aspect ratio when comparing to the map. This section catalogs the types of behaviors that were observed. The investigated triple points are on a 1000 nm thick $Pb(Zr_{0.52}Ti_{0.48})O_3$ thin film deposited via chemical solution deposition on 100 nm of PLD deposited $SrRuO_3$ on polished $SrTiO_3$.

Shown in Figure 4-19 is an example of a triple point marked in the .CSV file on the left, in which the dark red line, a single pixel in width, denotes the grain boundary location, and the adjacent lines to either side of the boundary denote the response at 50 nm intervals away. Figure 4-19 also shows the associated PFM $\alpha/d_{33,init}$ map from which the .CSV

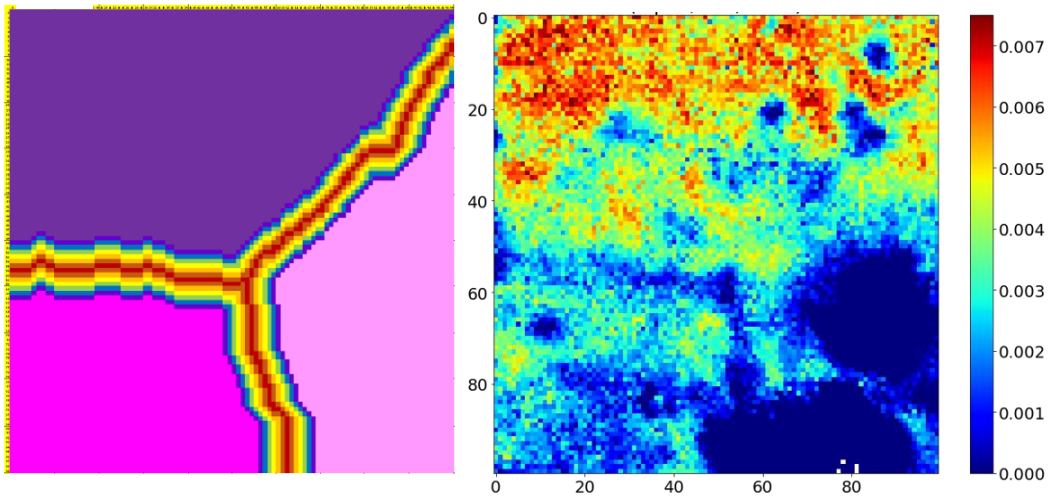

Figure 4-19: (Left) Marked .CSV file to associate raw data with microstructure locations. Red line denotes the grain boundary locations across a 5 μm x μm scan (Right) PFM $\alpha/d_{33,init}$ map from corresponding to the .CSV file collected on a 1000 nm $Pb(Zr_{0.52}Ti_{0.48})O_3$ thin film on 100 nm of $SrRuO_3$ on polished $SrTiO_3$

values were collected. The ratio of the Quadratic A3 component over the Quadratic A2 component was multiplied by 2 to report $\alpha/d_{33,init}$.

It should be noted that in calculating the average responses at discrete intervals away from each boundary, the points associated with large topographical changes were eliminated. In Figure 4-19 (Right), the dark blue areas in the bottom right of the PFM map are correlated with ~300 nm high surface defects found in the topography maps of the same PFM scan region. It is well known that there is some topographic crosstalk in the PFM signal. Here, where nonlinearity is mapped, it was found that the surface features artificially lowered alpha/$d_{33,init}$ in that region. Thus, these data points were eliminated from subsequent data processing.

By assessing the average ratio of irreversible and reversible piezoelectric response, conclusions can be drawn about the length scale and magnitude of nonlinearity about various pinning features. An $\alpha/d_{33,init}$ vs. position graph was created for each grain boundary

with the grain boundary represented by position 0, and the responses along lines parallel to the grain boundary averaged into both grains. This method enabled visualization of where the grain boundary pinning influenced the $\alpha/d_{33,init}$ ratio. In the following section, individual grains were color-coded, and are referred to by that color code.

The grain boundary between the purple and fuchsia grains was analyzed using this method to produce a graph of average $\alpha/d_{33,init}$ response with respect to distance from the grain boundary, as shown in Figure 4-20. The boundary has a misorientation angle of 60.9° and corresponds to a Σ17b coincident site lattice (CSL) boundary associated with a rotation around {221} of a crystal with m3m point group symmetry. Using this methodology each data point represents the collected average in 50 nm increments from the grain boundary (represented as the dotted line at pixel position 0). The Euler angles and closest relative

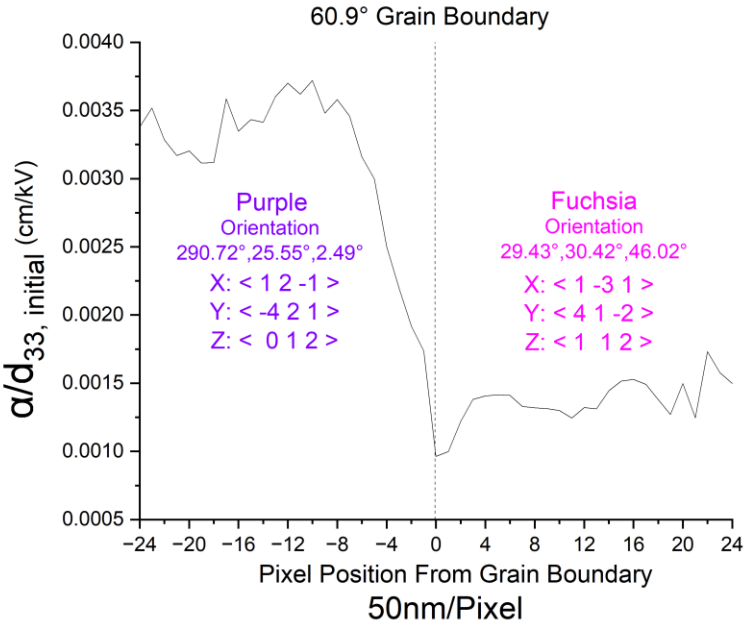

Figure 4-20: Average ratio of $\alpha/d_{33,init}$ with respect to proximity to the 60.9° grain boundary denoted as the center dotted line. The Euler angles and approximate orientations of each grain are shown with respect to the laboratory coordinates.

directions for each axis are shown on each grain's respective side of the boundary. A clear drop in the magnitude of $\alpha/d_{33,init}$ is seen in Figure 4-20 as the grain boundary is approached from either side, which suggests a strong local pinning site that impacts nonlinearity. However, it is notable that both the magnitude of the irreversible contributions to the piezoelectric response, and the width of influence of the grain boundary on domain wall motion differ on either side of the boundary. This is in contrast to the more symmetric grain boundaries studied by Marincel.[4] The fuschia grain has an $\alpha/d_{33,init}$ that goes through a shallow maximum of ≈0.0014 cm/kV around ≈200 nm from the pinning site followed by steady state behavior. For the purple grain, $\alpha/d_{33,init}$ reaches a larger steady state value ≈0.0037 cm/kV at a distance of ≈400 nm away from the boundary.

Utilizing this method, however, limits the accuracy of pinning influence to 50 nm increments from the grain boundary. Thus, methods adopted from the thesis work of Dan Marincel which utilize clustered response behavior were implemented to analyze the pinning distance in finer detail. Clustered responses of strong and weak nonlinear response behavior have been reported previously in Bintachitt and Marincel's thesis work as was explained in Section 2.5.[4,32] The three methods adopted from the work of Dan Marincel for this interpretation are quoted below.[4]

"Method 1: The mean and standard deviation in the nonlinear response for each sample were determined from maps collected far from the grain boundary. Then, low response regions were defined as those as having a value of $\alpha/d_{33,init}$ more than half the standard deviation below the mean nonlinear response. The total area of low response regions near a grain boundary was then divided by the total distance data was collected parallel to the grain boundary (~5 μm). The result is the average width of influence. The

error bars were determined as the 95% confidence in the width of low response at each row.

Method 2: Using all low response clusters on the map of the grain boundary as determined in Method 1, the number of low response pixels observed with distance from the grain boundary was represented in a histogram. If a random distribution of the nonlinear response were observed with no clustering, approximately 33% of the pixels at each distance from the grain boundary should be low response. Due to clustering in the response, the cutoff value was set to 40% of the pixels observed at each distance from the grain boundary being low response. The error bars were determined as ±5% in the ratio of low response pixels. The red horizontal line marks the cutoff determined by 40% low response pixels, while the black vertical line denotes the grain boundary.

Method 3: The average of the nonlinear response parallel to the grain boundary shows a minimum at the grain boundary. A cutoff value of 25% of the standard deviation below the mean nonlinear response was used to determine the width of influence. the center red horizontal line shows the mean nonlinear response and the surrounding red horizontal lines indicate ±25% of the standard deviation."[4]

In Marincel's work, the mean was collected far from the grain boundary. Given the smaller area of measurement in this work, uniform descriptions of "far" were not available. Thus, the $\alpha/d_{33,init}$ vs. position was plotted, and the average values were assessed as regions where the $\alpha/d_{33,init}$ vs. position appeared to be constant.

Utilizing the clustering methods described, the binned response regions were defined as being above, within, or below the mean nonlinear response ± ½ standard deviation far from the boundary for counting the number of low response pixels in method

1 and method 2. For method 3, the bounds were set based on the mean nonlinear response ± ¼ of a standard deviation far from the boundary. Given the different orientations of the grains, a separate mean and standard deviation were collected on both sides of each grain boundary. The $\alpha/d_{33,init}$ values of the .csv file were then conditionally formatted to appear as grey when within the mean ± ½ standard deviation, and black when above the high response cutoff. This leaves only the low response values for that grain unformatted. Most low response pixels were observed at the grain boundary, with several small low response behavior clusters shown elsewhere.

Following formatting of the nonlinear response maps, the number of unformatted low response pixels was counted. The number of low response pixels was then used in one of two ways: for method 1, the number of low response pixels in a line perpendicular to the grain boundary was used to assess the average length scale of low response clusters by collecting the total area of clustered low response divided by the length of the grain boundary to obtain an average width of low response. Unfortunately, in this work, it was difficult to properly calculate pixels that were perpendicular to slanted grain boundaries in the PFM frame of reference. In this case, the counting was done using the rectilinear grid, which introduces error in the calculated width of influence. In these cases, method 3 was believed to provide better values. The method 3 calculations were verified using method 2 for comparison. For method 2, the number of unformatted pixels were counted parallel to the boundary shape at increasing distances and then divided by the total number of pixels in that grain boundary to collect the ratio of low response behavior at that distance from the grain boundary. The intercept of 40% low response was used to determine the steady state behavior as described above. This approach differs in part from the work of Marincel

in that he consistently used 100 pixels per grain boundary for the bicrystal substrates; that could not be done here given the variable nature of the grain boundary lengths for the films on polycrystalline substrates. The point at which the concentration of low response pixels drops below 40% for clustered response grains and 33% for nonclustered response grains was then determined to be the width of influence for grain boundary pinning. For method 3 the average value of the PFM pixels were tabulated parallel to the boundary at increasing distances, from there the intercept of the calculated $\alpha/d_{33,init}$ average far from the boundary was used to determine steady state. The mean nonlinear response ± ¼ standard deviation was used to determine the error bars for method 3. The following discussion describes several triple point regions in the film and catalogs their response.

The first triple point investigated corresponds to the map in Figure 4-21. For the following analysis, the lower left grain will be referred to as fuchsia, the lower right grain as pink, and the top grain as purple. Figure 4-21 (Left) shows the scale and location of the

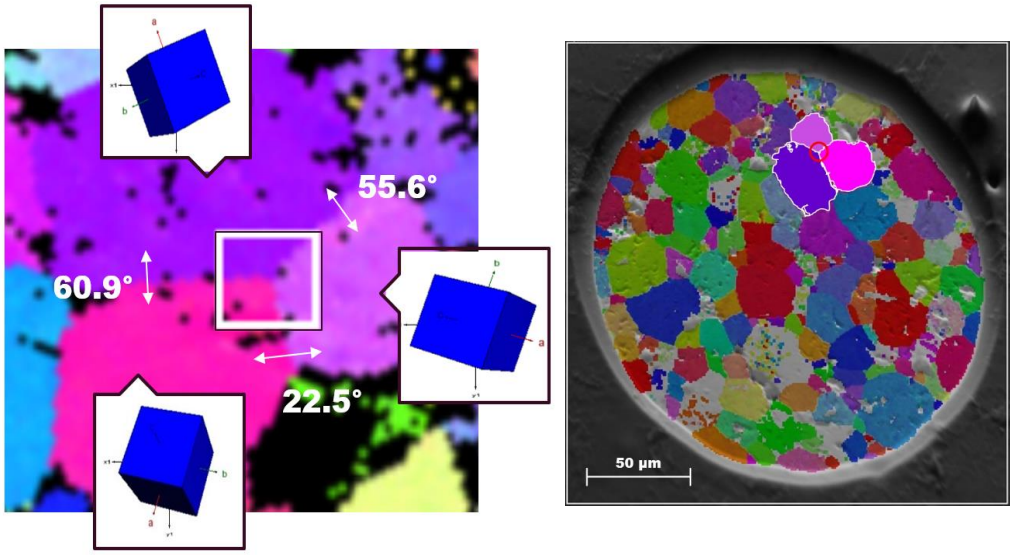

Figure 4-21: (Left) EBSD orientation map of a triple point with grain boundary misorientation marked. The white square denotes the PFM scan area. The blue cubes represent the orientation of each grain (Right) The relative position of the PFM scan region with respect to the 200µm electrode

PFM scan region as the white box at the triple point of these three grains, alongside their relative position on the 200 μm diameter electrode in Figure 4-21 (Right). The visualization of the grain orientation as well as the reported misorientation angles were produced using the AztecCystal grain analysis tool.

Analysis of the data in Fig. 4-22 via Method 3 based on the average response vs. position for the purple-fuchsia 60.9° grain boundary results in a pinning influence the stretches 379 ± 76 nm into the purple grain and 193 ± 295 nm into the fuchsia grain for a total width of influence of 572 ± 371 nm. The fuschia grain has an $\alpha/d_{33,init}$ that goes through a shallow maximum of ≈0.0028 cm/kV while the purple grain, $\alpha/d_{33,init}$ reaches a larger steady state value ≈0.0037 cm/kV. In Figure 4-22, the thicker horizontal red dotted line

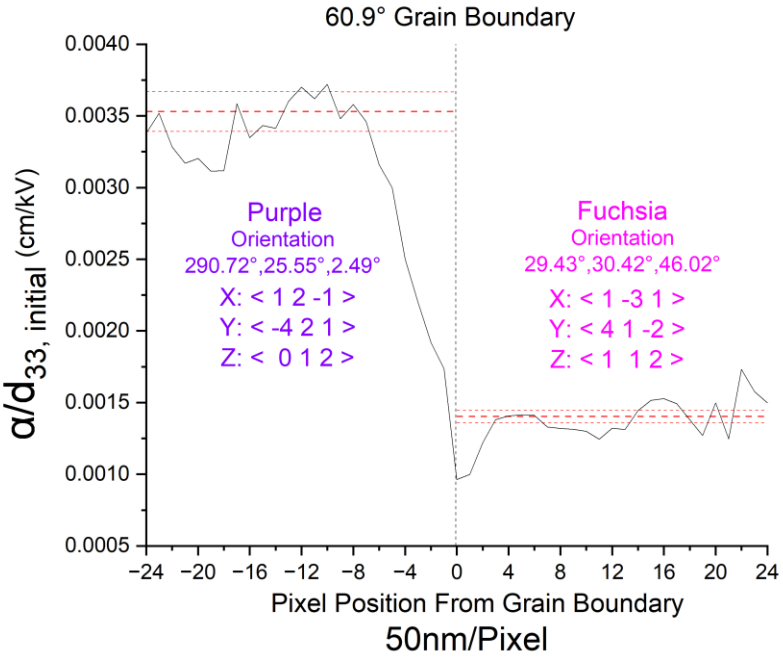

Figure 4-22: Analysis of the on Fuchsia/Purple 60.9° grain boundary by method 3. The grain boundary is marked as a vertical line. The thicker red horizontal line represents an average $\alpha/d_{33,init}$ value far from the grain boundary. The thinner red lines mark ± ¼ a standard deviation from the mean value

represents the average far from the boundary, and the other two red lines represent 25% standard deviation away from that mean; the vertical dotted line marks the Σ17b grain boundary. By eye, the width of influence was estimated as ~ 600 nm, within the error bounds for method 3.

The same dataset analyzed by method 2 yielded a lower width of influence in the purple grain of 317 ± 9 nm for the 40% intercept, as shown in Figure 4-23.This is not unexpected, as the bounds mark where the data fall below the mean $\alpha/d_{33,init}$ value by a half, rather than a quarter of a standard deviation. The fuchsia grain reported a width of influence of 330 ± 21 nm for a total width of influence of 647 ± 40 nm. This total width of influence agrees with method 3 and the by-eye interpretation as it estimates a roughly 600

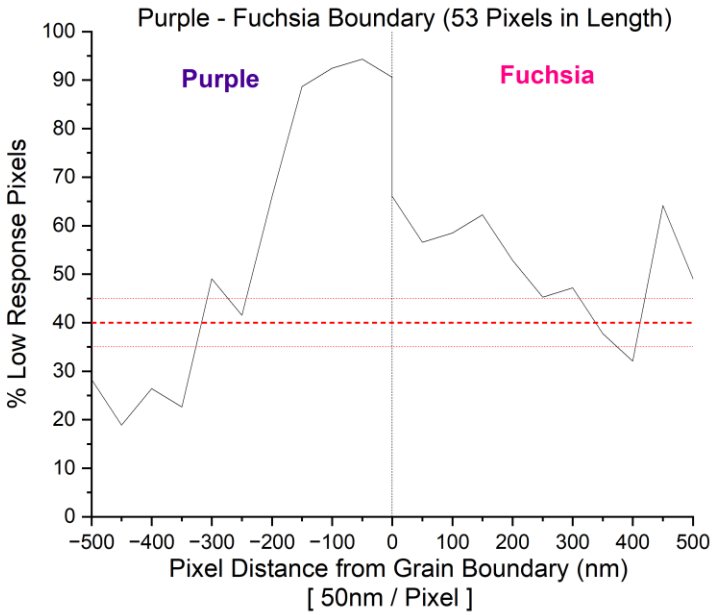

Figure 4-23: Method 2 on Fuchsia/Purple 60.9° grain boundary. The point at which the % of low response pixels crossed 40% (the darker red line) defined the width of influence of the boundary. The grain boundary is marked with a vertical line.

nm width. Table 4-2 shows a comparison of methods 1 – 3 for the purple-fuchsia boundary.

It was found that the standard deviations for method 1 were large, even though the raw data (e.g. Fig. 4-22) shows a clear minimum in $\alpha/d_{33,init}$ associated with the grain boundary. For example using method 1, the width of influence of the grain boundary into the purple grain was determined to be 831 ± 383 nm and 430 ± 254 nm into the fuchsia grain, for a total width of influence of 1261 ± 637 nm. Thus, while each method was utilized for every investigated grain boundary, in the remainder of this chapter the results for method 3 will be discussed.

Table 4-2: Methods 1-3 for purple – pink – fuchsia triple point. The solid horizontal line represents a point the method was unable to determine, and the * represents a coincident site lattice boundary

Misorientation Angle	***60.9°**	**22.5°**	***55.6°**	**Triple Point Analysis**
Grain Boundary Pinning Distance **(Method 1)**	Purple 831 ± 383 nm	Pink 682 ± 572 nm	Pink 421 ± 299 nm	_____
	Fuchsia 430 ± 254 nm	Fuchsia 640 ± 568 nm	Purple 743 ± 527 nm	_____
Total Width of Influence	1261 ± 637 nm	1322 ± 1140 nm	1164 ± 826 nm	1561 ± 1083 nm
Misorientation Angle	***60.9°**	**22.5°**	***55.6°**	**Triple Point Analysis**
Grain Boundary Pinning Distance **(Method 2)**	Purple 317 ± 9 nm	Pink 244 ± 46 nm	Pink 83 ± 13 nm	_____
	Fuchsia 330 ± 31 nm	Fuchsia 225 ± 85 nm	Purple 200 ± 137 nm	_____
Total Width of Influence	647 ± 40 nm	469 ± 131 nm	283 ± 150 nm	313 ± 7 nm
Misorientation Angle	***60.9°**	**22.5°**	***55.6°**	**Triple Point Analysis**
Grain Boundary Pinning Distance **(Method 3)**	Purple 379 ± 76 nm	Pink 188 ± 15 nm	Pink 151 ± 57 nm	_____
	Fuchsia 193± 295 nm	Fuchsia 352± 36 nm	Purple 134 ±11 nm	_____
Total Width of Influence	572± 371 nm	540± 51 nm	285± 68 nm	690 ± 18 nm

For comparison, the 55.6° boundary that separates purple and pink in Figure 4-24 is a Σ3 CSL boundary. The purple grain reaches a steady state value of $\alpha/d_{33,init}$ of 0.0037 cm/kV for both the fuchsia-purple and pink-purple boundaries, though the local minima at position zero of 0.0030 cm/kV in Figure 4-22 is far greater than the minima of 0.0018 cm/kV for the fuchsia-purple boundary in Figure 4-23.

This result suggests stronger local pinning for the Σ17b 60.9° grain based on a greater reduction in $\alpha/d_{33,init}$. The width of influence is also found to be greater for the 60.9° boundary, despite similar steady state behavior far into the grain from both grain boundaries. Utilizing method 3, the 55.6° boundary, approaching purple's steady state 134 ± 11 nm from the grain boundary, compared to the 379 ± 76 nm for the fuchsia-purple

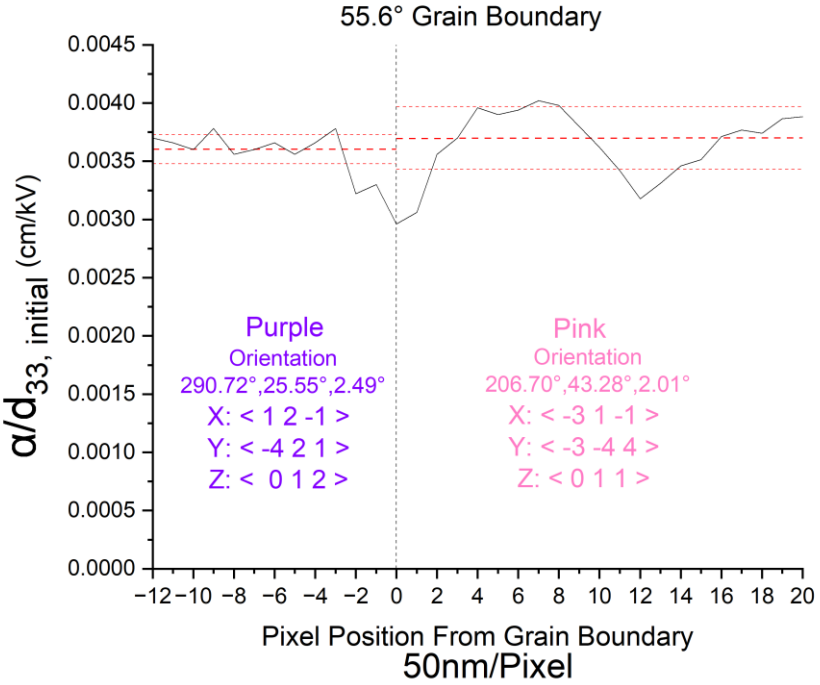

Figure 4-24: Average ratio of $\alpha/d_{33,init}$ with respect to proximity to the 55.6° grain boundary denoted as the center dotted line. The Euler angles and approximate orientations of each grain are shown with respect to the laboratory coordinates.

grain boundary. The width of influence into the pink grain was 151 ± 57 nm, for a total width of influence of 285 ± 68 nm. Using method 2 on the 55.6° boundary resulted in a 283 ± 150 nm total influence. For these two coincident site lattice boundaries, the larger degree of misorientation led to an increased depth of pinning response.

The final boundary of this triple point is the fuchsia-pink boundary. This is a random boundary (not CSL) with a misorientation angle of 22.5°. Several points are apparent in Figure 4-25. First, relatively symmetric behavior can be seen on either side of the boundary up to ~ 150-200 nm from the grain boundary. Beyond this distance, neither the pink nor the fuchsia grain reached the same average $\alpha/d_{33,init}$ as reported in Figures 4-22 and 4-24. While the reason for this is not known, it is speculated that there are differences in the domain structures across the grain, which depend on the matching

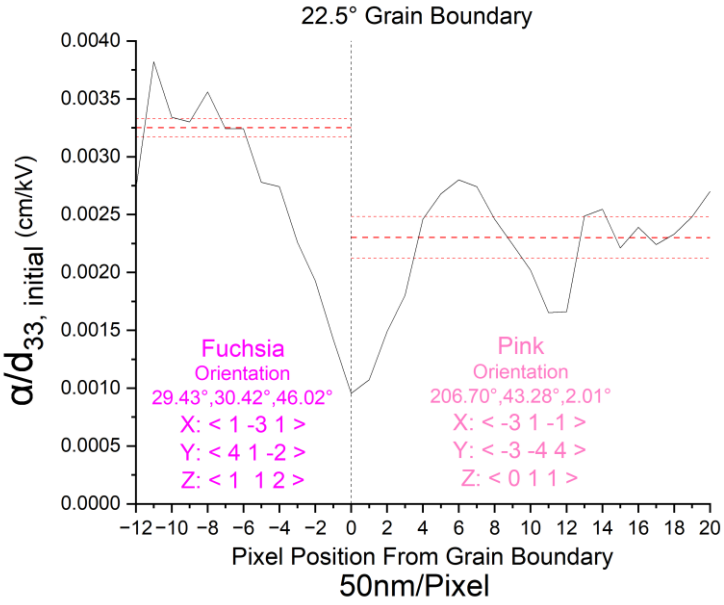

Figure 4-25: Average ratio of $\alpha/d_{33,init}$ with respect to proximity to the 22.5° random grain boundary denoted as the center dotted line. The Euler angles and approximate orientations of each grain are shown with respect to the laboratory coordinates.

conditions across the adjacent grain boundary. The pinning influence was estimated to stretch 352 ± 36 nm into the fuchsia grain and 188 ± 15 nm into the pink grain for a total width of influence of 540 ± 51 nm. It should be noted that of the three grain boundaries intersecting at this triple point, the random grain boundary had the the largest total width of influence on the irreversible motion of domain walls. In sum, the random grain boundary produced both deep minima in $\alpha/d_{33,init}$ and the largest width of influence on domain wall motion.

Another factor which might contribute to differences between the three grain boundaries associated with the triple point in the effective grain size of uniform orientation in the PZT. The areas of each grain are 729 μm^2 for the purple grain, 482 μm^2 for the fuchsia, and 255 μm^2 for the pink one.

Figure 4-19 shows the presence of a significat amount of topographical defects in the pink grain. Although those points have all been eliminated from the averages, there is a chance that the $\alpha/d_{33,init}$ ratios of the surrounding material were affected. Surface variability causing cantilever deflection and a distribution of strong pinning sites may drive the variability in the average $\alpha/d_{33,init}$ maps adjacent to different boundaries, and artificially extend the distance.

The next grain boundary corresponds to the triple point marked as light blue, dark blue, and orange; its relative position on the same electrode area is shown in Figure 4-26 (A); the grain boundary orientations are shown in part (B), the .CSV plotted scan area in (C) and the $\alpha/d_{33,init}$ (D) corresponding to the white square area of Figure 4-26 (B). The respective sizes of each grain are 154 μm^2 for orange, 310 μm^2 for dark blue, and 365 μm^2 for light blue.

For the orange and light blue grain boundary, there is a misorientation angle of 29.8°, which corresponds to a Σ13b CSL boundary with rotation around {111}. As shown

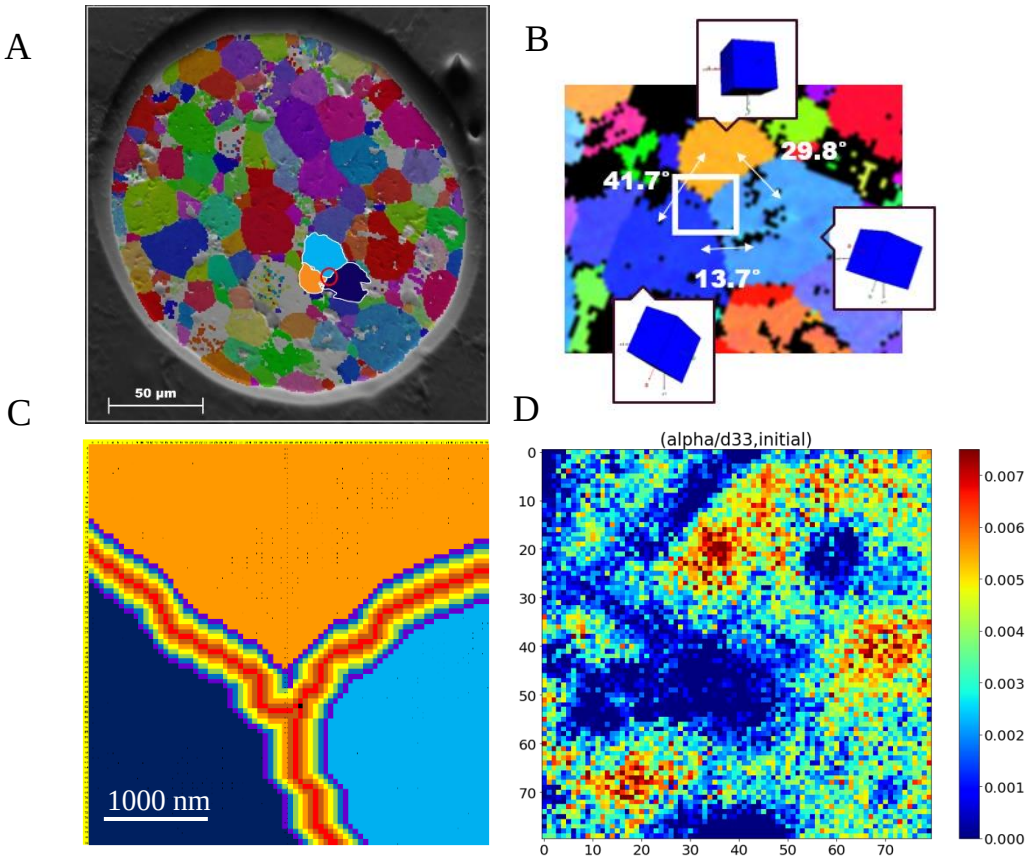

Figure 4-26: (A) EBSD orientation map overlaying the SEM of the electrode area (B) EBSD orientation map of region of interest with grain boundary misorientation marked. The white square denotes the PFM scan area, and the blue cubes represent the orientation of each grain. (C) Marked .CSV file to associate the raw data with the microstructure, where the red line denotes the grain boundary locations (D) PFM $\alpha/d_{33,init}$ map

in Figure 4-27, the average $\alpha/d_{33,init}$ is asymmetric with respect to the boundary after the first 200 nm but symmetric within this distance. This was the case for the previous CSL boundaries described in the purple-pink-fuchsia triple point.

The width of influence of the grain boundary on the irreversible to reversible ratio shows suppressed behavior out to around 17 pixels or ~850 nm into the orange grain. Compare this to the behavior in the light blue grain where a clear maximum is found ~600

nm from the pinning site; then further into the blue grain an average value of ~0.0030 cm/kV is achieved some 1300 nm into the grain. The local maxima followed by a return to an average value some distance from the grain boundary was also reported by Marincel.[4]

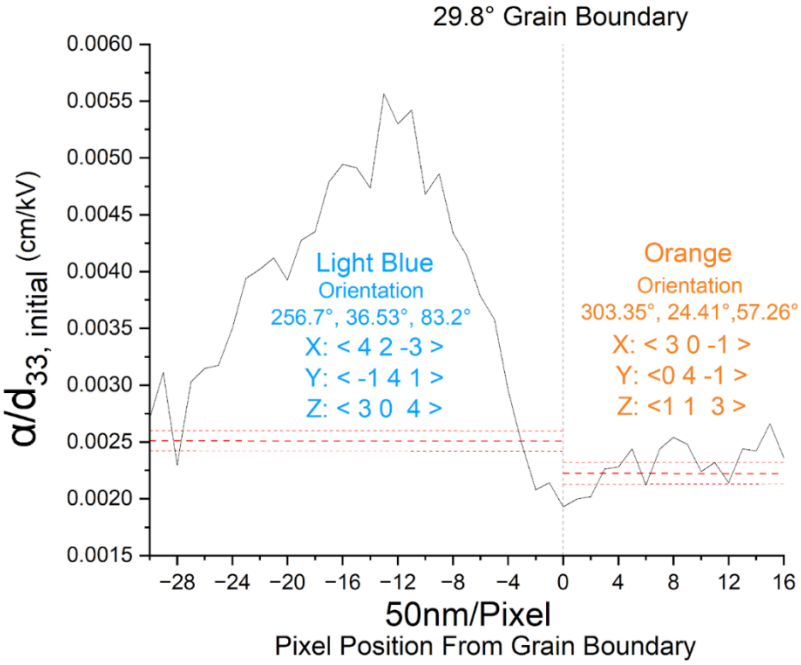

Figure 4-27: Average ratio of $\alpha/d_{33,init}$ with respect to proximity to the 29.8° grain boundary denoted as the center dotted line. The Euler angles and approximate orientations of each grain are shown with respect to the laboratory coordinates.

Shown in Figure 4-27 is the method 3 plot to determine the width of influence. It was found that the light blue reached its steady state as 153 ± 10 nm into the grain. The orange grain reached its steady state at 142 ± 45 nm for a total of 295 ± 55nm. Roughly the same steady value is reported for the orange grain in both the light blue – orange and dark blue - orange boundary.

In contrast, the light blue – dark blue grain boundary (13.7° random boundary) shown in Figure 4-28 is more symmetric than the light blue-orange grain boundary. The local minima for this grain boundary $\alpha/d_{33,init}$ is far lower at the zero position with a value

of 0.0006 cm/kV. The light blue reached its steady state according to method 3 at 141 ± 109 nm while the dark blue reached its steady state at 295 ± 107nm into the grain for a total width of influence of 436 ± 216nm.

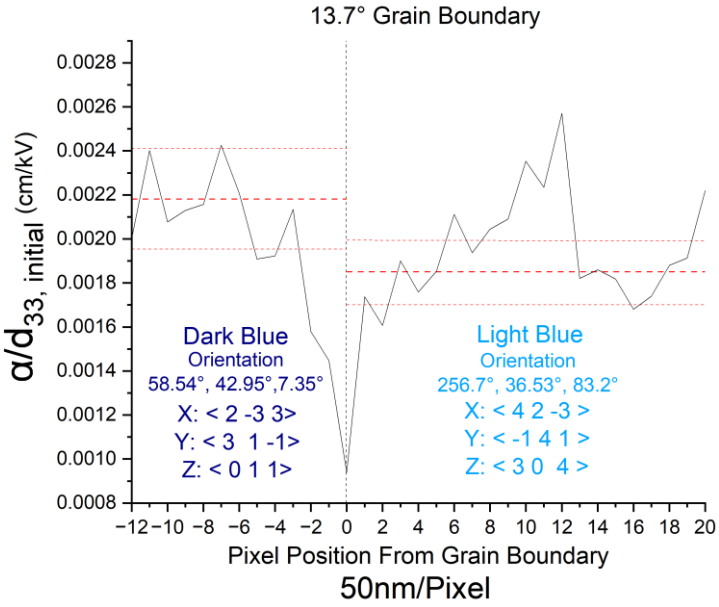

Figure 4-28: Average ratio of $\alpha/d_{33,init}$ with respect to proximity to the 13.7° grain boundary denoted as the center dotted line. The Euler angles and approximate orientations of each grain are shown with respect to the laboratory coordinates.

The final 41.7° dark blue – orange random grain boundary of this triple point shown in Figure 4-29 has a relatively asymmetric response. It is notable that the minima is an order of magnitude different between the dark blue-orange ($\alpha/d_{33,init}$ value of 0.00020 cm/kV) and light blue-orange ($\alpha/d_{33,init}$ value of 0.002 cm/kV) grain boundaries.

On the orange side of the boundary, utilizing method 3 the width of influence of the boundary pinning approached steady state at 485 ± 47nm into orange and 420 ± 105 nm for dark blue. The total width of influence calculated using method 3 for the dark blue-orange grain boundary is therefore 905 ± 152 nm, the largest influence investigated in this study using method 3. Therefore, in some cases, random grain boundaries demonstrated a

width of influence of ~ 1 μm, while the largest recorded CSL boundary influence of all the triple points was 572 ± 371 nm. Of particular interest is whether the static domain structures

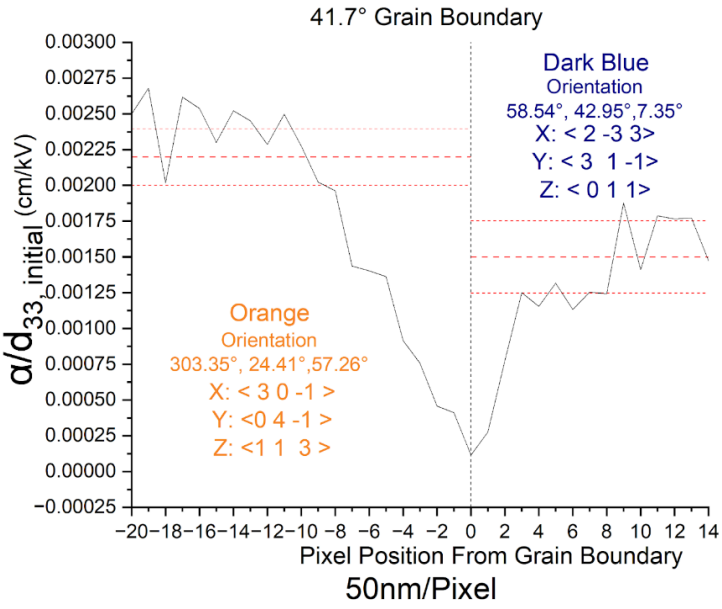

Figure 4-29: Average ratio of $\alpha/d_{33,init}$ with respect to proximity to the 41.7° grain boundary denoted as the center dotted line. The Euler angles and approximate orientations of each grain are shown with respect to the laboratory coordinates.

differ across these two types of boundaries.

In comparing random and CSL boundaries, the 29.8° CSL boundary had both the shallowest minima and lowest width of influence amongst the dark blue – light blue – orange triple point with a total width of influence of only 295 ± 55 nm compared to the large 905 ± 152 nm of the random 41.7° boundary. Notably these two *random* grain boundaries, similar to the case of purple-pink-fuchsia triple point, exhibit deeper minima of $\alpha/d_{33,init}$ compared to their associated CSL boundary neighbors. The tabulated values utilizing each method for the light blue – dark blue – orange triple point is shown in table 4-3.

Table 4-3: Methods 1-3 for light blue – dark blue – orange triple point, where the * denotes the CSL boundary and the – represents a value that could not be tabulated

Misorientation Angle	**13.7°**	**41.7°**	***29.8°**	**Triple Point Analysis**
Grain Boundary Pinning Distance (Method 1)	Dark Blue 563 ± 522 nm	Dark Blue 371± 222 nm	Orange 680 ± 426 nm	_____
	Light Blue 327 ± 206 nm	Orange 707 ± 405 nm	Light Blue 794 ± 636 nm	_____
Total Width of Influence	890 ± 728 nm	1078 ± 627 nm	1464± 1062 nm	675± 1313 nm
Misorientation Angle	**13.7°**	**41.7°**	***29.8°**	**Triple Point Analysis**
Grain Boundary Pinning Distance (Method 2)	Dark Blue 390 ± 72 nm	Dark Blue 93 ± 19 nm	Orange 283 ± 85 nm	_____
	Light Blue 290 ± 58 nm	Orange 223 ± 20 nm	Light Blue 250 ± 401 nm	_____
Total Width of Influence	680 ± 130 nm	316 ± 39 nm	533 ± 486 nm	540 ± 25 nm
Misorientation Angle	**13.7°**	**41.7°**	***29.8°**	**Triple Point Analysis**
Grain Boundary Pinning Distance (Method 3)	Dark Blue 295 ± 107 nm	Dark Blue 420 ± 105 nm	Orange 142 ± 45 nm	_____
	Light Blue 141 ± 109 nm	Orange 485 ± 47 nm	Light Blue 153 ± 10 nm	_____
Total Width of Influence	436 ± 216 nm	905 ± 153 nm	295 ± 55 nm	1052 ± 76 nm

Uncovering local structure features tied to strong pinning is fundamental to this work, but equally important is finding features that instead induce very little pinning. In light of this, the next sample region discussed will show behavior with no evidence of pinning despite the presence of a 45.1° grain boundary. Shown in Figure 4-30 (A) and (B) is the region of interest as well as a visualization of their orientations, the scan region, and the misorientation angles. Separating the pink and blue grains of (A-C) is a 45.1° grain

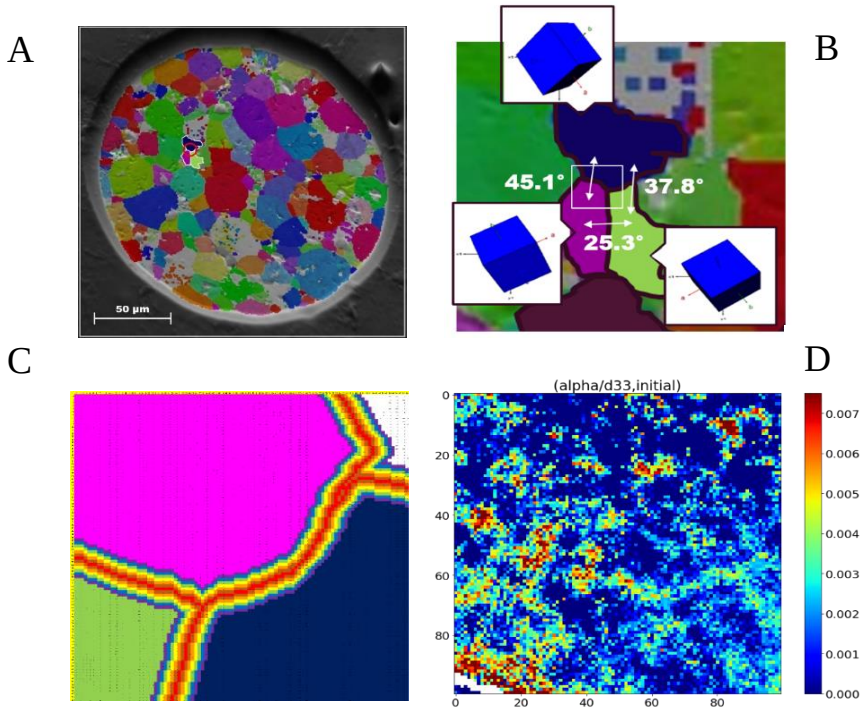

Figure 4-30: (A) EBSD Orientation map overlaying the SEM of the electrode area (B) EBSD Orientation map of region of interest with grain boundary misorientation marked. The white square denotes the PFM scan areas, and the blue cubes represent the orientation of each grain. (C) Marked .CSV file to associate raw data with microstructure locations where the red line denotes the grain boundary locations (D) PFM $\alpha/d_{33,init}$ map from which the .CSV numbers were collected

boundary that is anomalous: the $\alpha/d_{33,init}$ map in (D) shows little association with the grain boundary region marked in (C), and thus the average $\alpha/d_{33,init}$ relative to the grain boundary demonstrates no correlation with approaching the boundary location and shows its minima some 500nm into the pink grain as shown Figure 4-31.

In contrast, the blue region shows a minima in $\alpha/d_{33,init}$ near the boundary; utilizing method 3 a pinning influence of 382 ± 14 nm was determined. The blue-green grain

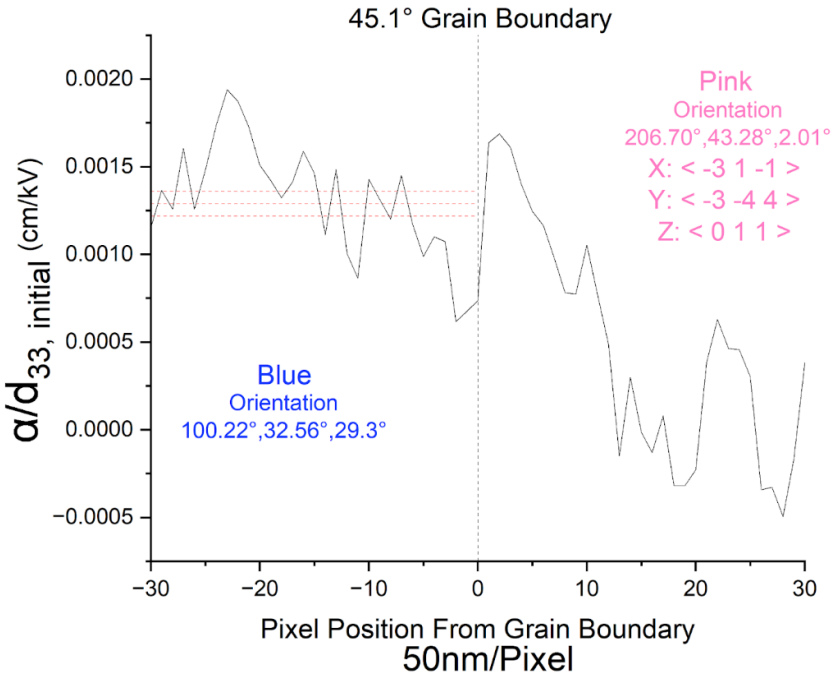

Figure 4-31: Average ratio of $\alpha/d_{33,init}$ with respect to proximity to the 45.1° grain boundary denoted as the center dotted line. The Euler angles and approximate orientations of each grain are shown with respect to the laboratory coordinates.

boundary shown in Figure 4-32 has an average $\alpha/d_{33,init}$ response in the blue region that is comparable to that of the blue grain response adjacent to the blue-pink boundary of Figure 4-31.

The green grain approaches its steady state $\alpha/d_{33,init}$ value approximately 284 ± 113 nm from the grain boundary utilizing method 3 and 575 ± 73 nm into the blue grain for a total of 859 ± 186 nm width of influence. All three of the analyzed boundaries of blue-pink-green show $\alpha/d_{33,init}$ minima at the grain boundary that are an order of magnitude smaller than the others investigated. In future work, it will be important to assess whether this significant difference is correlated with the comparatively smaller $SrTiO_3$ grain areas here; the respective sizes of each grain are 45 μm^2 for pink, 138 μm^2 for green, and 83 μm^2

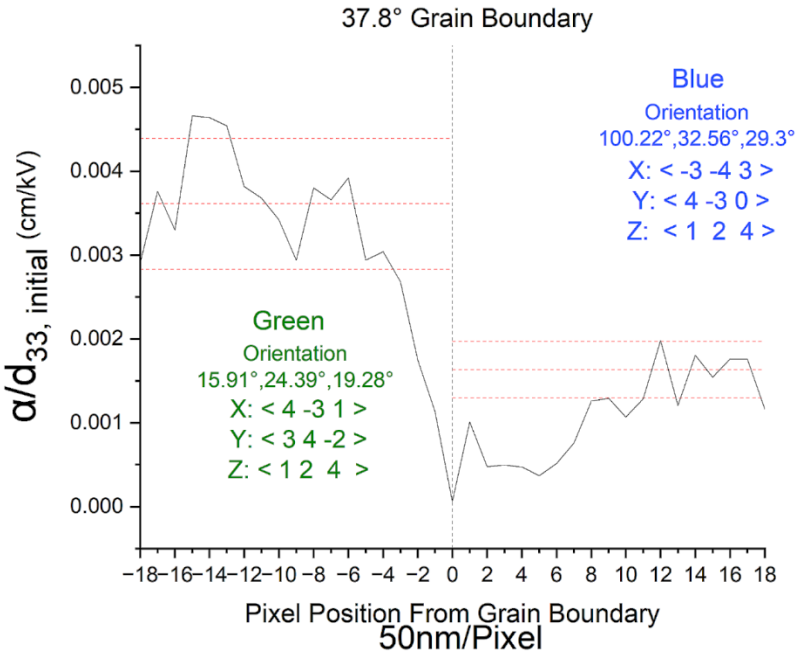

Figure 4-32: Average ratio of $\alpha/d_{33,init}$ with respect to proximity to the 37.8° grain boundary denoted as the center dotted line. The Euler angles and approximate orientations of each grain are shown with respect to the laboratory coordinates.

for blue. Additionally, all three of the boundaries in this region also correspond to random boundaries which has been correlated with the deepest pinning levels in each of the studied triple points. Therefore a triple point of three random boundaries may exacerbate this finding and contribute to the lowest reported $\alpha/d_{33,init}$ minima. In future work, it will also be important to assess whether this significant difference is correlated with the comparatively smaller $SrTiO_3$ grain, a larger number of random boundaries, or a difference in the local domain configuration.

The final boundary investigated for this same triple point is the 25.3° random boundary that separates green and pink grains in Figure 4-33. The spatial variation in $\alpha/d_{33,init}$ is relatively symmetric with respect to this boundary. This was also the only investigated boundary that showed a negative value for $\alpha/d_{33,init}$. The negative value at

position zero suggests a non-Rayleigh behavior that could be the result of a non-uniform distribution of restoring forces for the domain walls. This could be due to an anomalously strong pinning site. The width of influence for the 25.3° random boundary was 124 ± 23 nm into the green and 166 ± 36 nm into the pink for a total width of influence at 290 ± 59 nm. The tabulated values utilizing each method for the green – blue – pink triple point is shown in Table 4-4.

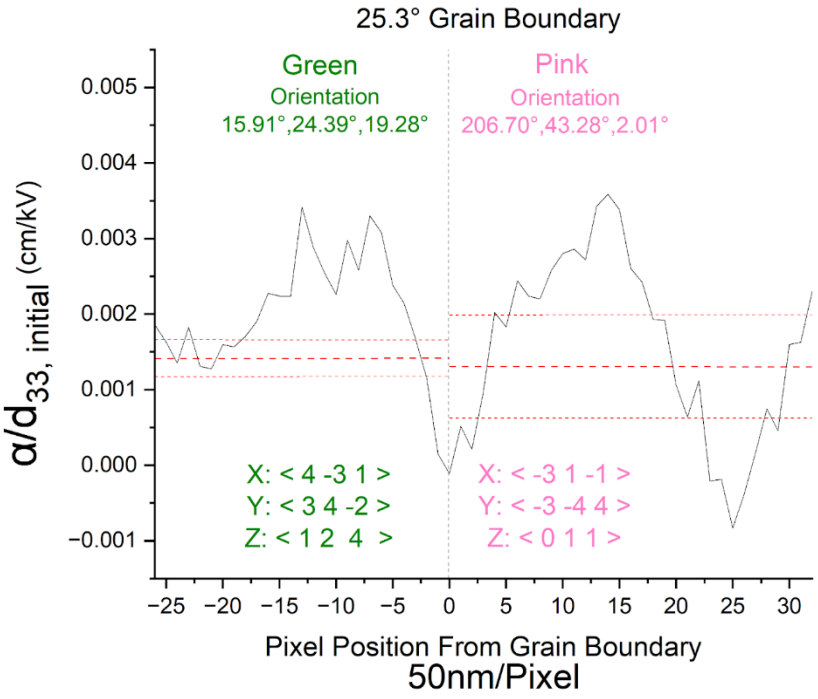

Figure 4-33: Average ratio of $\alpha/d_{33,init}$ with respect to proximity to the 25.3° grain boundary denoted as the center dotted line. The Euler angles and approximate orientations of each grain are shown with respect to the laboratory coordinates.

Table 4-4: Methods 1-3 showing the width of influence for green – blue – pink triple point. where the * denotes the CSL boundary and the – represents a value that could not be tabulated.

Misorientation Angle	**25.3°**	**37.8°**	**45.1°**	**Triple Point Analysis**
Grain Boundary Pinning Distance (**Method 1**)	Green 112 ± 150 nm	Green 195 ± 165nm	Pink 20nm ± 32 nm	_____
	Pink 134 ± 146 nm	Blue 372 ± 351 nm	Blue 276 ± 127 nm	_____
Total Width of Influence	246 ± 296 nm	567 ± 516 nm	296 ± 159 nm	835 ± 1797 nm
Misorientation Angle	**25.3°**	**37.8°**	**45.1°**	**Triple Point Analysis**
Grain Boundary Pinning Distance (**Method 2**)	Green 142 ± 16 nm	Green 330 ± 79 nm	Pink _____	_____
	Pink 173 ± 24 nm	Blue 155 ± 20 nm	Blue 110 ± 74 nm	_____
Total Width of Influence	315 ± 40 nm	485 ± 99 nm	_____	738 ± 55 nm
Misorientation Angle	**25.3°**	**37.8°**	**45.1°**	**Triple Point Analysis**
Grain Boundary Pinning Distance (**Method 3**)	Green 124 ± 23 nm	Green 284 ± 113 nm	Pink _____	_____
	Pink 166 ± 36 nm	Blue 575 ± 73 nm	Blue 382 ± 14 nm	_____
Total Width of Influence	290 ± 59 nm	859± 186 nm	_____	1036 ± 60 nm

The next point of study is the circular width of influence at each of the investigated triple point locations. In order to collect the response with respect to increasing distance from the triple point, the .CSV file was analyzed at increasing near-circle shapes using the radius of pixels distance from the triple point as a guideline and averaging the points on the perimeter it creates. Points far from the triple point were used to collect an average and

standard deviation for method 3, and to set the bounds for high and low response for the first two methods. It should be noted that the number of pixels being considered increases as the radius of the circular region grows and can therefore yield high standard deviations and error bars for method one in particular. An example of the circular analysis can be seen at the center of the green-pink-blue triple point in Figure 4-34.

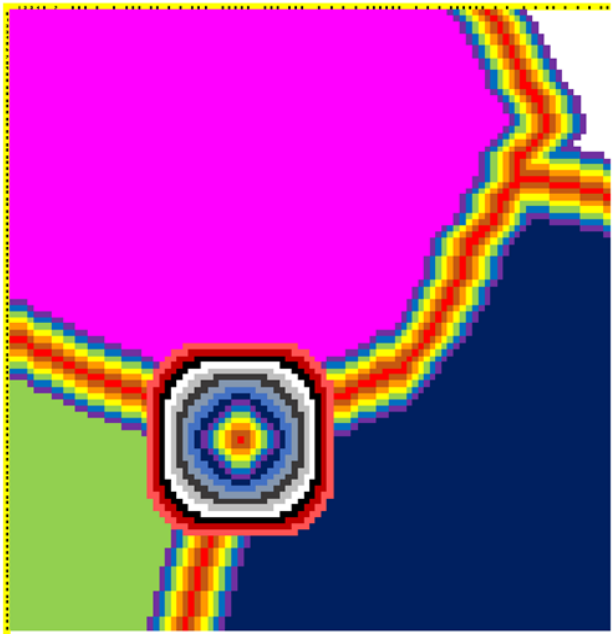

Figure 4-34: Formatted excel file for $\alpha/d_{33,init}$ with respect to proximity to increasing circular area surrounding the green-blue-pink triple point.

The values for the width of influence of the triple points have been collected along the right column of Table 4-2, 4-3, and 4-4 for each respective triple point. It was found that triple points typically serve as deep pinning sites, for which domain wall motion is degraded hundreds of nm away on any side of the triple point. At the triple points, the nonlinear piezoelectric response is often non-Rayleigh-like in character, suggesting that the domain walls locally see a non-Gaussian set of restoring forces. This non-Rayleigh behavior takes the form of a negative $\alpha/d_{33,init}$.

Let us first consider the circular width of influence of the light blue-orange-dark blue triple point. Shown in Figure 4-35 is the average $\alpha/d_{33,init}$ plotted with respect to increasing distance from the triple point with the width of influence calculated using method 3. Figure 4-35 suggests that the average $\alpha/d_{33,init}$ remains non-Rayleigh in character at length scales up to 279 nm in any direction from the triple point. The distance of non-Rayleigh behavior was found to be an average distance of 220 nm in any direction across all the triple points investigated. The associated minima value at the exact pixel location of the triple point was found to be -0.0024 cm/kV. The non-Rayleigh-like behavior could in

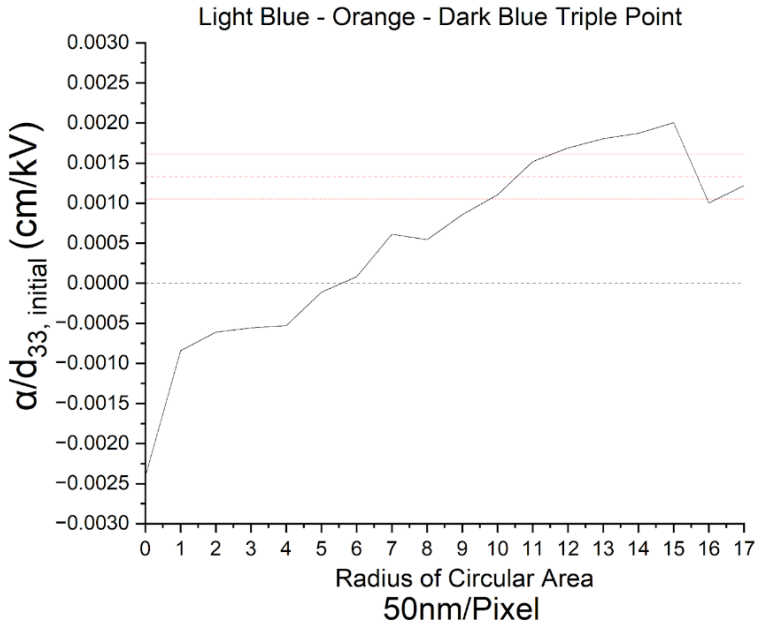

Figure 4-35: Average $\alpha/d_{33,init}$ with respect to proximity to increasing circular area surrounding the light blue – orange – dark blue triple point. The horizontal black dotted line represents the point at which the $\alpha/d_{33,init}$ becomes positive with respect to distance the red line represent the mean and 0.25% standard deviation used for error calculation.

principle, be due either to a region with no domain walls, or to a volume where the restoring forces for domain walls is not uniformly distributed.

The calculated triple point width of influence stretches beyond the non-Rayleigh regime, for a radial width of influence of 527 ± 38 nm using method 3 and 540 ± 25 nm utilizing method 2. The diameter width of influence therefore stretches 1052 ± 76 nm using method 3 for this triple point. This large width of influence is reasonable given the stronger pinning demonstrated by the strongly negative $\alpha/d_{33,init}$ minima.

Using methods 1 and 2, it was difficult to quantify a percentage of pixels that fell above a threshold, since the number of pixels changes with the radius. This differed from the case of grain boundaries, where a constant number of data points were typically available parallel to the boundary.

Compare this to the width of influence about the purple-pink-fuchsia triple point in Figure 4-36. The non-Rayleigh behavior for this triple point exists only for ~50 nm in any direction and demonstrates the shallowest minima of the three triple points with a recorded $\alpha/d_{33,init}$ of -0.00011 cm/kV at the triple point location. This triple point had more identified CSL grain boundaries than the others investigated, consistent with the trend of decreased pinning with shared rotation between grains. Additional measurements on other triple points should be made in the future to assess whether there is statistical significance to the correlation between a less negative $\alpha/d_{33,init}$ and the character of the grain boundary as well as its preferred axis of rotation. The $\alpha/d_{33,init}$ reaches an average value at a radial width of 345 ± 9 nm from the triple point utilizing method 3 for a total width of influence of 690 ± 18 nm. Additional random boundaries should be investigated to determine if the random boundaries tend to have a maximum in $\alpha/d_{33,init}$ at some consistent distance from the boundary**.** It should also be noted that all three methods found the pink – purple – fuchsia

triple point, with the most defined CSL boundaries, to have the smallest width of influence prior to steady state.

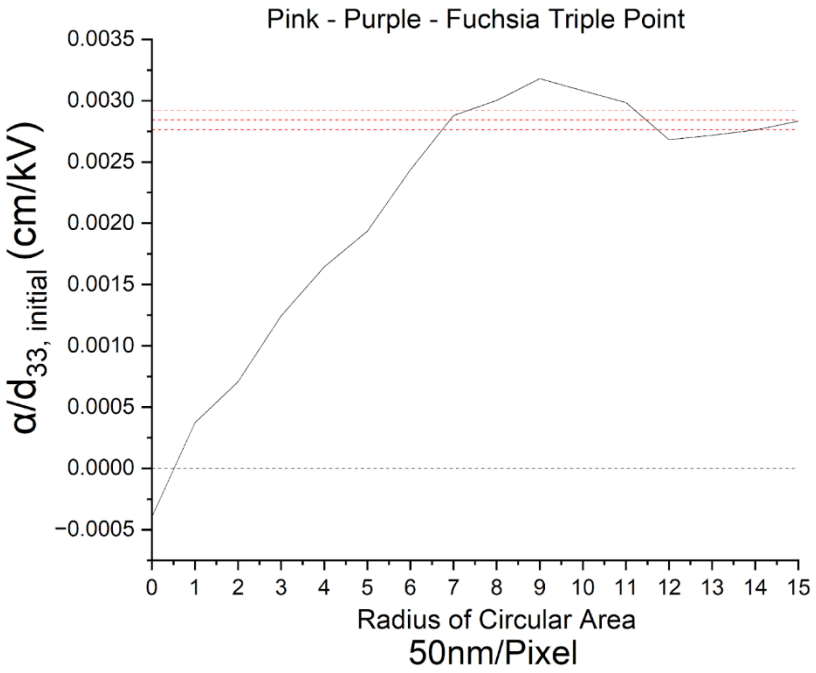

Figure 4-36: Average $\alpha/d_{33,init}$ with respect to proximity to the fuchsia – purple – pink triple point. The horizontal black dotted line represents the point at which the $\alpha/d_{33,init}$ becomes positive with respect to distance the red line represent the mean and 0.25% standard deviation used for error calculation

The triple point of green-blue-pink in Figure 4-37 shows both the lowest recorded minima at its triple point location, and the longest length scale away from the pinning center before reaching Rayleigh behavior. The minima of -0.004 cm/kV and non-Rayleigh behavior up to ~375 nm suggest that increased pinning drives a non-Gaussian set of restoring forces further into the grain region. Based on the limited number of boundaries measured here, it is notable that the shallowest minima in $\alpha/d_{33,init}$ corresponds to a shorter length scale of non-Rayleigh character for the asymmetric boundaries. Method 3 estimates the radial width of influence of the triple point to be 518 ± 30 nm for a total width of 1036 ± 60 nm. This observation differs from the report of Marincel et al. on symmetrical twist

boundaries which had a very deep pinning minima, but a short width of influence.[4] It should also be noted that all three of the boundaries in this region correspond to random boundaries which has been attributed to the deepest pinning levels in each of the studied triple point's grain boundaries and in this case the deepest minimum $\alpha/d_{33,init}$ with respect to the exact triple point location.

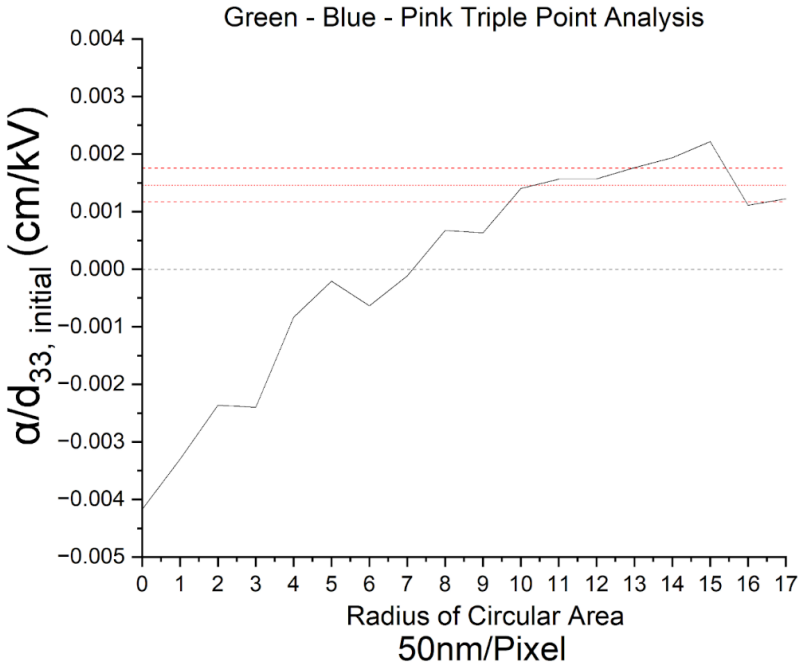

Figure 4-37: Average $\alpha/d_{33,init}$ with increasing circular area surrounding the green-blue-pink triple point. The horizontal black dotted line represents the point at which the $\alpha/d_{33,init}$ becomes positive with respect to distance the red lines represent the mean and 0.25% standard deviation used for error calculation.

For the green-pink-blue triple point, non-Rayleigh like behavior for $\alpha/d_{33,init}$ response was observed 350 nm from the triple in each grain; utilizing method 3, a radial width of influence of 518 ± 60 nm was determined for a total of 1036 ± 60 nm. Additional triple point investigations will be required to confirm the trends based on the rotation axis of CSL boundaries, however in increasing the number of random boundaries within the

triple point it was found that an increased distance before reaching Rayleigh like behavior, and steady state $\alpha/d_{33,init}$ was observed.

Chapter 5

Conclusions and Future Work

5.1 Local Epitaxial Growth on Polycrystalline Substrates

The primary focus of this work is classifying local pinning sites for their impact on dielectric and piezoelectric properties. To that end, PZT films were grown with local epitaxy on polycrystalline $SrTiO_3$ substrates such that they could exhibit a larger variety of grain orientations to analyze for pinning. Electron backscatter diffraction was used map the underlying grain orientations so that piezoresponse force microscopy measurements were collected at known locations of grain boundary triple points to evaluate the nonlinear response with respect to local pinning sites.

It was found that surface roughness limits the ability to collect orientation maps on thin film samples. This roughness, combined with nucleation of misoriented grains precluded the use of PZT films deposited via PLD. EBSD with Kikuchi patterns that could be consistently analyzed by the detector were achievable for the first 100 nm of film thickness; beyond that zero solutions became more prevalent seemingly because of the increased film thickness led to increased secondary nucleation of very small grains with respect to the $SrTiO_3$ grain boundaries under investigation. Beyond a PZT thickness of ~250 nm, no Kikuchi patterns were not indexable in PLD deposited. In contrast, chemical solution deposited PZT films up to 1000 nm thick were smooth enough to detect and index strong Kikuchi patterns. The majority of the electrode area had regions of uniform orientation that corresponded to the length scale of the underlying $SrTiO_3$ grains. Thus,

CSD deposited PZT films were utilized for subsequent studies in the final thin film sample stacks.

5.2 Grain Boundary-Piezoresponse Interaction

Individual grain boundaries were investigated by PFM to assess their pinning potential and the factors driving its behavior. It was found that different grain boundaries influenced the mobility of domain walls on length scales from 124 ± 23 nm to 575 ± 73nm normal to their respective grain boundary. The largest width of influence recorded up to 905 ± 153 nm. In analyzing trends between misorientation angle and pinning strength it was found those boundaries classified with random grain orientation with respect to their neighboring grains did play a role. Coincident site lattice (CSL) grain boundaries exhibited a lesser degree of pinning with a deeper minima of $\alpha/d_{33,init}$ found for random grain boundaries. That is, regularity in the crystalline arrangement of the two grains may lead to easier collective movement between grains. All three of the analyzed boundaries of blue-pink-green, for example, show $\alpha/d_{33,init}$ far deeper minima than the others investigated. All three of the boundaries in this region also correspond to random boundaries which has been attributed to the deepest pinning levels in each of the studied triple points. Therefore a triple point of three random boundaries may exacerbate the pinning and contribute to the lowest reported $\alpha/d_{33,init}$ minima. While minima served as a means to compare the pinning at boundary position zero; it was found that the width of influence on domain wall motion scaled better with the difference between the minima and the steady state $\alpha/d_{33,init,}$ then it did with the value of $\alpha/d_{33,init}$ at the grain boundary itself. That is, wider widths of influence

were observed in cases with larger differences between the minima and the steady state $\alpha/d_{33,init.}$. It is also notable that CSL boundaries are the ones that have been reported to enable continuity if the domain structure across boundaries in the reports of Mantri et al.[30] With regards to grain size, in some cases, smaller grains showed stronger pinning on shorter length scales, however this is not true across all investigated boundaries but rather in addressing the sizes of the individual grains that comprise each triple point themselves.

5.3 Triple Point-Piezoresponse Interaction

It was also found that triple points with random grain boundaries led to a deeper minima for $\alpha/d_{33,init.}$ That is, a larger number of non-CSL grain boundaries led to an increased pinning. For example, the fuchsia-purple-pink triple point had two CSL boundaries and a significantly smaller region of non-Rayleigh behavior observed to 25 nm from the triple point; the radial width of influence on domain wall motion was 690 ± 18nm according to method 3. Furthermore, the associated minima for $\alpha/d_{33,init}$ at the triple point was comparatively shallow with a value of -0.0005 cm/kV. In contrast, the green-pink-blue triple point, for which all three of the boundaries were random, showed the deepest minima of $\alpha/d_{33,init}$ and a radial width of influence on domain wall motion of 1036 ± 60 nm . Thus, the width of influence of a triple point can extend across the length scale of dozens of PZT grains based on their average grain size measurements. There were no universal trends found based on the average grain size or average misorientation angle. That said, many additional triple points should be interrogated to provide better statistical evidence for the conclusion. Uncovering specific CSL rotation axes that enable decreased pinning could

prove useful with an increased triple point sample size. Of interest would be contrasting the domain structure both within the reported triple point width of influence and the domain structure outside of it. Reporting on a larger variety of triple points should enable a deeper investigation of the various CSL preferred rotations and their domain pinning.

5.4 Future Work

By improving the understanding of the pinning potential with respect to various microstructure and sample conditions, future models can be developed that better quantify their influence on domain wall or phase boundary mobility. This thesis work addressed the nonlinearity of the piezoresponse about a select number of triple points and various grain boundary misorientation angles.

The first suggested piece of future work is to expand the number of grain boundaries and triple points interrogated, to improve the statistical significance of the conclusions. Of interest is to determine whether the underlying grain size or the grain boundary misorientation has a stronger influence on the domain response across a larger variety of pinning sites. Drawing trends from a limited number of triple points can lead to incomplete assessments of the trends in pinning strength. In considering the response beneath a greater number of electrodes, more triple points can be catalogued, and stronger trends can be developed for the impact of domain continuity on nonlinearity. For example, a more complete set of coincident site lattice boundaries should be analyzed for comparison to randomly oriented grain neighbors, and addressed based on their shared rotation axis.

To further uncover the mechanisms behind domain wall pinning, Dark Field X-ray Microscopy should be used to spatially map the domain structures near grain boundaries and triple points. It is of interest to deconvolute the property impacts driven by the stationary domain structure to those that are driven from the evolving motion of domain walls. Dark Field X-ray microscopy should allow the relative roles of static domain structure and domain wall movement on nonlinearity around grain boundaries to be identified.

The factors that lead to domain continuity across grains must also be addressed in greater detail. Of interest is determining whether there is a quantitative lower limit of pinning strength that enables irreversible motion or a specific field value that induces collective motion. Assessing the behavior along a given grain boundary as a function of proximity to the triple point is also important, as it possible that the domain structure itself change as the triple point is approached. The use of Dark Field X-ray microscopy should enable a greater understanding of collective motion visually based on continuation of the initial structure. This initial structure and its relation to triple point proximity can then be paired with a quantitative pinning analysis of PFM scans. Ultimately it would be useful to assess the domain cluster size as well as the domain wall density and resultant property influence surrounding the large domain clusters.

The impact of sample stress states and grain sizes should also be addressed further in its effect on domain wall movement in polycrystalline samples. To do so a range of different polycrystalline substrates beyond $SrTiO_3$ should be considered. The use of different polycrystalline substrates should enable an analysis of grain sizes at different scales as well as different average stress states based on the thermal expansion mismatch

between the underlying substrate and the film under the high processing temperatures. In quantifying these factors, future ferroelectric models can be developed that better consider the sample factors with respect to microstructure and processing.

References

1. Jaffe, B., Cook, W. R. & Jaffe, H. *Piezoelectric Ceramics* (1971).

2. Swartz, S.L., Wood, V.E., "Ferroelectric Thin Films," *Condensed Matter News*, vol. 1, no. 5, pp. 4-13 (1992).

3. Kratzer, P., et al. "First-Principles Studies of Kinetics in Epitaxial Growth of III-v Semiconductors." *Applied Physics A: Materials Science & Processing*, vol. 75, no. 1, 2002, pp. 79–88 (2002).

4. Marincel, D. M., Zhang, H., Kumar, A., Jesse, S., Kalinin, S. V., Rainforth W. M., Reaney, I. M., Randall, C. A., and Trolier-McKinstry S., "Influence of crystal defects on domain wall motion in ferroelectrics," *Advanced Functional Materials*, vol. 24, no. 10, pp. 1409– 1417, (2014).

5. Kratzer, M, Lasnik, M, Röhrig, S, Teichert, C, Deluca, M. "Reconstruction of the domain orientation distribution function of polycrystalline PZT ceramics using vector piezoresponse force microscopy". *Sci Rep.* 2018 Jan 11;8(1):422. (2018).

6. Randall, C.A., Barber, D.J., and Whatmore, R.W., "Ferroelectric domain configurations in a modified-PZT ceramic". *Journal of Material Science* 22, 925–931 (1987).

7. Mayergoyz, I. D., "Mathematical Models of Hysteresis," *Phys. Rev. Lett.* 56, 1518 - 1521 (1986).

8. Newnham R. E., *Properties of Materials: Anisotropy, Symmetry, Structure* (Oxford University Press, Oxford, 2005).

9. Mayergoyz, I. D., “Chapter 4: Hysteresis in Piezoelectric and Ferroelectric Materials.” *The Science of Hysteresis*, vol. 3, Elsevier/Academic Press, Amsterdam, 2006, pp. 345–346. (2006).
10. Frantti, J., Jaffe, B., Roth, R. S., & Marzullo, S. “Piezoelectric Properties of Lead Zirconate-Lead Titanate Solid Solution Ceramics”. *Journal of Applied Physics* 25, 809–810 (1954).
11. Moulson, A. & Herbert, J. *Electroceramics: Materials, Properties, Applications* 2nd Ed. (John Wiley & Sons, West Sussex, 2003).
12. Speck J. S., Seifert A., Pompe, W., and Ramesh, R., “Domain configurations due to multiple misfit relaxation mechanisms in epitaxial ferroelectric thin films. II. Experimental verification and implications,” *J. Appl. Phys*., vol. 76, no. 1, p. 477, (1994).
13. Emelyanov, A. Y., Pertsev, N. A., and Kholkin, A. L., “Effect of external stress on ferroelectricity in epitaxial thin films,” *Phys. Rev. B*., 66, 214108 (2002).
14. Kalpat, S., and K. Uchino. “Highly Oriented Lead Zirconium Titanate Thin Films: Growth, Control of Texture, and Its Effect on Dielectric Properties.” *Journal of Applied Physics*, vol. 90, no. 6, 2001, pp. 2703–2710. (2001).
15. Chrisey, D. B., and Hubler, G. K. *Pulsed Laser Deposition of Thin Films*. Wiley-Interscience 1st Edition, 1994. (1994).
16. Schwartz, R. W. “Chemical Solution Deposition of Perovskite Thin Films.” *Chemistry of Materials*, vol. 9, no. 11, 1997, pp. 2325–2340. (1997).

17. Shoghi, A., Abdizadeh, H., Shakeri, A. *et al.* Sol–gel synthesis of PZT thin films on FTO glass substrates for electro-optic devices. *J Sol-Gel Sci Technol* **93,** 623–632 (2020).

18. Shirane G., Suzuki, K., and Takeda, A. "Phase Transitions in Solid Solutions of $PbZrO_3$ and $PbTiO_3$*" J. Phys. Soc. Japan* vol. **7,** no. 12 (1952).

19. Randall, C., Kim, N., Kucera, J.-P., Cao, W. & Shrout, T. R. Intrinsic and Extrinsic Size Effects in Fine-Grained Morphotropic-Phase-Boundary Lead Zirconate Titanate Ceramics. *Journal of the American Ceramic Society* 81, 677–688 (2005).

20. Noheda, B., Gonzalo, J., Guo, R., Park, S.E., Cross, L.E., Cox, D., Shirane, G. "The monoclinic phase in PZT: New light on morphotropic phase boundaries." *Fundamental Physics of Ferroelectrics*. 535. 10.1063/1.1324468 (2000).

21. Noheda, B., et al. "Stability of the Monoclinic Phase in the Ferroelectric Perovskite $PbZr_{1-x}Ti_xO_3$." *Physical Review B,* vol. 63, no. 1, 2000,

22. Du, X.-H., Zheng, J., Belegundu, U. & Uchino, K. "Crystal Orientation Dependence of Piezoelectric Properties of Lead Zirconate Titanate Near the Morphotropic Phase Boundary.*" Applied Physics Letters* 72, 2421–2423 (1998).

23. Welberry, T., Goossens, D., Withers, R. et al. "Monte Carlo Simulation Study of Diffuse Scattering in PZT, $Pb(Zr,Ti)O_3$." *Metall Mater Trans A* 41, 1110–1118 (2010).

24. Damjanovic D. and Demartin, M. "Contribution of the irreversible displacement of domain walls to the piezoelectric effect in barium titanate and lead zirconate titanate ceramics," *J. Phys.: Condens. Mater* 9, 4943-4953 (1997).

25. Bassiri Gharb, N., Fujii, I., Hong, E., Trolier-McKinstry, S., Taylor, D. V., and Damjanovic, D. “Domain Wall Contributions to the Properties of Piezoelectric Thin Films,” *Journal of Electroceramics* 19 47 - 65 (2007).
26. Fousek, J. “Permissible domain walls in ferroelectric species,” Czechoslov. *J. Phys.*, vol. 21, no. 9, pp. 955–968, Sep. (1971).
27. Sapriel, J. “Domain-Wall Orientations in Ferroelastics.” *Physical Review B*, vol. 12, no. 11, 1975, pp. 5128–5140 (1975).
28. Fousek, J. and Janovec, V. “The orientation of domain walls in twinned ferroelectric crystals,” *J. Appl. Phys*., vol. 40, no. 1, p. 135, (1969).
29. Neel, L. “Theorie du Trainage Magnetique des Substances Massives dans le Domaine de Rayleigh,” Le Journal de Physique et le Radium 11 49 – 61 (1950).
30. Mantri S., Oddershede, J., Damjanovic D., and Daniels, J. E. “Ferroelectric Domain Continuity over Grain Boundaries,” *Acta Mat.* 128 400-405 (2017).
31. Schultheiß, J., Checchia, S., Uršič, H., Frömling, T., Daniels, J.E., Malič, B., Rojac, T., Koruza, J. “Domain wall-grain boundary interactions in polycrystalline $Pb(Zr_{0.7}Ti_{0.3})O_3$ piezoceramics” *Journal of the European Ceramic Society*, 40, 12, 3965-3973 (2020).
32. Bintachitt, P., et al. “Collective Dynamics Underpins Rayleigh Behavior in Disordered Polycrystalline Ferroelectrics.” *Proceedings of the National Academy of Sciences*, vol. 107, no. 16, 2010, pp. 7219–7224 (2010)
33. Smolenskiĭ G. A. “Ferroelectrics and Related Materials.” *Gordon and Breach Science Publishers*, (1984).

34. Arlt G., and Dederichs, H. “Complex elastic, dielectric and piezoelectric constants by domain wall damping in ferroelectric ceramics”, *Ferroelectrics*, 29:1, 47-50, (1980).

35. Yamazaki, T., Furuya, Y., Nakao, W. “Experimental evaluation of domain wall dynamics by Barkhausen noise analysis in $Fe_{30}Co_{70}$ magnetostrictive alloy wire” *Journal of Magnetism and Magnetic Materials*, Vol. 475, ISSN 0304-8853, (2019).

36. Schultheiß, J., Checchia, S., Uršič, H., Frömling, T., Daniels, J.E., Malič, B., Rojac, T., Koruza, J., “Domain wall-grain boundary interactions in polycrystalline $Pb(Zr_{0.7}Ti_{0.3})O_3$ piezoceramics” *Journal of the European Ceramic Society*, Vol. 40, Issue 12, 2020, pp 3965-3973, (2020).

37. Griggio, F., and Trolier-McKinstry, S. “Local Piezoelectric Behavior in PZT-Based Thin Films for Ultrasound Transducers.” *Pennsylvania State University,* (2011).

38. Damjanovic, D. & Demartin, M. The Rayleigh Law in Piezoelectric Ceramics. *Journal of Physics D: Applied Physics* vol. 29, pp. 2057–2060 (1996).

39. Trolier-McKinstry S., Bassiri-Gharb N., and Damjanovic D., “Piezoelectric nonlinearity due to motion of 180° domain walls in ferroelectric materials at subcoercive fields: A dynamic poling model,” *Appl. Phys. Lett*., vol. 88, no. 20, p. 202901, (2006).

40. Zapperi, S., Magni, A., Durin, G “Microscopic foundations of the Rayleigh law of hysteresis.” *Journal of Magnetism and Magnetic Materials*. 242. 10.1016/S0304-8853(01)01131-3. (2001).

41. Lacey, J. “Effect of Dopants and Microstructure on Properties of PZT deposited via Pulsed Laser Deposition” *The Graduate School College of Earth and Mineral Sciences*. Diss. The Pennsylvania State University, (1997).

42. Kronmuller, H. “Statistical Theory of Rayleigh’s Law,” Z. Angew. *J. Physik* 30, 9 (1970).

43. Taylor, D.V., and Damjanovic, D. “Evidence of Domain Wall Contribution to the Dielectric Permittivity in PZT Thin Films at Sub-switching Fields,” *J. Appl. Phys*. 82 1973-1975 (1997).

44. Marincel, D. M., Zhang, H. R., Britson, J., Belianinov, A., Jesse, S., Kalinin, S.V. Chen, L. Q., Rainforth, W. M., Reaney, I. M., Randall, C. A., and Trolier-McKinstry, S. “Domain Pinning Near a Single-Grain Boundary in Tetragonal and Rhombohedral Lead Zirconate Titanate Films,” *Phys. Rev. B* vol. 91, 134113 (2015).

45. Boser, O. “Statistical-Theory of Hysteresis in Ferroelectric Materials,” *J. Appl. Phys.* 62, 1344-1348 (1987).

46. Stewart, M & Cain, Markys & Hall, David. “Ferroelectric hysteresis measurement and analysis” *Report CMMT* (A). vol 152. (1999).

47. Kim, G. H. “An Analysis of Imprinted Hysteresis Loops for a Ferroelectric $Pb(Zr,Ti)O_3$ Thin Film Capacitor Using the Switching Transient Current Measurements.” *Journal of Applied Physics*, vol. 105, no. 4, 2009, p. 044106. (2009).

48. Maria, J-P., Trolier-McKinstry, S., Schlom, D. G., Hawley, M. E., Brown, G. W. “The influence of energetic bombardment on the structure and properties of epitaxial $SrRuO_3$ thin films grown by pulsed laser deposition.” *Journal of Applied Physics 83(8), 4373–0.* (1998).

49. Maria, J-P. “Epitaxial $Pb(Mg_{1/3}Nb_{2/3})O_3$ -$PbTiO_3$ Thin Films.” *Pennsylvania State University*, UMI, (1998).

50. Shoghi, A., Abdizadeh, H., Shakeri, A. *et al.* “Sol–gel synthesis of PZT thin films on FTO glass substrates for electro-optic devices.” *J Sol-Gel Sci Technol* **93,** 623–632 (2020).

51. Dey, S.K., Budd, K.D., Payne D. A. “Thin-film ferroelectrics of PZT of sol-gel processing” *IEEE Trans Ultrason Ferroelectr Freq Control*. vol. 35(1): 80-1 (1988).

52. Lowe, M. J., et al. “Electron Backscatter Diffraction and Piezoresponse Force Microscopy Study of Bulk and Thin Film PZT Samples.” *Integrated Ferroelectrics,* vol. 98, no. 1, 2008, pp. 136–143. (2008.)

53. Seal, K., Jesse, S., Nikiforov, M, Kalinin, S., Fujii, I, Bintachitt, P., and Trolier-McKinstry, S. “Spatially Resolved Spectroscopic Mapping of Polarization Reversal in Polycrystalline Ferroelectric Films: Crossing the Resolution Barrier." *Physical review letters.* vol. 103. no. 057601. (2009).

54. Morandi, C. S., “Bismuth Magnesium Titanate - Lead Titanate Thin Films for High Temperature Ferroelectric Memory.” *Pennsylvania State University ProQuest Dissertations Publishing* 2018. 28778766. (2018).

55. Zhu, W., Fujii, I. Ren, W., and Trolier-McKinstry S. “Domain Wall Motion in A and B Site Donor Doped $Pb(Zr_{0.52}Ti_{0.48})O_3$ Films,” *J. Am. Ceram. Soc.* 95 (9) 2906-2913 (2012).

56. Borman, T. M., and Trolier-McKinstry S. “{001} Textured Growth of Doped, Gradient Free, Lead Zirconate Titanate Thin Films by Chemical Solution Deposition.” *Pennsylvania State University ProQuest Dissertations Publishing*, 15 Sept. (2016).

57. Mittra, J., Abraham, G., Kesaria, M., Bahl, S., Singh, R., Shivaprasad, S., Viswanadham, C., Kulkarni, U., and Dey, G. “Role of Substrate Temperature in the Pulsed Laser Deposition of Zirconium Oxide Thin Film.” *Materials Science Forum.* Vol 710. Pp 757-761. (2012).

58. Schuettler,M., Stieglitz,T., “Microassembly and Micropackaging of Implantable Systems”, *Woodhead Publishing Series in Biomaterials*, 2013, pp. 108-149, (2013).